UNIVERSITÀ
DEGLI STUDI
DI PADOVA

Head Office: Università degli Studi di Padova

Department of Geosciences

Ph.D. COURSE IN: Geosciences

SERIES XXXV

HIGH DIFFERENTIAL STRESS IN THE SEISMOGENIC LITHOSPHERE: CONSTRAINTS FROM NUMERICAL MODELING AND MICROSTRUCTURAL ANALYSIS

Coordinator: Prof. Agnini Claudia

Supervisor: Prof. Giorgio Pennacchioni

Co-Supervisor: Prof. Luca Menegon

Co-Supervisor: Prof. Alfredo Camacho

Ph.D. student: Giovanni Toffol

«Io non posso accettare e tacere …
Quel che cerco l'ho nel cuore, come te»
C. Pavese, Dialoghi con Leucò

Abstract

The main goal of this thesis is to investigate the mechanics of seismic failure under high confinement pressure from the micrometric to the lithospheric scale, combining cutting-edge microstructural investigations and geodynamic numerical simulations. Deep-seated pseudotachylytes (i.e. coseismic quenched frictional melts), a proxy for deep earthquakes, are here both directly investigated to explore earthquake mechanics and used to constrain a brittle failure model on a lithospheric scale. Two complementary case studies are presented: (i) the seismicity at mid-crustal conditions, investigated from microstructural observations of pseudotachylytes from the hanging wall of the Woodroffe Thrust (Musgrave Ranges, central Australia), and (ii) the intermediate-depth subduction seismicity, whose predisposing conditions are modelled on a lithospheric scale extrapolating the occurrence of subduction-related deep pseudotachylytes to a general model of stress amplification promoting seismic failure.

In the thesis: (i) I provide new pressure estimates for the pseudotachylytes of the Woodroffe Thrust, from the analysis of Al_2SiO_5 stable polymorphs crystallizing from the melt in pseudotachylyte-bearing peraluminous gneisses. (ii) I present the first complete earthquake on-fault energy budget from an exhumed fault at mid-crustal conditions, by quantifying the work associated with crystal-plastic straining of the host-rock minerals by applying HR-EBSD (high-angular resolution electron backscattered diffraction) on seismically shocked garnets. (iii) I propose a process of stress amplification that may induce the high differential stresses required for intermediate-depth seismicity in the dry and strong peridotites of the subducting oceanic slab in absence of weakening mechanisms.

Riassunto

L'obiettivo di questa tesi è lo studio della meccanica del terremoto in condizioni di alta pressione ambientale dalla scala micrometrica alla scala litosferica, combinando studi microstrutturali all'avanguardia e simulazioni numeriche di processi geodinamici. Pseudotachiliti (fusi frizionali cosismici solidificati) profonde, un proxy per i terremoti profondi, sono qui investigate per studiare la meccanica dei terremoti e usate per vincolare un modello di rottura su scala litosferica. Due casi studio complementari sono presentati: (i) la sismicità in crosta intermedia, studiata con osservazioni microstrutturali di pseudotachiliti dall'hanging wall del Woodroffe Thrust (Musgrave Ranges, Australia centrale), e (ii) la sismicità di subduzione intermedio-profonda, le cui condizioni sono simulate su scala litosferica estrapolando la presenza di pseudotachiliti profonde di subduzione a un modello generale di rottura sismica promossa dall'amplificazione degli stress.

Nella tesi: (i) fornisco nuove stime di pressione per le pseudotachiliti del Woodroffe Thrust studiando la stabilità dei polimorfi di Al_2SiO_5 che cristallizzano dal fuso. (ii) presento il primo budget completo dell'energia dissipata sul piano di faglia durante un terremoto a condizioni di crosta intermedia, quantificando anche il lavoro associato alla deformazione cristal-plastica dei minerali della roccia incassante, applicando la tecnica HR-EBSD (diffrazione di elettroni retrodiffusi ad alta risoluzione angolare) su granati scioccati sismicamente. (iii) propongo un processo di amplificazione dello stress che può indure gli alti stress differenziali necessari per la sismicità intermedio-profonda in peridotiti anidre della placca oceanica in subduzione in assenza di altri processi.

Table of contents

INTRODUCTION

1. GENERAL INTRODUCTION

Earthquakes are among the most energetic events occurring on Earth. They shake the Earth since the inception of plate tectonics, affecting the lithosphere at depth (e.g. providing pathways for fluid percolation and promoting physical-chemical transformations (Jamtveit et al., 2018)) and at the surface (e.g. shaping the landscape (Bailey et al., 2011; Kirby and Whipple, 2012)). From a human perspective, high-magnitude earthquakes are catastrophic events responsible of thousands of deaths and huge economic losses (England and Jackson, 2011; Dal Zilio and Ampuero, 2023). Despite their relevance in the evolution of planet Earth as well as in everyday people's life, our comprehension of the laws governing the seismic cycle and the processes occurring on- and off-fault prior, during and after an earthquake is still patchy. For these reasons great effort is put into the study of earthquakes by various scientific communities (i.e. seismologists, experimentalists, numerical modelers, structural geologists), combining different approaches toward the common goal of a complete understanding of the earthquake mechanics.

Earthquakes typically nucleate in proximity of plate boundaries, in continental collision settings and along subduction zones. In the continental crust, most of the earthquake hypocentres are relegated to relatively shallow depths, approximately in the first 10–15 km (Scholz, 2019). This range of depths is consistent with common rheological models that propose a transition from brittle failure to ductile deformation at around 300 °C, the temperature of onset of crystal plasticity of quartz (Jackson, 2002; Burov and Watts, 2006). However, there are areas (e.g. the Indian plate underthrusting Tibet (Jackson et al, 2004; Bodin and Horton, 2004), the northern foreland of the Alps (Deychmann and Rybach, 1989; Singer et al., 2014), rifting areas (Albaric et al., 2009)), where earthquakes are recorded also at greater depths, in the middle and lower crust implying that the seismogenic layer (i.e. the portion of crust prone to seismic failure) can extend across the whole crust down to the Moho (Maggi et al.,

2000; Jackson et al., 2021). This distribution of hypocentres is at odds with conventional rheological models that propose the middle and lower crust to deform viscously rather than fracture (Ranalli, 1995).

In subduction zones, the depth distribution of earthquakes is wider and covers almost completely the whole subducting slab from the surface down to the mantle transition zone at 660 km (Wadati, 1928; Zhan, 2020; Frohlich, 2006; Houston, 2015). In this tectonic setting most of the hypocentres are located in the first 30–40 km along megathrusts and subsidiary faults marking the subduction interface. Increasing depth, seismicity tends to decrease exponentially towards a minimum at approximately 300 km of depth, and then slightly increase again towards the mantle transition zone. Earthquakes occurring between 70 and 300 km of depth are commonly referred to as intermediate-depth earthquakes. Their hypocentres typically define two planes that progressively merge at depth and are characterized by down-dip compression and down-dip extension in the upper and lower plane respectively (Enghdal and Scholz, 1977; Brudzinski et al., 2007; Florez and Prieto, 2019).

The occurrence of earthquakes at high confinement pressure represent an ongoing debate since at great depths brittle failure should be inhibited by viscous flow and, if this is not the case, it would still require extremely high differential stress. Several mechanisms have been proposed to explain seismic failure under these conditions:

- downward propagation of seismic ruptures (Tse and Rice, 1986; Moecher and Steltenpohl, 2009), that implies a transient strengthening of weak rocks due to high strain rates during seismic rupture propagation without the need of long-term high differential stresses accumulated in the lithosphere.
- stress transfer from the seismogenic crust (Ellis and Stöckhert, 2004) that propose a transient deepening of the brittle-ductile transition in response to high-magnitude events in the seismogenic upper crust.

- thermal runaway (Kelemen and Hirth, 2007; John et al., 2009; Thielmann et al., 2015), that propose a positive feedback between shear heating and weakening due to viscosity reduction that can ultimately lead to slip at seismic velocities. This mechanism was proposed both for intermediate depth earthquakes in the lower plane of seismicity (Prieto et al., 2013; Prieto et al., 2017) and for lower-crustal earthquakes (Stewart and Miranda, 2017; Papa et al., 2020)
- dehydration embrittlement (Raleigh and Paterson, 1965; Yamasaki and Seno, 2003; Brudzinski et al., 2007), that was proposed as a viable mechanism for intermediate-depth subduction earthquakes and imply an embrittlement of the lithosphere driven by an increase of fluid pressure during dehydration of serpentinites minerals.
- stress transfer due to dehydration reactions (Ferrand et al., 2017; Kita and Ferrand, 2019) that was proposed to be responsible of brittle failure at intermediate-depth conditions during subduction. Other phase transformations have also been proposed to be responsible for embrittlement and seismic failure (Shi et al., 2018; Incel et al., 2019).

Contraposed to these mechanisms is the brittle failure of strong and dry rocks under high (gigapascal-level) differential stress accumulated in-situ. Local build-up of high differential stress has been proposed to explain both lower-crustal and intermediate-depth subduction earthquakes, based on field and microstructural investigations of exhumed fault rocks (Campbell et al., 2020; Hawemann et al., 2019; Scambelluri et al., 2017; Pennacchioni et al., 2020).

Unfortunately, it is physically impossible to access and investigate an active seismic fault at hypocentre depth and the only direct information during an earthquake can be obtained from the interpretation of seismic waves. A window into the mechanics of earthquakes at depth is offered by exhumed fault rocks bearing pseudotachylytes (i.e. coseismic quenched frictional melts) recording ancient earthquakes. Their study is thus fundamental to enhance the comprehension of fault processes and earthquake mechanics as well as to infer aspects of the lithosphere rheology to build up new rheological models on.

In this thesis we take the most we can obtain out of exhumed deep-seated fault rocks to study earthquake mechanics from the microscale to the lithospheric scale. The goals are to investigate the mechanics of deep-seated seismic failure from the study of mid-crustal pseudotachylytes and to propose a new mechanism for earthquake rupture under high-pressure conditions in the subducting oceanic slab.

2. PSEUDOTACHYLYTES AS FIELD EVIDENCE OF ANCIENT EARTHQUAKES

The only clear and undebatable evidence of ancient seismic faulting in the geological record is represented by the occurrence of quenched frictional melt produced during seismic slip. This particular type of fault rock is called pseudotachylyte. It was first described from a meteorite impact crater (Shand, 1916) and only later identified also along exhumed faults (Philpotts, 1964; McKenzie and Brune 1972; Sibson 1975) and on the slipping plane of large landslides (Heuberger et al., 1984). Since their first descriptions, tectonic pseudotachylytes (i.e. pseudotachylytes produced due to frictional heating and melting along a seismically slipping fault) have proven to be a fundamental source of information for the study of earthquake mechanics from exhumed faults (e.g. Sibson, 1977; Di Toro et al., 2005; Pittarello et al., 2008; Petley-Ragan et al., 2019; Zhong et al., 2021; Mancktelow et al., 2022) and have become one of the main objects of study for structural geologists.

A pseudotachylyte is the solidified product of frictional wear and melting along the fault plane right after the propagation of the seismic rupture (Di Toro and Pennacchioni, 2004; Magloughlin, 2005; Spray, 2010;) and it is responsible for the lubrication of the fault plane favouring seismic slip (Di Toro et al., 2006). In the field pseudotachylyte occurs as a black aphanitic rock decorating the fault plane, with angular host-rock clasts in variable proportion. Pseudotachylyte fault veins can range in thickness from less than a millimetre to a couple of centimetres (Ferrand et al., 2021) and can extend undisturbed for tens of metres. Distinctive features are: (i) the presence of sharp selvages with truncated host-rock grains and often decorated by chilled margins; (ii) the occurrence of injection veins (Fig. 1) departing from the principal fault vein and intruding the host rock, extending for

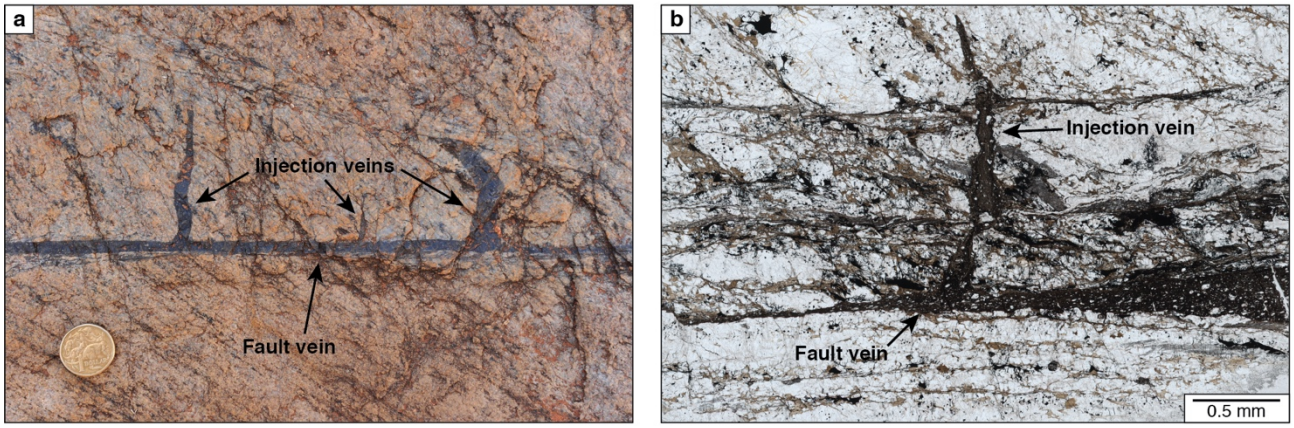

Fig. 1 |a, Pseudotachylyte fault vein with injection vein departing from it. **b**, thin section of pseudotachylyte. Both pseudotachylytes are from the hanging wall of the Woodroffe Thrust (25°59'32" S, 132°8'35" E)

millimetres to metres; (iii) the presence of portions of cataclastic breccia completely sealed by the pseudotachylyte melt. In presence of circulating fluids pseudotachylytes are easily altered (Fondriest et al., 2020) while in high-grade rocks they may be partially to completely overprinted by mylonitisation that can hide their friction-melt origins (Kirkpatrick and Rowe, 2013). For these reasons pseudotachylytes may be overlooked in the field thus losing part of the recorded information about earthquake mechanics.

Apart from witnessing the occurrence of an earthquake, pseudotachylytes and host rock can preserve frozen in time the history of a seismic event, from its initial stage of nucleation to the coseismic slip, arrest and subsequent postseismic creep. The study of pseudotachylyte and host-rock microstructures thus is useful to constrain on-fault processes (e.g. loading of high differential stress (Trepmann and stockert, 2001; Campbell and Menegon, 2022; Bruckner et al., 2021), rupture propagation and slip (Petley-Ragan et al., 2018; Mancktelow et al., 2022), energy consumption (Di Toro et al., 2005; Pittarello et al., 2008)) and, more in general, the rheological behaviour of the host rock and its evolution after seismic faulting (Menegon et al., 2017; Jamtveit et al., 2018; Pennacchioni et al., 2020;).

The study of exhumed pseudotachylytes produced during deep earthquakes (i.e. middle- to lower-crustal earthquakes and intermediate-depth subduction earthquakes) is of particular interest. Deep-seated pseudotachylytes are found in exhumed high-grade rocks exposing the roots of ancient mountain chains and in ophiolites (slices of the oceanic lithosphere subducted). Deep-seated pseudotachylytes have been described from various localities around the world (e.g. the Lofoten, Norway (Moecher and Steltenpohl, 2009; Menegon et al., 2017), the Bergen Arcs, Norway (Austrheim et al., 1994), northern Canada (Orlandini et al., 2018), central Australia (Hawemann et al., 2018; Hawemann et al., 2019) and in alpine ophiolites (Andersen and Austrheim, 2006; Fabbri et al., 2018; Scambelluri et al., 2017; Pennacchioni et al., 2020)). Deep seated pseudotachylytes are often found mutually overprinted by mylonites (Menegon et al., 2021), but pristine pseudotachylytes can be preserved if rocks were sufficiently dry to inhibit any subsequent overprint (Hawemann et al., 2018; Pennacchioni et al., 2020).

Typically, pseudotachylytes hosted in high-grade rocks are assumed to be the result of deep earthquakes. However, caution is required since seismic faulting can have occurred also during the exhumation path at shallower levels than those of the peak metamorphic conditions. Thus, it is mandatory to properly determine ambient conditions at the time of faulting before extrapolating microstructural observation to generalized failure models at depth.

Unfortunately, this task may be not straightforward, particularly if the pseudotachylyte is pristine. The mineralogical assemblage of a pseudotachylyte is typically out of equilibrium due to the fast quenching, and ion-exchange reactions useful for geobarometry are generally absent. A mylonitic overprint of the pseudotachylyte can promote metamorphic reactions useful to constrain ambient conditions, assuming the two processes to be coeval, however the mylonitisation would also erase part of the earthquake record. The presence of specific key phases crystallized in the quenching pseudotachylyte can offer some constraints on the pressure. Cauliflower garnet is typically invoked as an evidence for quenching at high pressure conditions (Pittarello et al., 2015; Papa et al., 2018), as well as the occurrence of kyanite, the archetypal high-pressure mineral.

The highest abundance of tectonic pseudotachylytes in the world is found in the hanging wall of the Woodroffe Thrust (Musgrave Ranges, central Australia) (Camacho et al., 1995; Lin et al., 2005; Wex et al., 2017; Hawemann et al., 2018). This area offers the great opportunity to study an ancient crustal-scale seismogenic zone, with seismicity constrained at middle- to lower- crustal conditions, whose activity lasted for at least a few tens of millions of years (de Gromard et al., 2019). For this reason, the area has been selected in this thesis to investigate the mechanics of earthquake failure in the continental crust.

3. THE ENERGY BUDGET OF AN EARTHQUAKE

An earthquake is the result of the abrupt conversion of potential energy (the elastic energy due to tectonic loading) into several energy contributions dissipated as work on fault and as radiated seismic waves (Scholz, 2019). While tectonic loading took years to hundreds of years (the interseismic period) to build up the stress required for failure, the releasing stage is extremely fast and last only a few seconds. In this short time span, the energy is released in a series of high stress events (rupture propagation (Reches and Dewers, 2005), frictional wear and melting during seismic slip (Di Toro et al, 2004; Bestmann et al., 2012; Papa et al., 2018)) responsible of the microstructural features (fracturing (Austrheim et al., 2017; Petley-Ragan et al., 2019; Mancktelow et al., 2022; Incel et al., 2019;), crystal plasticity of minerals (Campbell and Menegon, 2022), melt production (Di Toro et al., 2004)) observable in the volume of rock surrounding the slip plane.

The strain energy built up during the interseismic period is converted into: (i) radiated seismic waves (E_r), accounting for no more than 15–20 % of the total released energy (Lockner and Okubo, 1983) and work spent on the fault zone (E_{FZ}) (Scholz, 2019; Okubo et al., 2019; Cocco et al., 2023).

It is common to discuss the contributes of the energetic budget in terms of energy density (energy per square meter of slipping fault, expressed in Joule/m^2). The work dissipated on fault can thus be written as:

$$W_{FZ} = W_{FH} + W_{SF} + W_{CP}$$

where: W_{FH} is the frictional heat; W_{SF} is the fracture surface energy, i.e. the energy consumed to fracture the rock and propagate the rupture; and W_{CP} is the energy consumed in crystal-plastic and elastic straining of minerals lattice.

Of these contributions, heat represents the largest part of energy absorbed by the fault walls and it is responsible for the production of the pseudotachylyte melt (Di Toro et al., 2004). Fracture energy in general can represent up to 10 % of the total energy consumed during an earthquake and it is assumed to comprise also crystal-plastic energy, that has never been quantified separately (Cocco et al., 2023). Fracture energy have been constrained both from experiments and from the inversion of seismic data (Cocco et al., 2023).

The study of fault rock microstructures, both from exhumed ancient fault zones and from drill cores in the shallower portions of active faults, may provide the excellent opportunity to obtain an estimate of the energy budget from local microstructural observations directly traceable to a seismic event (Chester et al., 2005; Ma et al., 2006; Pittarello et al., 2008; Johnson et al., 2021). In particular, single-jerk pseudotachylytes offer the unique opportunity to quantify the energy released at a single point during the propagation of a single and well constrained earthquake rupture and seismic slip (Pittarello et al., 2008).

4. AIM AND OUTLINE OF THE THESIS

In recent years a vast production of scientific works has been focused on the study of deep-seated pseudotachylytes and in the extrapolation of local observations to general models to explain deep seismicity both in the continental and in the subducting oceanic lithosphere. With this thesis, we aim to give a contribution to the ongoing discussion, trying to fill some gaps in the topics of the earthquake energy budget and in the mechanics of intermediate-depth subduction earthquakes. Different approaches have been followed: (i) high resolution microstructural investigation, in particular applying the cutting-edge technique of HR-EBSD (high-angular resolution electron backscattered diffraction, Wallis et al., 2019) and (ii) geodynamic numerical simulations with the finite differences method.

The thesis is subdivided into three main chapters, all first authored, that deals with three main research aspects:

Chapter 1 contains a detailed petrographic description of the microlites crystallizing from the quenching melt of pseudotachylytes in peraluminous gneisses collected along the hanging wall of the Woodroffe Thrust (Musgrave Ranges, central Australia). The occurrence of the relatively-low-pressure mineral andalusite and cordierite stable together with kyanite in the pseudotachylytes is considered as an upper boundary for the pressure conditions of earthquake faulting.

Chapter 2 propose a full quantification of the on-fault energy budget of an earthquake occurred at mid-crustal conditions obtained from a pseudotachylyte from the Woodroffe Thrust. Together with the fracture energy and the heat we quantified for the first time the energy dissipated in the crystal-plastic deformation of the lattice of host-rock minerals and show that the associate features can be preserved through the exhumation path.

Chapter 3 is inspired by the description of deep (70 km) ophiolitic pseudotachylytes interpreted as an analogue for intermediate-depth seismicity in a dry subducting oceanic plate (Pennacchioni et al., 2020). We show with a numerical approach that during subduction of a dry oceanic plate the presence of scattered domains of partially serpentinized peridotite can amplify the stress field up to seismogenic levels. We thus propose a purely brittle process to explain intermediate-depth subduction earthquakes. This chapter, in a slightly different version, is published in the journal Earth and Planetary Science Letters (Toffol et al., 2022).

Chapter 1: New pressure estimates for the Woodroffe Thrust (Musgrave Ranges, central Australia) from the stability of Al_2SiO_5 microlites in pseudotachylytes

Toffol, G.[1], Pennacchioni, G.[1], Camacho, A.[2], Mancktelow, N.[3], Gillio, M.[4]
[1] University of Padova, Department of Geosciences, Padova, Italy
[2] University of Manitoba, Department of Geological Sciences, Winnipeg, Canada
[3] ETH Zurich, Department of Earht Sciences, Zurich, Switzerland
[4] University of Pavia, Department of Earth and Environmental Sciences, Pavia, Italy

The manuscript of this chapter is under preparation for submission on a peer-reviewed journal.
Authorship contribution statement:
GT: Conceptualization, Data collection, Interpretation, Writing – original draft, Writing – review & editing. **GP**: Conceptualization, Data collection, Writing – review & editing, Supervision. **AC**: Conceptualization, Supervision. **NM**: Conceptualization. **MG**: Data collection.

Abstract

The Woodroffe Thrust (Musgrave Ranges, central Australia) is a crustal scale tectonic structure developed at lower to middle crustal conditions during the Petermann Orogeny (630–520 Ma). Close to the Woodroffe Thrust contact, and along the various tectonic lines present in the hanging wall, the dominant granulitic rocks contain the largest volume of tectonic pseudotachylytes (coseismic quenched frictional melts) in the world. The ambient conditions of pseudotachylyte production along the Woodroffe Thrust have been inferred to be not so dissimilar from the northern to the southern exposures, ca. 520–650 °C, and 0.8–1.1 GPa to 650 °C and 1.0–1,3 GPa, respectively.

Here we investigated pseudotachylytes within peraluminous gneisses from 3 different locations in the hanging wall of the Woodroffe Thrust, tens of kilometres apart and at different distances along the thrust direction. High-resolution microstructural analysis of the pseudotachylyte microlitic assemblages indicate the coexistence of andalusite and kyanite crystallized directly from the quenching frictional melt. This new observation constrains the ambient pressure of faulting at < 0.5 GPa, i.e. at much shallower depth than previously estimated, and significantly changes the scenario of the tectonic setting and evolution of the Woodroffe Thrust.

1. INTRODUCTION

A pseudotachylyte is a quenched frictional melt present in some exhumed faults within silicate rocks. As such, pseudotachylytes are considered by most geologists as an incontrovertible evidence for seismic slip and can therefore provide useful clues on earthquake mechanics and rock rheology (Sibson, 1975; Swanson et al., 1992; Di Toro et al., 2005; Pittarello et al., 2008; Pennacchioni et al., 2020; Mancktelow et al., 2022). Pseudotachylytes are commonly found in faults exhumed from the base of the brittle upper crust, although their presence may be erased by deformation and alteration after formation and exhumation (Fondriest et al., 2020). Less common is the presence of pseudotachylytes in middle and lower crustal rocks, at conditions of pressure and temperature where rocks are predicted to deform in a ductile way rather than fail seismically. However, deep-seated pseudotachylytes have been described in middle and lower crustal rocks (Passchier, 1982; Austrheim and Boundy, 1994; Pittarello et al., 2012; Menegon et al., 2017; Hawemann et al., 2018; Orlandini et al., 2018). These pseudotachylytes have been interpreted as the product of ancient deep earthquakes, analogue of those currently occurring well below the brittle-ductile transition (i.e. below 10-15 km of depth), in different tectonic environments, e.g.: in the Indian shield underthrusting Tibet (Bodin and Horton, 2004), in the foreland of the norther Alps (Deichmann and Rybach, 1989; Singer et al., 2014) and in rift systems (Albaric et al., 2009). Deep-seated pseudotachylytes are almost exclusively encountered in dry, strong rocks, typically granulites, eclogites and peridotites, that are capable to build up the high differential stress required to fail seismically under high confinement pressure. These pseudotachylytes are often locally mylonitised, and more than one generation of pseudotachylytes and mylonites, mutually overprinting each other, can be identified. This overprinting relationship suggests cyclic interplay between brittle (seismic) and ductile (aseismic) deformation mechanisms (Hawemann et al., 2019; Campbell et al., 2020, Menegon et al., 2021; Stewart and Miranda, 2017; Papa et al., 2020). Brittle seismic failure may also represent an efficient process to weaken the lower crust, by favouring fluid infiltration and promoting metamorphic re-

equilibration reactions in otherwise dry and metastable rocks (Menegon et al., 2017; Jamtveit et al., 2018; Jamtveit et al., 2019).

The occurrence of pseudotachylytes in high-grade rocks alternating with mylonites is commonly considered as a proxy for deep seismicity. However, this syllogistic view of pseudotachylytes hosted in high-grade rocks may lead to erroneous interpretations. Unfortunately, to obtain precise estimates of the ambient conditions of seismicity from exhumed pseudotachylyte-bearing faults is difficult, particularly when pseudotachylytes are pristine. A major obstacle for this estimate is represented by the essentially magmatic nature of the mineralogic assemblages crystalizing from the quenching melt that in most cases do not provide ion-exchange reactions useful for geobarometry. To make things more complicated, given the short time of quenching (seconds to minutes), crystallization is not an equilibrium process and overstepping is common. Crystallization within a quenching melt is also strongly controlled by the presence of host rock clasts that serve as seeds for crystal nucleation. Thus, the presence or absence of specific minerals in the host rock and eventual processes that can determine their disappearance may pre-determine the mineralogy of the quenched pseudotachylyte (Papa et al., 2018). Microlitic garnet, commonly called "cauliflower garnet", is the most invoked mineral to assign the wording high-pressure to a pseudotachylyte, together with kyanite, the archetypal high-pressure phase.

The largest volume of tectonic pseudotachylytes in the world is hosted in the hanging wall of the Woodroffe Thrust (WT), Musgrave Ranges (Camacho et al., 1995). The WT is an E-W, top-to-north crustal scale shear zone extending over 600 km along strike and outcropping for almost 100 km in the eastern Musgrave Ranges. A very shallow dip angle of ca. 6° has been calculated for the WT based on the small temperature and pressure variations (520–650 °C, 0.8–1.1 GPa in the north to 650 °C and 1.0–1,3 GPa in the south) along an ~ 60 km cross section in the direction of thrusting within the footwall mylonites (Wex et al., 2017). The eastern Musgrave Ranges represent one of the best localities worldwide to investigate a deep seismogenic zone now exhumed to the Earth's surface. This region has been already the focus of several geological studies (Camacho et al., 1995; Hawemann et al., 2018, 2019a, 2019b; Lin et al., 2005, 2008; Wex et al., 2017, 2018, 2019;

Mancktelow et al., 2022). In these studies, however, there is still a significant uncertainty in the estimates of the ambient conditions at the time of faulting. Pressures calculated for the synkinematic metamorphic assemblage in the mylonites marking the WT (predominantly the footwall rocks) were considered representative for the ambient conditions of pseudotachylyte-forming faulting based on the fact that they contain sheared pseudotachylytes and are in turn overprinted by undeformed pseudotachylytes. In this work we investigated pseudotachylytes hosted in peraluminous gneisses in the pseudotachylyte zone of the WT from three different localities in the northern outcrops. The type of Al_2SiO_5 polymorph crystallizing from the quenched melt constrains the pressure at the time of faulting. The new pressure values that we propose, lower than the previously suggested values, impact the reconstruction of the regional thrust geometry of the WT.

2. GEOLOGICAL SETTING

The Proterozoic Musgrave Province, central Australia, is situated at the junction between the North, West and South Australian Cratons, which amalgamated ~1300 Ma during the development of Rodinia (Myers et al., 1996). In the Musgrave Province several major shear zones (Major, 1970; Bell, 1978; Major and Conor, 1993; Camacho et al., 1997; Scrimgeour et al., 1999; Edgoose et al., 2004) developed during the intracontinental Petermann Orogeny (630–520 Ma) (Maboko et al., 1992; Camacho and Fanning, 1995; Camacho and McDougall, 2000; de Gromard et al., 2019): the Woodroffe Thrust (WT) as the major structure; the northern Davenport and Davenport shear zones; the Ferdinand shear zone; the Mann Fault (Fig. 1). The WT juxtaposed granulite facies gneisses and granites of the Fregon subdomain in the hanging wall with upper-amphibolite facies gneisses of the Mulga Park subdomain in the footwall (Major, 1970; Edgoose et al., 1993; Camacho and Fanning, 1995; Major and Conor, 1993; Wex et al., 2017). The two subdomains were metamorphosed during the Musgravian Orogeny (ca. 1200 Ma) and intruded by voluminous syn- to post-tectonic intrusions (Pitjantjatjare Supersuite, Giles Complex) and swarms of dikes (Alcurra Dolerite swarm, Amata Dolerite swarm) before the Peterman Orogeny (Gray, 1978; Maboko et al., 1991; Major and Conor, 1993; Camacho and Fanning, 1995; Camacho et al., 1997; Scrimgeour et al., 1999; Wade et al., 2008;

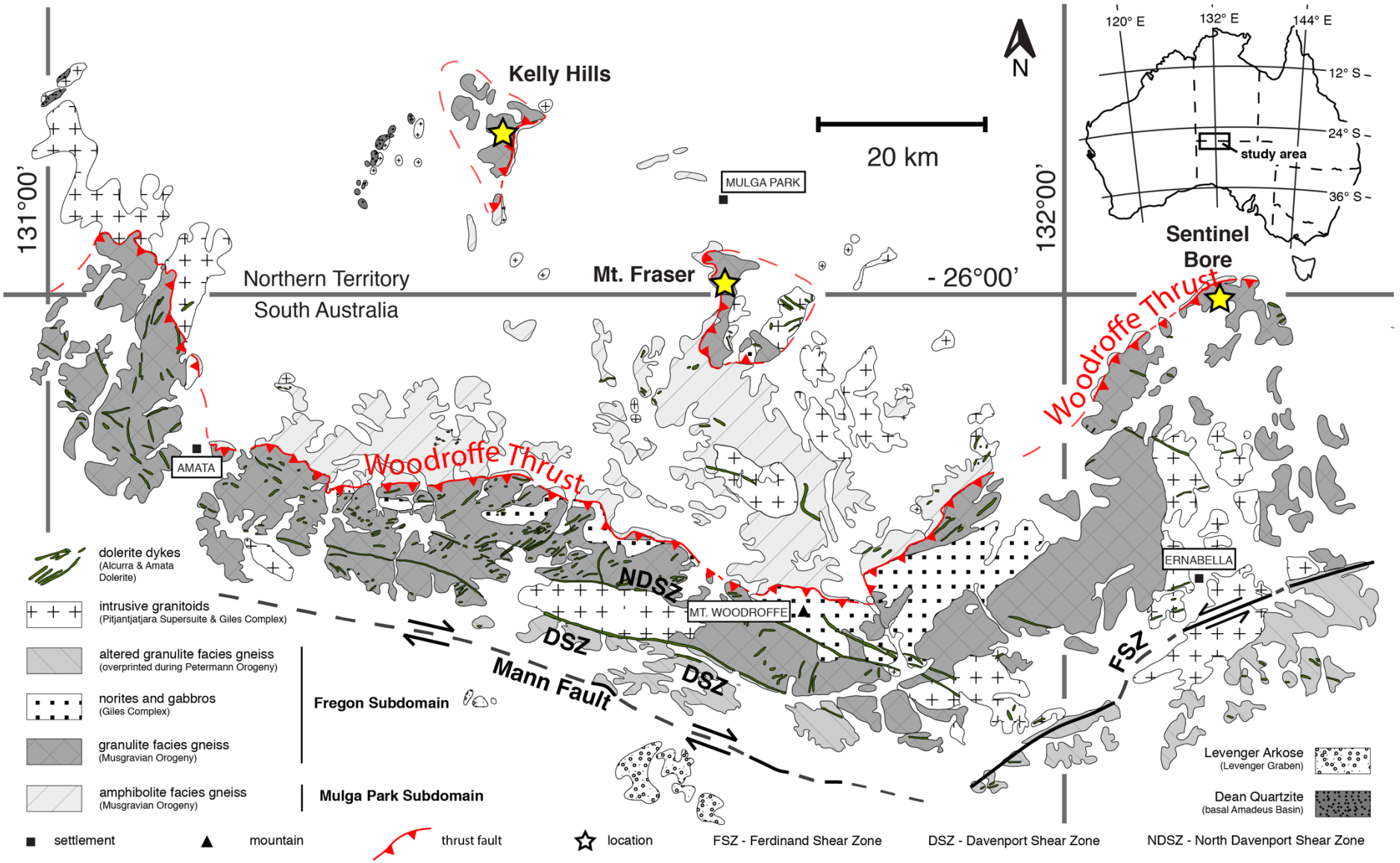

Fig. 1 | Geological map of the central Musgrave Block. Yellow stars mark the locations of the investigated samples. Redrawn after Wex et al., 2017

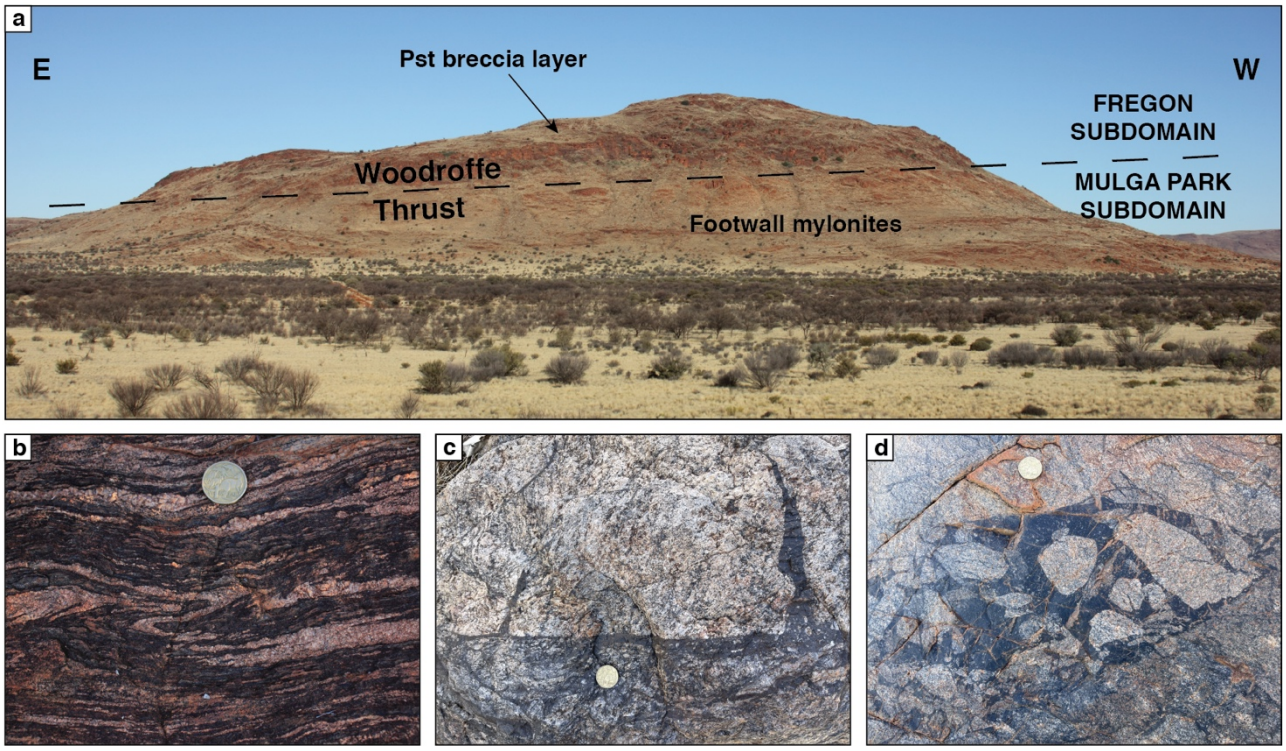

Fig. 2 | The Woodroffe Thrust. a, View of Mount Fraser, looking towards south. The dashed black line marks the WT at the contact between the footwall mylonites and the hanging wall pseudotachylytes constituting the decametric cliff indicated by the black arrow. **b,** granulitic layering in a peraluminous gneiss. **c,** pseudotachylyte fault vein with a decametric injection vein deprating from it. **d,** pseudotachylyte breccia

Smithies et al., 2011). The Fregon and Mulga Park subdomains likely represent different crustal levels (deeper and shallower, respectively) of the same terrane as suggested by the similarity in lithological composition (mainly quartzo-feldspatic gneisses and granitoids with metapelites, metadolerites and mafic gneisses) and in the structural and magmatic history (Camacho and Fanning, 1995, Scrimgeour et al., 1999). During the Petermann Orogeny, the granulites of the Fregon subdomain experienced peak metamorphic conditions of amphibolite to sub-eclogite facies, estimated in the range of 700–750 °C and 1.2–1.4 GPa to 650–700 °C and 1.2 GPa from west to east (Clarke et al., 1995; White and Clarke, 1997; Scrimgeour and Close, 1999; Ellis and Maboko, 1992; Camacho et al., 1997). These metamorphic conditions were originally interpreted to represent isobaric cooling during the Musgravian Orogeny (Ellis and Maboko, 1992), proposing the exhumation along the WT as the last part of a long-lasting anticlockwise P-T-t path. However, Camacho and McDougall (2000) and Camacho et al. (2009) reinterpreted the sub-eclogitic overprint as the product of a rapid cycle of burial and exhumation during the Petermann Orogeny.

The WT, well exposed in the eastern part of the Musgrave Ranges (e.g. Fig. 2a), consists of a thick (100–600 m; Wex et al., 2018) shallowly south-dipping band of mylonites and a pseudotachylyte zone up to 1 km thick (Camacho et al., 1995). Mylonitisation affected mainly the footwall rocks as testified by the thorium signature of the mylonites, compatible with that of the Mulga Park Subdomain (Wex et al., 2018). The much more extensive mylonitization of the Mulga Park Domain with respect to the Fregon Domain along the WT was interpreted as the result of more hydrated conditions in the footwall rock which favoured weakening compared to the dry stiff rocks of the hanging wall (Bell, 1978; Camacho et al., 1995; Wex et al., 2018; Wex et al., 2019). The pseudotachylyte zones comprises large volumes of pseudotachylytes (up to 4%), with only a minor portion mylonitised and hardly distinguishable from the footwall mylonites (Camacho et al., 1995; Wex et al.,2017; Wex et al., 2018).

3. METHODS

Polished thin sections of pseudotachylyte-bearing gneisses were studied by optical and electron microscopy. Electron microscopy investigations (imaging, EDS chemical analysis, electron backscattered diffraction (EBSD)) were performed on a FEG-SEM TESCAN Solaris at the Department of Geosciences of the University of Padova. High-resolution imaging was performed in backscattered electron mode with a mid-angle BSE detector. Working conditions were: 5keV of acceleration voltage; 300 pA of beam current; 4 mm of working distance. Acquisition time ranged between 23 and 53 minutes per frame, producing high-quality images with resolution up to 3072x3072 pixels. EDS quantitative analyses were performed with a Ultim Max 65 (Oxford Instruments) detector calibrated over Co. Working conditions were: 15 keV of acceleration voltage; 3 nA of beam current; 5 mm of working distance. EBSD maps were acquired with a CMOS-Symmetry (Oxford Instruments) detector and indexed with the software Aztec. Working conditions were: 15 keV of acceleration voltage; 3 nA of current; working distance of 14–18 mm; sample tilt of 70°. Subsequent processing of the maps was performed with the toolbox MTEX 5.6.1 (Hielscher and Schaeben, 2008) in MATLAB®. Isolated indexed pixels were discarded and single not indexed pixels

inside grains were filled with neighbour values. Grains were reconstructed considering a threshold angle of 10° for all the phases and a minimum of 2 indexed pixels per grain. Raman spectroscopy analyses were conducted with a Horiba LabRAM HR Evolution Raman microscope (University of Pavia). A green (532 nm) laser with a spot size of approximately 1 m was used. Spectra were obtained averaging two consecutive acquisitions of 5–15 seconds. X-ray powder diffraction (XRPD) analysis was conducted on pulverized samples with a Panalytical X'Pert (University of Padova). X-ray fluorescence spectrometry (XRF) investigations were performed with a WDS Panalysitcal Zetium (University of Padova) on the same powders prepared for XRPD.

4. SAMPLES

We investigated pseudotachylytes within peraluminous gneisses in the pseudotachylyte zone of the WT. The samples come from three different locations along the WT in the eastern Musgrave Range: (i) Sentinel Bore (SB) to the east side, (ii) Mt. Fraser (FR) in the middle and (iii) Kelly Hills (KH) to the west, spaced ca. 40 km E–W one each other, with KH ca. 10 km further N with respect to SB and FR in the direction of thrusting (Fig. 1).

In all the three locations the peraluminous gneisses are interlayered with rocks of intermediate and felsic compositions. The peraluminous gneisses are medium grained and consist of mm-thick layers of quartz-feldspars (light colour) alternating with cordierite-sillimanite-rich (dark colour) layers (Fig. 2b). Locally, migmatitic folds and ponds with restitic material are present. Other minerals include sparse garnet, magnetite, ilmenite and biotite in variable abundance. The Al_2SiO_5 polymorphs present in the gneisses and pseudotachylytes include: (i) sillimanite, predominant in all 3 localities; (ii) kyanite, also present in all the 3 localities; and (iii) andalusite (reported for the first time) in SB. The mineralogical compositions determined by XRPD and the XRF bulk-rock chemical compositions are presented in Supp. Fig. 1 and in Supp. Tab. 1. Pseudotachylytes (e.g. Fig. 2c-d) are widespread in the investigated localities (Fig. 2a). They occur either as breccia layers of variable thickness (decimetric to metric) or as networks of spatially dense fault and injection veins with mutual crosscutting

relationships. The simplest systems with isolated pseudotachylyte fault veins and locally associated injection veins were selected for the microstructural investigations.

5. MICROSTRUCTURAL OBSERVATIONS

5.1 Sentinel Bore

Two samples from the Woodroffe Thrust at Sentinel Bore were investigated (i) a highly strained granulite with a mm-thick pseudotachylyte fault vein and an associated 2-cm-long injection vein and (ii) a nearby sheared pseudotachylyte

The pristine pseudotachylyte fault vein marks a discordance in the orientation of the granulitic foliation which is parallel to the vein on the side containing the injection vein and forming an angle of ca. 30 ° on the other side. The host rock is characterized by alternating mm-thick quartz-feldspar-rich and cordierite-sillimanite-rich layers. In the vicinity of the pseudotachylyte the rock is affected by a pervasive network of micro fractures oriented at a high angle to the fault vein and by micro-shear zones subparallel to the fault vein.

Host rock microstructure

In the host rock, mm-sized cordierite grains are partly overprinted by an andalusite-quartz-biotite symplectite nucleating along fractures. The simplectic intergrowth of andalusite-quartz at the core passes into a symplectic aggregate of biotite and quartz at the rim, preserving the continuity of vermicular quartz (fig. 3a, b). Sub-micrometric magnetite crystals are scattered within the symplectites and generally aligned along the fractures. Sheaves of acicular kyanite up to 20 μm in length grow along the fractures overprinting the andalusite-quartz-biotite symplectites, with the larger crystals overgrowing the new biotite. Locally, cordierite is almost completely replaced by the andalusite-quartz-biotite aggregates and shows an extensive overgrowth of acicular kyanite. The surviving non-replaced relicts of cordierite are commonly altered to pinite. Nearby replaced cordierite along the fractures, K-feldspar exhibits flame perthites oriented subparallel to the fractures (Fig. 3c). Granulite facies sillimanite is not recrystallized or replaced, even in the intensely fractured cataclastic

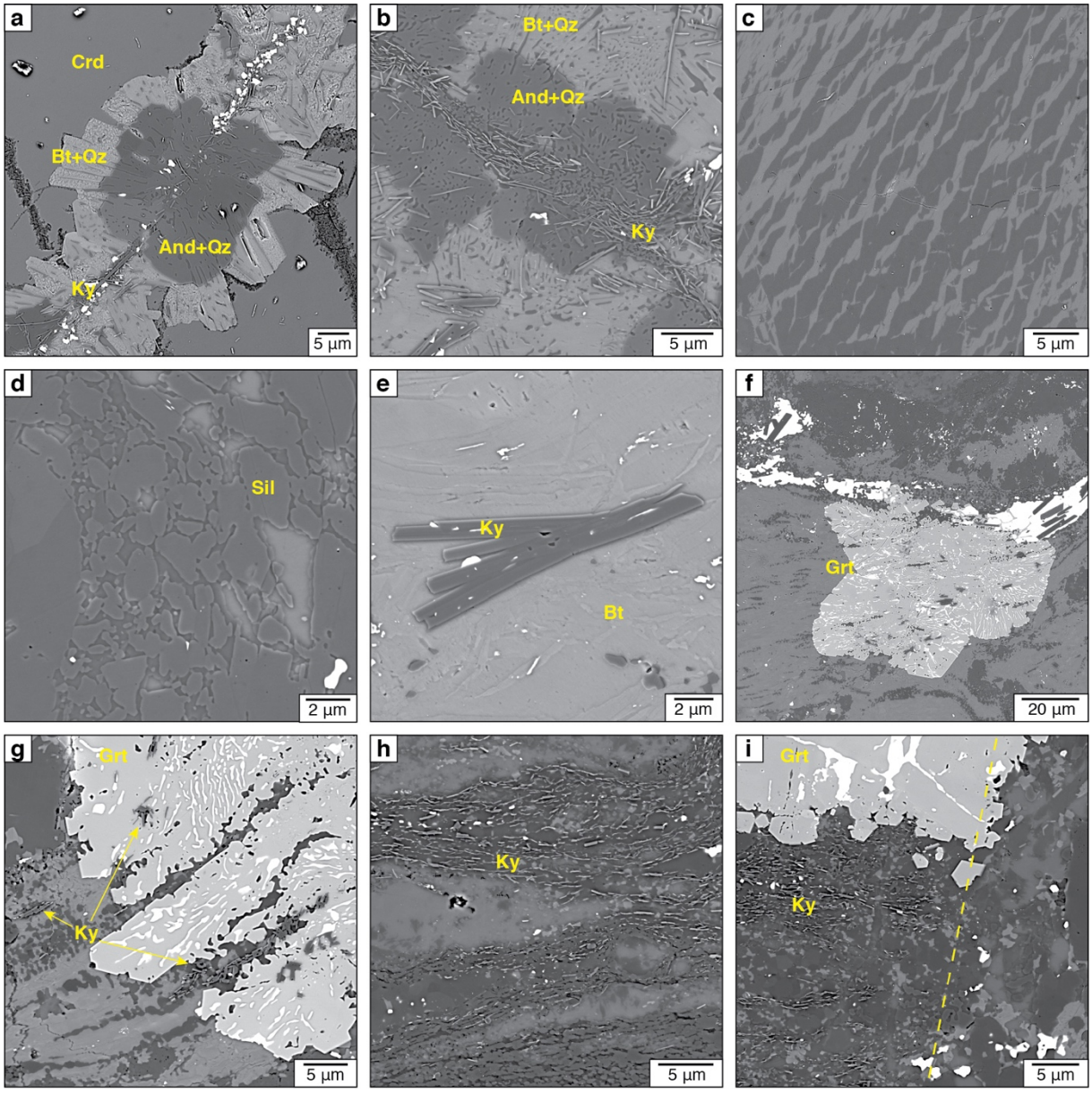

Fig. 3 | Sentinel Bore, host rock microstructures. BSE images of: **a,** cordierite decomposed along a fracture into an aggregate of andalusite and quartz rimmed by biotite and quartz, with magnetite mainly along the fracture. Quartz is continuous across the andalusite-biotite rim. Kyanite needles of variable size crystallize along the fracture. **b,** detail of a cordierite completely susbstituted into an andalusite-biotite-quartz aggregate with abundant kyanite. **c,** micrometric flame perthite developed around the substituted cordierite grains. **d,** crushed sillimanite close to a pseudotachylyte vein. Sillimanite is metastable. **e,** kyanite crystal growing over biotite. **f,** garnet crystal growing over biotite. The structure of the biotite, with abundant trails of micrometric euhedral quartz grains, is locally preserved in the garnet. Garnet is affected by abundant exsolutions of Fe-Ti oxides. **g,** detail of a garnet overgrowing biotite with kyanite crystals both on the biotite and included in the garnet. **h,** detail of a microshearzone with submicrometric kyanite needles aligned along the microshearzones and locally enveloping rigid domains. **i,** a sharp fracture cutting and displacing a microshearzone (marked by the aligned submicrometric kyanite crystals) and a garnet crystal. Garnet is locally overgrown by a micrometric layer developing euhedral shapes along the fractured side and in contact with the microshearzone.

domains and along the micro-shear zones. In contact with the pseudotachylyte vein (Fig. 3d) sillimanite fragments are rimmed by a halo resembling a "corroded fabric", with space filled by quartz. Kyanite crystals, up to 50 μm in length, overgrow statically the host-rock biotite (Fig. 3e). Kyanite is commonly characterized by a cleavage associated with nanometric exsolution of magnetite. The biotite overgrown by kyanite commonly shows the nucleation of clusters of small (< micron) quartz grains aligned in the foliation. Garnet crystallizes in dendritic crystals, a few hundred micrometres in size, replacing biotite (Fig. 3f, g). The dendritic cauliflower habit is commonly associated with the occurrence of pervasive vermicular inclusions of ilmenite locally arranged in radial patterns. Garnet also includes kyanite and quartz aligned into the foliation of the host biotite.

Micro-shear zones, trending roughly parallel to the fault vein, are present in the first 2–3 cm on both sides of the fault vein. These structures either exploit the former foliation or link biotite-rich domains. The wider micro-shear zones locally show cataclastic features. Abundant nanometric kyanite needles are aligned in the foliation of the micro-shear zones, together with micrometric euhedral quartz grains and biotite (Fig. 3h). Other auxiliary planes with oriented micrometric crystals interested by shearing departs from the main micro-shear zones, typically at low angle and resembling sharp fractures under the optical microscope. Millimetric injection veins depart from one of these micro-shear zones close to the main pseudotachylyte injection vein. Fractures are abundant and extended across the whole specimen and typically appear as extremely sharp features also at the microscale. Fractures close to the pseudotachylyte are often associated with sets of microfractures extending for only a few millimetres and decorated by micrometric opaque minerals. Micro-shear zones are locally truncated and displaced by fractures that interrupt the foliation defined by kyanite (Fig. 3i). Garnet, when crosscut by fractures shows a recrystallization rim of a few microns.

Pseudotachylyte microstructure

The pseudotachylyte is well crystallized, with only scattered portions of unresolvable cryptocrystalline material representing the most residual melt portions. The mineral assemblage includes fine-grained (sub-micrometric to micrometric) quartz, andalusite, biotite, feldspars,

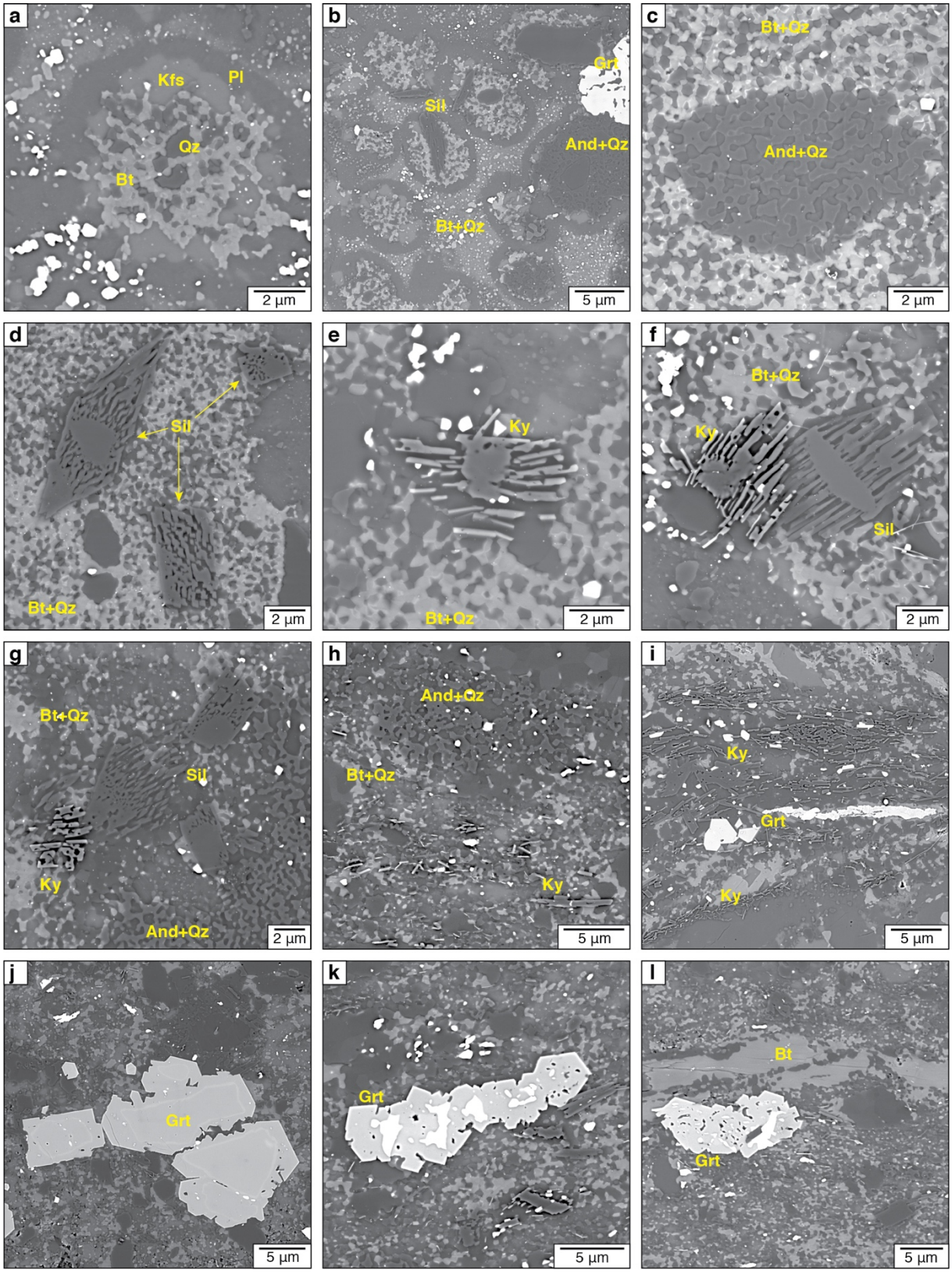
a
Kfs
Pl
Qz
Bt
2 µm
b
Grt
Sil
And+Qz
Bt+Qz
5 µm
c
Bt+Qz
And+Qz
2 µm
d
Sil
Bt+Qz
2 µm
e
Ky
Bt+Qz
2 µm
f
Bt+Qz
Ky
Sil
2 µm
g
Bt+Qz
Sil
Ky
And+Qz
2 µm
h
And+Qz
Bt+Qz
Ky
5 µm
i
Ky
Grt
Ky
5 µm
j
Grt
5 µm
k
Grt
5 µm
l
Bt
Grt
5 µm

Fig. 4 | Sentinel Bore, pseudotachylyte microstructures. BSE images of: **a-g** microstructures of the pseudotachylyte injection vein; **h-**l microstructures of the pseudotachylyte fault vein. **a,** globular aggregate of biotite and quartz rimmed by plagioclase and K-feldspar. **b,** group of globular aggregates of biotite-quartz and andalusite-quartz with andalusite substituted at the boundaries by biotite. The aggregates are rimmed by plagioclase and K-feldspar, an unresolvable matrix rich in oxides fill the remnant space. Small sillimanite microlites are present. **c,** amoeboid andalusite-quartz aggregate surrounded by biotite and quartz. The alteration rim is neat, and quartz is continuous through it. Where biotite substitutes andalusite quartz develops triple junctions. **d,** sillimanite microlites, with thin needles overgrowing sillimanite clasts. **e,** kyanite microlite with the typical small holes. **f,** kyanite microlite partially superimposed on a sillimanite microlite. Kyanite overgrows a former kyanite clast. **g,** microlites of kyanite, andalusite and andalusite. **h,** partially disaggregated andalusite-quartz aggregate, with andalusite showing incipient substitution by biotite. Kyanite crystals iso-oriented with fault vein direction. **i,** kyanite microlites oriented with the fault vein direction. A stripe of cataclastic garnet elongated accordingly is present. **j,** garnet clasts overgrown by new garnet. A nanometric layer with different composition or Fe-oxides bounds the clasts. **k,** garnet microlite boudinaged in the fault vein. Oxides fill the cavities between the garnets. **l,** clast of host-rock biotite preserved in the pseudotachylyte.

sillimanite, kyanite, Fe-Ti oxides and garnet microlites. The injection vein preserves the original quenched microstructure while the aggregates in the fault vein are slightly sheared and disrupted during syn- to post-cooling shearing. With the exception of cordierite, the pseudotachylyte contains clasts of all the host-rock minerals, including low-melting point minerals such as K-feldspar and biotite.

In the injection vein, intergrowths of andalusite and quartz with a symplectic texture are common (Fig. 4c, Fig. 5a). These intergrowths (referred hereafter as spherulites) are rounded in shape close to the pseudotachylyte vein boundary and becoming more irregular in shape toward the centre (Fig. 4a, b). EBSD analysis indicates that the andalusite spherulite is a single crystal and the quartz vermicules (or groups of neighbouring vermicules) commonly have a crystallographic orientation inherited from that of the quartz clast locally present at the core of the intergrowth (Fig. 5b). Clusters of neighbouring andalusite spherulites share, in many instances, the same CPO. Andalusite is locally, statically replaced at the rim by an aggregate of submicrometric polygonal biotite and quartz vermicules as well is recrystallized to a polygonal submicrometric (ca. 0.5 μm grain size) aggregate (Fig. 4c). The contact between andalusite and biotite is neat, and their continuity in shape is maintained. The altered andalusite spherulites are often rimmed by plagioclase associated with patches of K-feldspar (Fig. 4a). The spherulites are immersed in a cryptocrystalline K-rich matrix clustered with nanometric Fe-Ti oxides. Sillimanite is present as microlites overgrowing in crystallographic continuity sillimanite

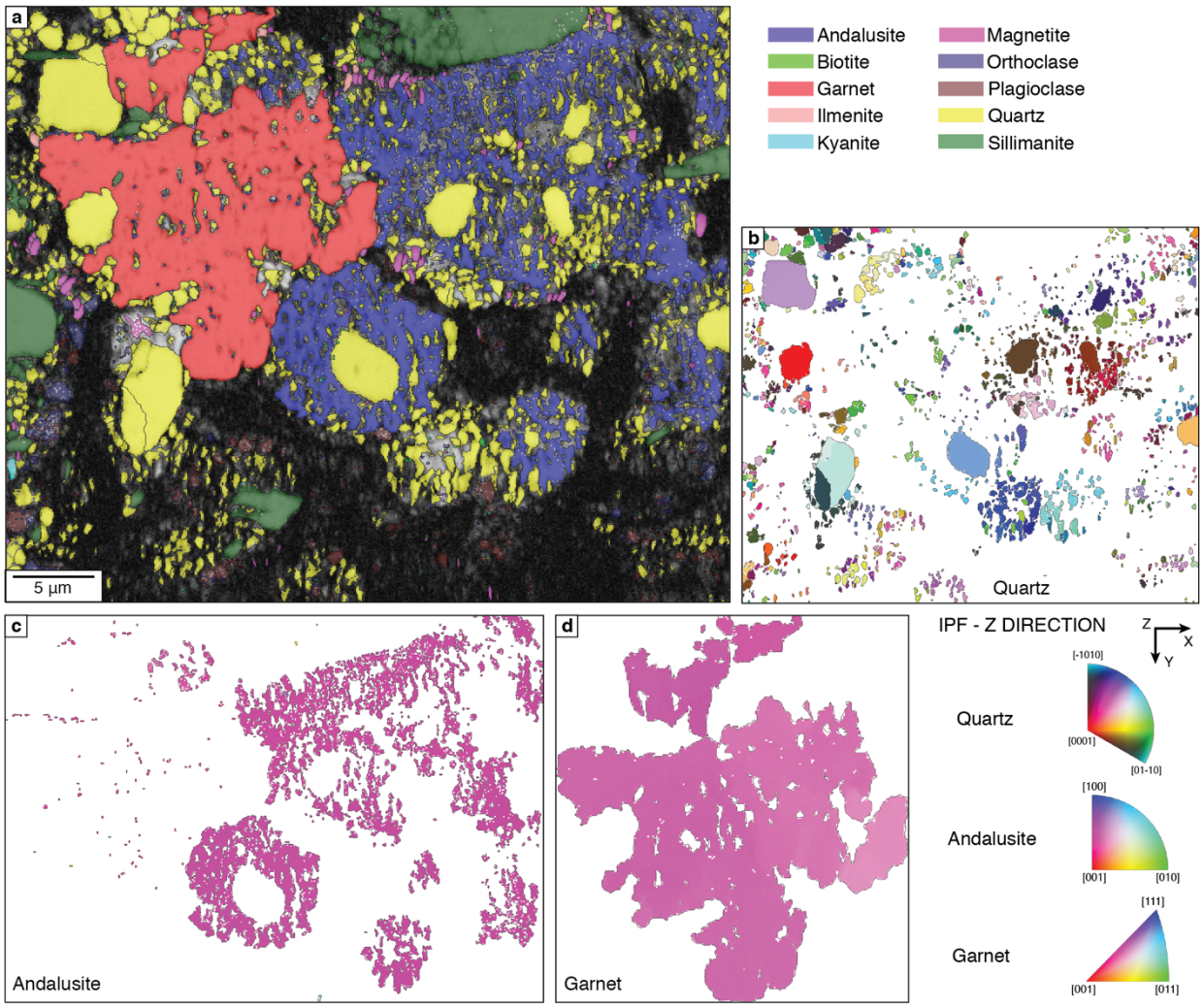

Fig. 5 | EBSD map in a pseudotachylyte fault vein from Sentinel Bore. a, phase map. **b,** quartz orientation map. The orientation of small quartz vermiculi crystallizing with andalusite is controlled by that of quartz clasts nearby. **c,** andalusite orientation map. all the andalusite in the map has the same crystallographic orientation, it is a single dendritic crystal. **d,** garnet orientation map. The garnet is a single crystal. Colour coding, based on inverse pole figures with respect to z-direction, for quartz, andalusite and garnet is reported in the bottom right corner.

clasts (Fig. 4d, f, g). The microlites are needle-shaped (few microns in thickness and as much as 10 µm in length), elongated along the c-axis, and are appended on the opposite sides of the parent sillimanite clasts. In cross-section at a high angle to the sillimanite c-axis, the sillimanite microlites show a characteristic maze-shaped geometry intergrown with quartz (Fig. 4d). Kyanite occurs as small needle-shaped microlites, with thickness ranging from hundreds of nanometres to a couple of microns, length up to ten microns and locally displaying hopper crystal shapes (Fig. 4e, g). In only rare cases, kyanite is found to overgrow a seed kyanite clast (Fig. 4e). The largest kyanites crystals, with lower aspect ratio than the smaller microlites, resemble the kyanite in the host rock. Overprinting

relationships indicate that kyanite microlites grew later that sillimanite microlites (Fig. 4f). Raman spectra used to confirm the different Al_2SiO_5 polymorphs present in the pseudotachylyte are reported in Supp. Fig. 2. Garnet is present as cauliflower-shape microlites, with a single crystallographic orientation and only slight distortions (Fig. 5a, d). Neighbour cauliflower garnets are found to share the same crystallographic orientation indicating a complex arborescent 3D structure, similar to andalusite (Supp. Fig. 3). Garnet includes commonly abundant magnetite, delineating the cauliflower structure, as well as quartz, andalusite and kyanite.

The injection vein shows a slight foliation perpendicular to the vein selvages locally defined by the orientation of elongated crystallized domains. Concordantly, biotite crystals grow in pressure shadows around crystallized domains and clasts.

The mineral phases observed in the injection veins are also found in the fault vein. The pristine microstructure of the pseudotachylyte is disrupted, but locally the association of quartz and andalusite with its biotite replacement is still preserved (Fig. 4h). Sillimanite microlites are less abundant than in the injection vein and occur only locally on sillimanite clasts. Kyanite, on the other hand, is more abundant. It forms sub-micrometric acicular crystals iso-oriented with shearing direction, similar to the kyanite observed in the micro-shear zones (Fig. 4i). Locally kyanite grows statically in bigger crystals, similar to those in the injection vein and in the host rock biotite, superimposed on quartz + biotite aggregates. Garnet is abundant, especially close to host rock garnets where fragments are dispersed in the pseudotachylyte (Fig. 4j–l). It typically overgrows clasts, clearly distinguishable by a nanometric bright rim determined by a sharp variation of composition or by the presence of nanometric oxides along the boundary of the clast. Garnets are commonly elongated and boudinaged concordantly with the direction of shearing, with the micro-boudinage cavities filled with oxides (Fig. 4k). Pressure shadows of biotite around rigid clasts, similar to those observed in the injection vein, are also present, oriented concordantly with shear direction.

Sheared pseudotachylyte

In the sheared pseudotachylyte the quench microstructures are completely obliterated by deformation. Abundant sub-micrometric acicular kyanites are disseminated in the pseudotachylyte. Near the replaced cordierite some micrometric lozenge crystals of probable andalusite crystallized in the sheared pseudotachylyte, suggesting that andalusite was still stable during shearing.

5.2 Mount Fraser

The investigated sample shows a main fault vein with a centimetric injection vein departing from it. Observations are focused on the injection vein, that preserve the original quenched assemblages, and the bounding host-rock.

Host rock microstructure

The host rock is particularly rich in sillimanite, present in abundant needles a few millimetres in length and clearly recognisable also macroscopically in the dark-colour restitic layers. Cordierite, garnet and opaque minerals are present associated with sillimanite (despite cordierite was never observed in the selected sample). Microstructures in the host rock are similar to what observed in the SB samples, with pervasive sets of microfractures filled with opaques. Micro-shear zones were not identified due to the more complex structure of the pseudotachylyte vein network.

Pseudotachylyte microstructure

The pseudotachylyte is rich in microlites and clasts, and the matrix is almost completely crystallized. Irregular aggregates of quartz and biotite with minor plagioclase constitute most of the matrix, together with anhedral crystalline cordierite. Scarce portions of cryptocrystalline material with abundant nanometric oxides droplets fill the rest of the vein. Microlites of sillimanite are abundant in the pseudotachylyte and occur either as long sheaves of needles departing from the opposite sides of clasts, as set of submicrometric partially interconnected lozenges or as bigger lozenges of tight maze-shaped microlites (Fig. 6a, b). Kyanite is present in small elongated microlites, typically showing

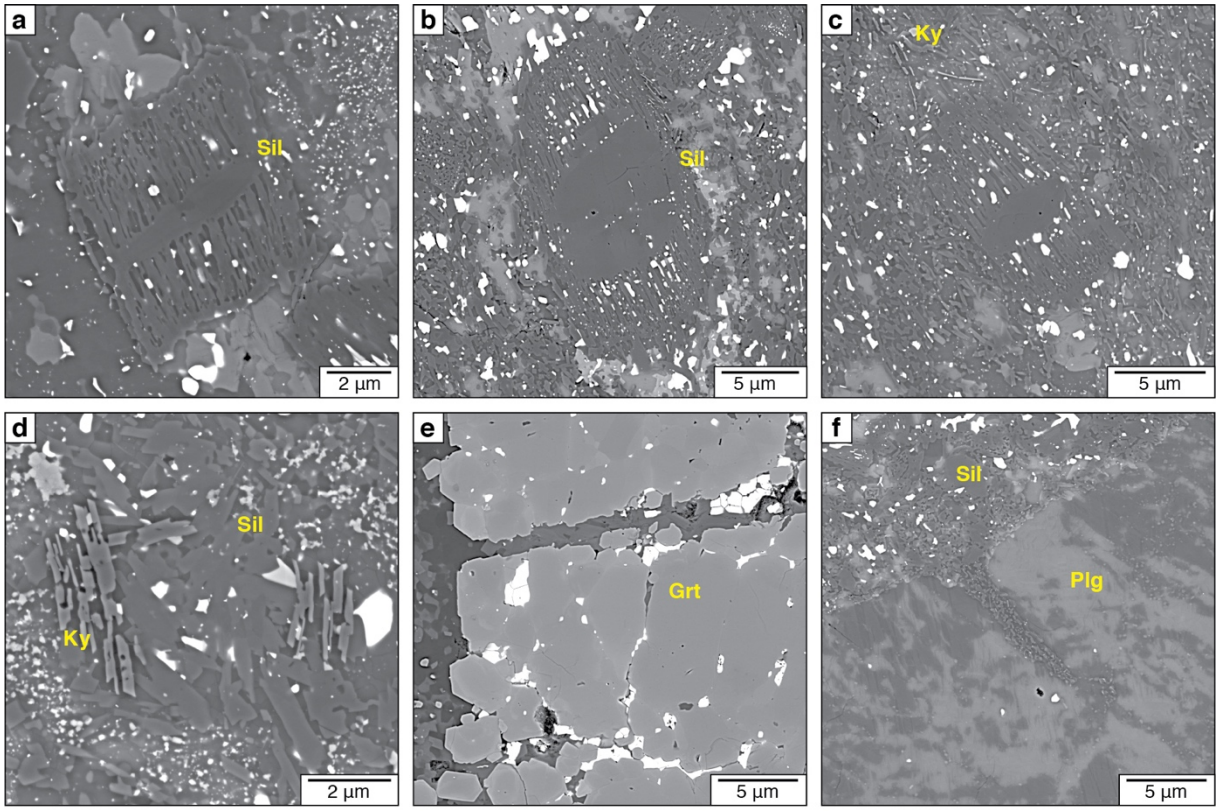

Fig. 6 | Mount Fraser, pseudotachylyte microstructures. a, b, sillimanite microlites, with thin needles overgrowing sillimanite clasts. **c, d,** micrometric kyanite crystals. **e,** healed cataclastic garnet at the selvages of the pseudotachylyte injection vein. The fragments are highlighted by a light-colour halo. **f,** small injection vein departing perpendicular from the main injection vein. The vein is filled by sillimanite and probable kyanite.

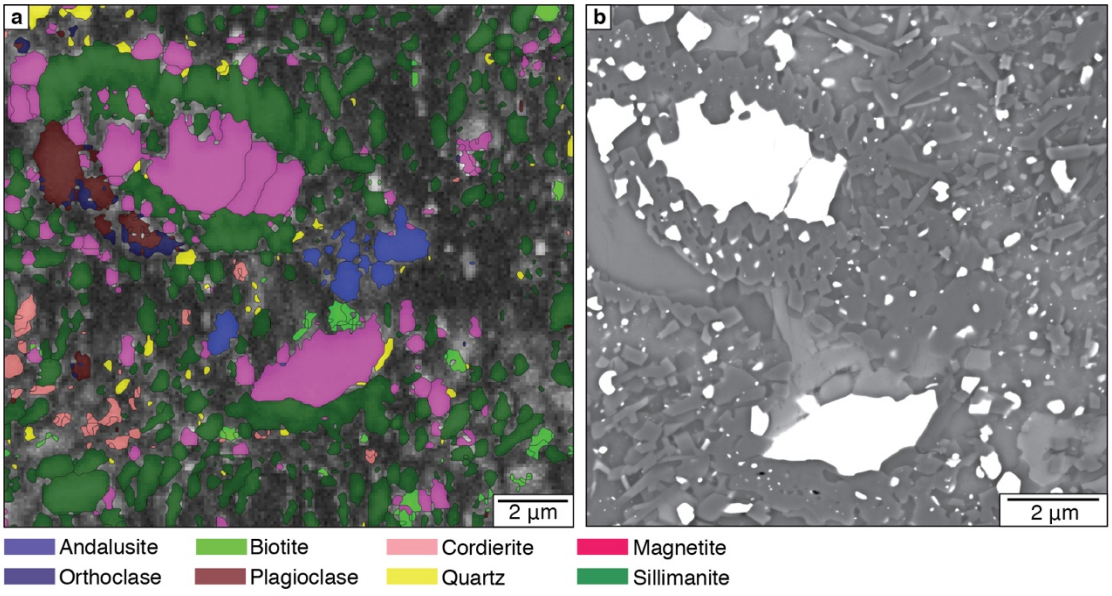

Fig. 7 | Andalusite in a pseudotachylyte from Mount Fraser. a, EBSD phase map. **b,** BSE image of the area mapped with EBSD. Andalusite and sillimanite are hard to distinguish without the help of EBSD.

small holes due to incomplete growth (Fig. 6c, d). Small euhedral garnet crystallises around garnet clasts, identifiable by a slightly different grey-tone, in proximity of healed shattered host-rock garnet (Fig. 6e). Rare aggregates of micrometric andalusite are present, with rounded edges but resembling sillimanite lozenges in shape, thus making them difficult to identify (Fig. 7). The real abundance of andalusite is probably highly underestimated in these samples due to the difficulty in recognising it without diffraction methods like EBSD. Host rock plagioclase crosscut by a pseudotachylyte injection vein is intruded by small subsidiary injection veins departing perpendicularly from the principal one (Fig. 6f). These injections, only a couple of microns in thickness, are filled by submicrometric elongated and lozenge-shaped microlites, most likely sillimanite and kyanite.

5.3 Kelly Hills

A pluri-centimetric injection vein normal to the gneiss foliation and some relatively isolated fault veins were selected for the microstructural investigation among the several pseudotachylytes, sheared and unsheared, that affect the rocks and mutually crosscut in a disordered pattern without clear relationships.

Host rock microstructure

The host rock is characterized by the alternation of quartz-feldspars and sillimanite-cordierite rich layers, with sparse elongated garnets and abundant Fe-Ti oxides. Biotite is rare. Kyanite is present while andalusite, differently from SB and FR samples, is never observed. Cordierite is abundant in the host rock but shows signs of destabilization less frequently than in SB. It is typically overprinted by sheaves of acicular kyanite crystals associated with abundant magnetite, quartz and scarce biotite (Fig. 8a, b, c). Where cordierite is not fractured the reaction is hampered and also late pinitization is less frequent. Sillimanite, as already observed in the other localities, does not react, even where intensely fractured or in contact with the pseudotachylyte. Garnet is present in big euhedral crystals elongated and aligned with the cordierite-sillimanite rich layers. The host rock is affected by

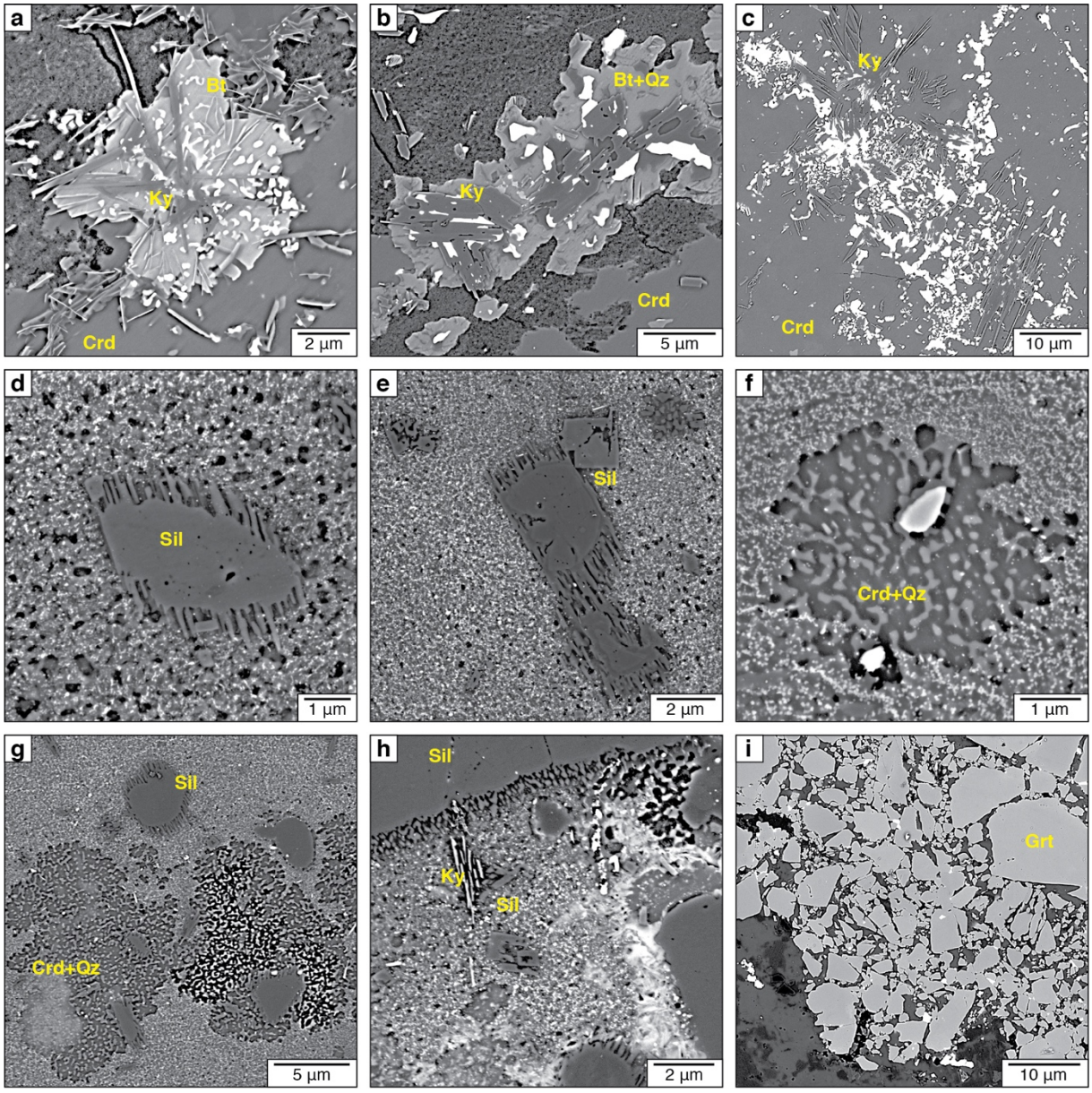

Fig. 8 | Kelly Hills host-rock and pseudotachylyte microstructures. a, b, c, host-rock cordierite substituted by quartz, biotite, kyanite and magnetite in various relative abundances. **d, e,** sillimanite microlites in pseudotachylyte vein with unresolvable matrix. **f,** cordierite microlite intergrowth with quartz. **g,** cordierite and sillimanite microlites. **h,** kyanite microlite. **g,** cataclastic garnet at the selvages of a pseudotachylyte fault vein. Locally garnet is partially recrystallized producing euhedral shapes.

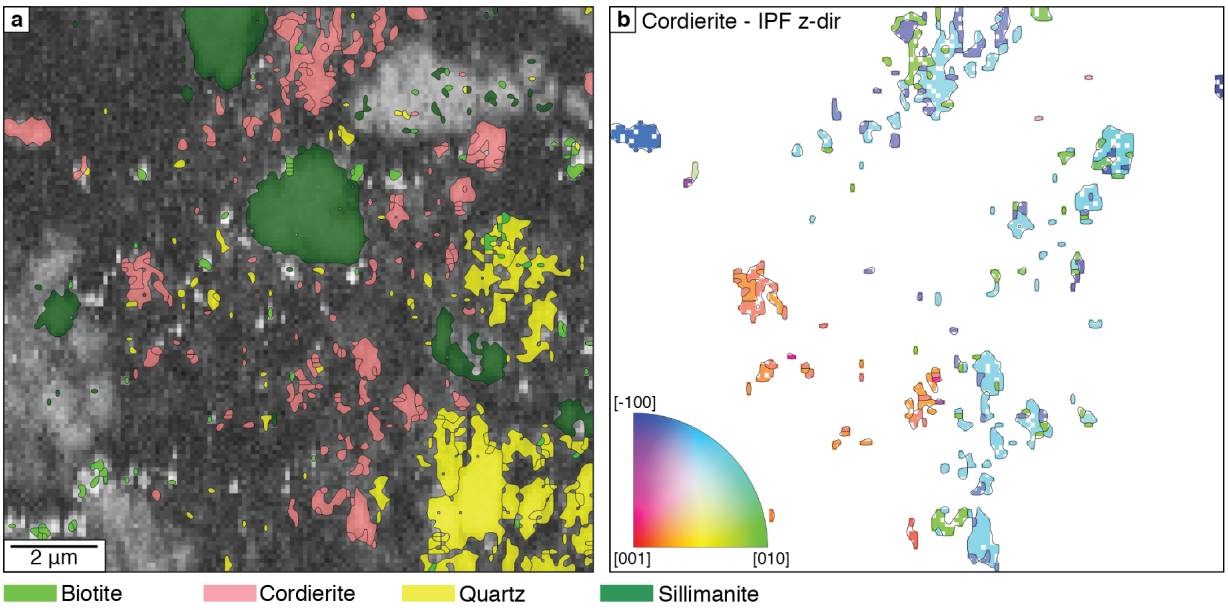

Fig. 9 | EBSD map of Kelly Hills pseudotachylyte. a, phase map plotted over EBSD band contrast. **b,** cordierite orientation map colour-coded according to the inverse pole figure in the bottom left corner

pervasive fracturing, often with micrometric displacements. Fractures are associated with abundant Fe-Ti oxides that locally seals the shattered rocks along fractures.

Pseudotachylyte microstructure

An unsheared pseudotachylyte injection vein preserves the original quench microstructure. It is largely composed of a homogeneous unresolvable matrix made of nanometric microlites with scarce droplets of oxides. Clasts of the main host rock minerals are present but not abundant. Microlites are less abundant than in SB. The most common ones are microlites of sillimanite that overgrow in thin elongated needles at the opposite sides of sillimanite (Fig. d, e). Cordierite microlites are widespread, constituting spherulitic aggregates intergrowth with quartz and often surrounding quartz or sillimanite clasts (Fig. 8f, g; Fig. 9). Rare micrometric microlites of kyanite are also present (Fig. 8h). Andalusite was never observed in the pseudotachylyte. Cauliflower garnets is absent, but where garnets are pulverized along the selvages of the pseudotachylyte, they are locally rimmed and sealed by newly crystallized garnet in a micrometric layer (Fig. 8i).

6. CHEMISTRY OF RELEVANT PHASES

Chemical composition of cordierite (Fig. 10), garnet and, where relevant, of other phases in the studied samples are briefly reported here. Some compositions may be spurious due to the small grain size of microlites, commonly smaller than the spot size of the SEM.

Sentinel Bore — Host rock cordierite is rich in Mn, with (Mn/(Fe+Mg+Mn) ~ 0.1 (Fig. 10). Ilmenite contains up to 10 wt% Mn. Garnet is rich in Mn and Fe with an average composition of spessartine 44.9%, almandine 39.1%, pyrope 13.7% and grossular 2.3%. There are no other Mn-bearing minerals, with biotite containing only a maximum of 0.5% of MnO. Host-rock andalusite is Mn-free but contains about 1 wt% of FeO. Host-rock granulite facies biotite contains 2.4 – 3.4 % TiO_2 while biotite resulting from the breakdown of cordierite is Ti-free. Host-rock biotite has more Fe and less Mg than Cordierite-derived biotite (on average 9.7 % and 7.5 % FeO and 16.9 % and 17.9 % MgO, respectively).

Mount Fraser — Cordierite crystallising from pseudotachylyte melt is almost free of Mn with an average Fe/(Fe+Mg+Mn) ratio of ~0.3. Granulite facies garnet composition is on average almandine 62.5 %, pyrope 31.5 %, spessartine 2.6 % and grossular 3.4 % and is not appreciably different from the partially healed cataclastic garnets in the pseudotachylyte.

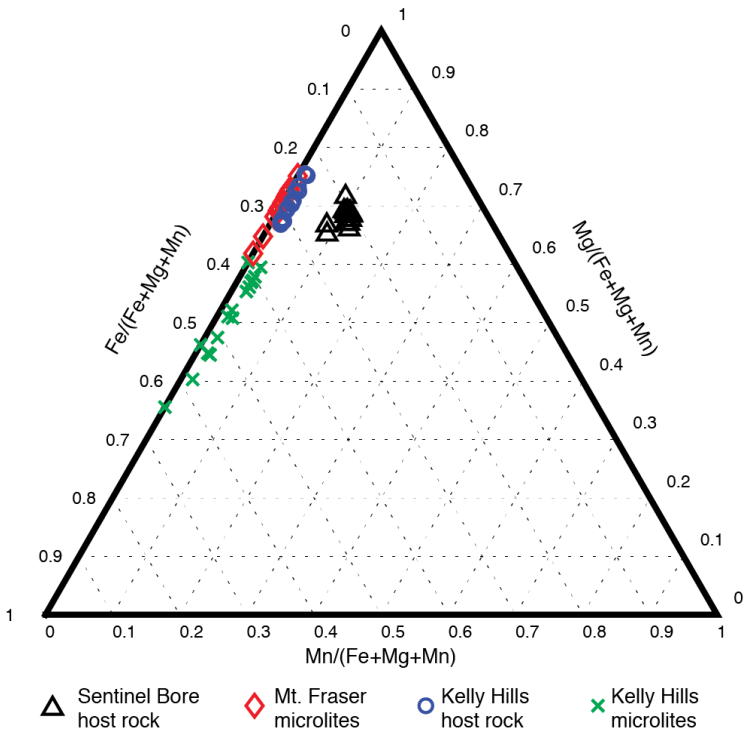

Fig. 10 | Cordierite compositions. Ternary plot showing the relative abundance of Fe, Mg and Mn in host rock and microlitic cordierites.

Kelly Hills — Cordierite has very low Mn content, with Mn/(Fe+Mg+Mn) < 0.02. There is a variation in Mg and Fe ratios in host-rock cordierites and cordierites crystallizing from the pseudotachylyte, with the latter richer in iron and poorer in Mg (on average Fe/(Fe+Mg+Mn)~0.29, Mg/(Fe+Mg+Mn)~0.71 and 0.48, 0.52 for host-rock cordierites and microlitic cordierites respectively). Garnet is Fe-rich, with average composition of almandine 59.3 %, pyrope 26.1 %, spessartine 11.5 % and grossular 3.1 %.

7. DISCUSSION

7.1 Crystallization sequence during quenching of a pseudotachylyte

The crystallization sequence of microlites is influenced by several parameters, many of which may vary dramatically throughout the veins both in time and space. Crystallization takes place from a superheated melt that quenches over a very short time span (seconds to minutes), giving rise to overstepping and crystallization out of equilibrium (Logfren, 1974; Lin, 1994). The process of comminution related to the dynamic earthquake rupture propagation and seismic slip preceding frictional melting, the temperature of the melt and the mechanical and thermal shock properties of the host rock minerals all affect the survival (or disappearance) of the minerals as clasts in the frictional melt. The presence or absence of nucleation seeds (clasts) may play a critical role in promoting microlite crystallization or in resulting in the absence of a mineral phase among the microlites, respectively (Papa et al., 2018). In the case of thick pseudotachylyte veins an internal textural and compositional zonation can develop, due to the faster quenching at the vein selvages. The cooling rate, that evolves rapidly in the quenching melt, influence elements diffusivity and, consequently, the extent of crystallization of the mineral phases. As crystallization proceeds, the pseudotachylyte melt is depleted of the chemical elements forming the early crystallized microlites, and this may change the type of microlites crystallizing at later stages. Small amount of water initially incorporated in the melt can eventually be released during progressive crystallization with formation of hydrous minerals in the latest stages of crystallization.

The microstructures described in the injection vein from the SB locality suggest a specific crystallization sequence for a pseudotachylyte melt derived from a peraluminous host rock. As discussed above, this sequence of crystallization may vary significantly as a function of numerous parameters in the complex system of a quenching frictional melt. In the SB sample the first mineral phase that crystallized from the superheated melt was sillimanite, reflecting the fact that sillimanite is the Al_2SiO_5 polymorph stable at high temperature and that the pseudotachylyte include abundant sillimanite clasts. As the melt cooled down andalusite started crystallizing in typical spherulitic intergrowth of andalusite-quartz single crystals typical of many symplectite aggregates. The single crystallographic orientations of andalusite and quartz in the aggregates and their size implies a relatively high mobility of Al and Si in the quenching melt. Availability and mobility of Al was higher in the middle of the vein than at the vein selvages due to the higher temperature and is reflected in the larger size of the andalusite spherulites in the vein core. After andalusite crystallization, residual melt of a K-rich composition crystallized as a cryptocrystalline matrix with patchy rims of crystallized plagioclase and K-feldspar surrounding the spherulites. We infer that this stage was also marked by release of the dissolved water in the melt that altered andalusite to biotite and favoured recrystallization of the intergrown quartz vermicules. Kyanite most likely crystallized at this stage since being mainly grown on the biotite replacing andalusite and locally overlapping sillimanite. Rare clasts of kyanite are also overgrown implying that kyanite was stable during faulting and it is not a later overprint. Remnants of the melt, depleted in Si and Al, fill the remaining volume of the vein producing a nanometric, unresolvable matrix with scattered droplets of Fe-Ti oxides.

Cauliflower garnet includes all the aluminosilicate minerals. Andalusite included in a cauliflower garnet share the crystallographic orientation of nearby andalusite aggregates (fig. 5c), suggesting that garnet crystallization took place toward the end of melt quenching. The garnet shape is locally similar to that of the spherulitic aggregates suggesting that, rather than a phase crystallizing from the melt, garnet may have substituted biotite, as observed for the host-rock biotite. In contrast, garnets in the fault vein, with the clasts at the core highlighted by a bright nanometric rim, clearly shows evidence of crystallization from a melt.

In the other pseudotachylyte samples described in this study the sequence of microlite crystallization is more difficult to define. However, in all examples sillimanite microlites crystallized first during the peak in the frictional melt thermal transient. This is especially evident in FR where sillimanite microlites are abundant across the entire vein. In the FR sample, andalusite is more difficult to identify and was only identified by EBSD analysis; however, the andalusite appears as a morphological evolution of sillimanite microlites and we infer a similar sillimanite to andalusite sequence of crystallization as in the SB locality. Pseudotachylyte in the KH locality does not contain andalusite and instead contains abundant cordierite microlites without a clearly recognisable crystallization sequence. The difference between the KH and SB and FR localities may reflect a slight change in P-T conditions.

7.2 P-T estimates for the pseudotachylyte zone of the WT

The appearance of index minerals crystallizing from the melt of a quenched pseudotachylyte, with simple chemistry, well-known stability fields and not excessively influenced by other coexisting phases can be used to constrain the ambient pressure at the time of faulting despite the non-equilibrium conditions of crystallization. Microlites of andalusite in pseudotachylytes from SB and FR mark an upper pressure limit of approximately 0.45 GPa, the Al_2SiO_5 triple-point pressure (Pattison, 1992; Cesare et al., 2003).

At SB locality, andalusite is associated with kyanite microlites. Kyanite mainly crystallized over the altered spherulites, but microlites overgrowing former kyanite clasts are also present. The occurrence of rare kyanite clasts testify that kyanite was stable before and during seismic faulting and it is not only a later overprint. The hopper-shape of some kyanite microlites is also typical of crystallites directly precipitated from a quenched melt rather than by metamorphic crystallization. In the host rock andalusite and kyanite also coexist together as products of the breakdown of cordierite that took place predominantly along fractures associated with pseudotachylyte development. The coexistence of andalusite and kyanite in the pseudotachylyte and in the host rock further increase the resolution of the pressure estimate, limiting the possible states in the P-T space to those surrounding the

coexistence curve of andalusite and kyanite (i.e. at pressure less than 500 MPa at decreasing temperature). Unfortunately, temperature cannot be estimated directly from the quenched pseudotachylyte, as the main factor controlling crystallisation is the coseismic thermal transient during which temperature increased from ambient to > 1000 °C almost instantaneously and then cooled in a few tens of seconds. For the mylonites along the WT, Wex et al. (2017) estimated synkinematic temperatures in the range 520–620 °C, compatible with temperatures of stability of coexisting andalusite and kyanite (i.e. not higher that the Al_2SiO_5 triple point temperature, ca. 550 °C). Camacho et al. (2001), based on $^{40}Ar/^{39}Ar$ and Rb/Sr ages of >800 Ma preserved in biotite, proposed that the entire Fregon domain never reached ambient temperatures higher than ca. 450 °C during the Petermann Orogeny. Temperatures in this range are consistent with the possible pressure conditions inferred for the pseudotachylytes.

The absence of andalusite in the samples from the KH locality may signify that pressure was slightly higher or the temperature was lower than in the other localities. The KH pseudotachylytes contain cordierite whose composition (ca. 0.5 #Mg) suggests a crystallization pressure ≤ 0.5 GPa (Holdaway and Lee, 1977; Newton and Woods, 1979), therefore not markedly higher than in the other studied localities.

7.3 Geometry of the Woodroffe Thrust

The WT outcrops in the central part of the Musgrave Ranges, a remote area that largely falls inside the boundaries of the Anangu Pitjantjatjara Yankunyatjatjara (APY) Lands of restricted access. For this reason, studies on the tectonic evolution of the region are not abundant. Furthermore, the geological history of the central Australia, started about 1600 Ma and characterized by three major orogenies (Musgravian, Petermann and Alice Springs orogenies) and a protracted condition of crustal shortening in an intracontinental setting, is complex (Wade et al., 2008; de Gromard et al., 2018). Thus, the understanding of the geological evolution of the WT is still incomplete and the patchy data may lead to contrasting interpretations.

Previous pressure estimates by Wex et al. (2017) for the northern outcrops of the WT (0.8–1.1 GPa) were based on conventional geobarometry on metamorphic assemblages in the footwall mylonites. As clearly stated by the authors, those estimates are potentially affected by large (> 0.3 GPa) errors due to not-ideal mineral assemblages that may lead to overestimates. The strategy we followed was to examine peraluminous rocks where the stability of the different aluminosilicate polymorphs could help better constrain the ambient pressure conditions during the formation of pseudotachylyte. Considering the fine grain-size of these rocks the use of a modern high-resolution FE-SEM was critical for imaging and mineral phase identification. For the first time we were able to identify the occurrence of andalusite, kyanite and sillimanite microlites in the pseudotachylytes of 2 northern outcrops of the WT (SB and MF localities) and to establish the relative sequence in crystallization within the pseudotachylyte melts. We infer that sillimanite microlites grew first during the thermal peak of the melt followed by andalusite and kyanite crystallization reflecting the ambient pressure conditions of < 0.45 GPa. Therefore, the pseudotachylytes in the northern section of the WT developed at a shallower depth (approximately 18–20 km) than what was previously estimated from the mylonites (ca. 30–40 km; Wex et al., 2017).

It is reasonable to assume that pseudotachylyte-producing seismic faulting in the hanging wall and mylonitisation in the footwall took place coevally at the same pressure conditions. Although mylonitisation involved mainly footwall rocks, the hanging wall and the basal thick layer of pseudotachylytes were also involved (Camacho et al., 1995; Wex et al., 2018). These mylonitised hanging wall rocks are affected by several generations of pseudotachylytes cyclically overprinting mylonites and affected by ductile deformation (Camacho et al. 2015; Wex et al., 2017). These spatial relations support the idea that mylonites and pseudotachylytes along the WT developed coevally during the Petermann orogeny.

A non-coeval development of the structures, with pseudotachylyte production occurring syn- to post-mylonitisation during the exhumation along the WT towards shallower crustal levels was hypothesized by Lin et al. (2005). However, Camacho et al. (1995) already noticed that the scarce presence of pseudotachylytes in the mylonite zone is in contrast with such hypothesis, since a weak

planar layer extending continuously for tens to hundreds of kilometres would represent the ideal precursor for earthquake rupture nucleation and propagation, imposing the pseudotachylytes to concentrate in the footwall mylonites rather than in the undeformed strong hanging wall. Thus, despite the protracted activity of the WT in a long-standing context of crustal shortening (de Gromard et al., 2019) most pseudotachylytes probably were not younger than the mylonitization.

According to our new pressure estimates, the WT would be steeper than previously described and in line with common thrust geometries, dipping at an approximate angle of 20–25 ° (considering an average rock density of 2700 kg/m^3, no relevant paleo-topography and a distance of 60 km between the northernmost and southernmost outcrops). The slight P-T variations along strike in the WT, as recorded by the absence of andalusite in KH locality, may be explained assuming a complex, non-planar structure of the thrust, with undulations and consequent non-even exhumation during Petermann orogeny (Raimondo et al., 2010).

8. CONCLUSIONS

In this work we investigated peraluminous gneisses rich in pseudotachylytes from the immediate hanging wall of the Woodroffe Thrust in its northernmost exposures. We described microlites of the three Al_2SiO_5 polymorphs coexisting together in a pseudotachylyte and show that they crystallised from the quenching melt in a very short time. While sillimanite crystallization is due to the high coseismic thermal transient, the crystallization of andalusite and kyanite during quenching reflects the ambient pressure of < 0.5 GPa. Farther west, at similar latitude, in absence of andalusite, pseudotachylyte formation has been inferred to have occurred in an overlapping pressure range by the crystallization of cordierite. These new pressure constraints are at odds with previous estimates obtained from conventional geobarometry on footwall mylonites. Based on these new observations and given the coevality of hanging wall pseudotachylytes and footwall mylonites we propose that our pressure estimates represent the average pressure during thrusting. This implies that the WT dip was steeper (20–25 °) than previously inferred (ca. 6 °). The structural evolution of the Musgrave Ranges during the Petermann Orogeny may thus need to be revisited accounting for our new observations.

With this work we also want to raise attention to the importance of proper pressure estimates for (supposedly-) deep-seated pseudotachylytes, that should be obtained directly from the quenched mineral assemblages to ensure reliability.

Chapter 2: On-fault earthquake energy density partitioning from shocked garnet in an exhumed seismic mid-crustal fault

Toffol, G.[1], Pennacchioni, G.[1], Menegon, L.[2], Wallis, D.[3], Faccenda, M.[1], Camacho, A.[4], Bestmann, M.[5]
[1] University of Padova, Department of Geosciences, Padova, Italy
[2] University of Oslo, Department of Geoscience, Oslo, Norway
[3] University of Oxford, Department of Earth Sciences, Oxford, UK,
[4] University of Manitoba, Department of Geological Sciences, Winnipeg, Canada
[5] University of Vienna, Department of Geology, Vienna, Austria

A slightly different version of this chapter is currently under evaluation in the journal Science Advances.
Authorship contribution statement:
GT: Conceptualization, Data collection, Interpretation, Writing – original draft, Writing – review & editing. **GP**: Conceptualization, Interpretation, Writing – review & editing, Supervision. **LM**: Conceptualization, Writing – review & editing, Supervision. **DW**: Writing – review & editing. **MF**: Writing – review & editing. **AC**: Writing – review & editing. **MB**: Data collection.

Abstract

The energy released during an earthquake is mostly dissipated in the fault zone and subordinately as radiated seismic waves. The on-fault energy budget is partitioned into frictional heat, generation of new grain surface by microfracturing, and crystal lattice distortion associated with dislocation defects. The relative contribution of these components is debated and difficult to assess, but this energy partitioning strongly influences earthquake mechanics. We use high-resolution scanning electron microscopy techniques, especially to analyse shocked garnet in a fault host-rock, to provide the first estimate of all three energy components for a seismic fault patch exhumed from midcrustal conditions. Fault single-jerk seismicity is recorded by the presence of pristine quenched frictional melt. The estimated value of energy per unit fault surface is ~ 13 MJ/m^2 for heat, which is predominant with respect to both surface energy (up to 0.29 MJ/m^2) and energy associated with crystal lattice distortion (0.02 MJ/m^2).

1. INTRODUCTION

Seismogenic environments build up the highest tectonic differential stresses. High ambient differential stresses are associated with elastic strain accumulated during inter-seismic periods and partially released during earthquakes. Differential stresses of several hundred megapascals may be achieved by tectonic loading at the brittle-ductile transition in the upper crust (10–15 km depth) (Behr & Platt, 2014). These stresses can reach gigapascal magnitudes in dry rocks of the lower continental crust and in the upper lithospheric mantle (Burov and Diament, 1995; Burov, 2011; Jamtveit et al., 2019; Campbell et al., 2020; Toffol et al., 2022). Once critically stressed, a fault may yield seismically partially releasing the accumulated elastic energy in a few seconds. Yielding results in abrupt, large-magnitude, local (near- or on-fault) stress changes during (i) propagation of the earthquake rupture tip at velocities of kilometres per second (Reches and Dewers, 2005), and (ii) frictional fault slip at velocities of metre per second resulting in frictional heating and, eventually, melting of silicate-rich host rocks (Di Toro and Pennacchioni, 2004, Bestmann et al., 2012, Papa et al., 2018) (Fig. 1a).

These high-stress processes account for dissipation of the largest amount of the released energy of an earthquake as work spent in the fault zone (E_{FZ}), while a fraction (< 20% of the total energy budget) is radiated as seismic waves (E_{R}) (Okubo et al., 2019). Determining how energy is consumed in the fault zone and what is the contribution of every process is fundamental to properly understand the mechanics of earthquakes (Cocco et al., 2023). The energy budget is commonly expressed in terms of work density W_{FZ}, i.e. the energy spent per area of slipping fault (J/m^2), and consists of different contributions

$$W_{\mathrm{FZ}} = W_{\mathrm{FH}} + W_{\mathrm{FS}} + W_{\mathrm{CP}}, \quad (1)$$

where: W_{FH} is the frictional heat, W_{FS} is the fracture-surface energy, i.e. the energy consumed to fracture the rock and propagate the rupture, and W_{CP} is the energy consumed in crystal-plastic and elastic straining of mineral lattices (Fig. 1b). These quantities, unlike the energy radiated as seismic waves, can only be estimated indirectly during an earthquake. Most of the available estimates of the fault-zone work come from laboratory experiments and interpretations of seismological observations

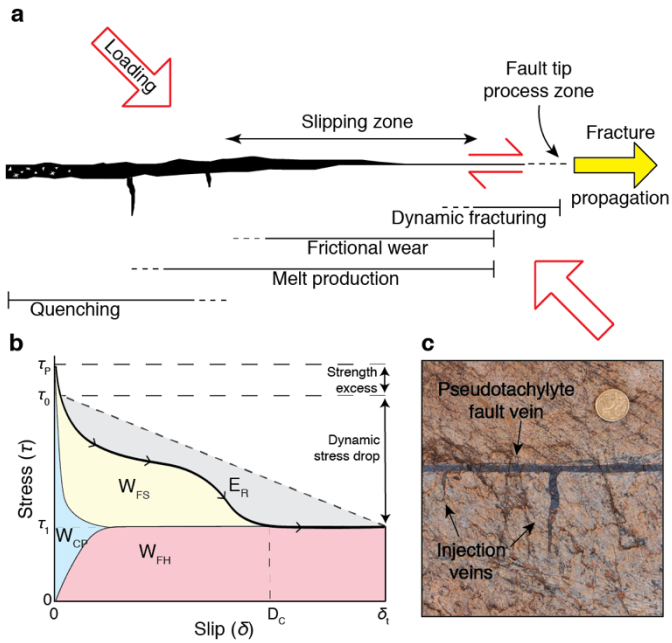

Fig. 1 | Stages of the earthquake cycle. a, Cartoon illustrating the different processes associated with a fault during the earthquake cycle, including the interseismic loading stage and the coseismic stages of fracture propagation, frictional slip and melting, and the final stage of fault healing by quenching of the pseudotachylyte melt (redrawn after Petley-Ragan et al., Mancktelow et al.). **B,** Earthquake energy budget per unit fault area for a simplified slip-weakening model represented in the shear stress (τ) versus slip (δ) space. The black curve with arrowheads shows the evolution of stress from the peak strength (τ_p) to the final value (τ_1) reached at the critical distance D_c and maintained until the end of slip (δ_1). The total released energy is represented by the area below the diagonal dashed line and comprised of the radiated energy (E_R) and the energy dissipated on fault by fracturing, crystal-plastic straining of the minerals and frictional heating (the area below the thick black curve). Energy components are not to scale. Modified after Johnson et al. to include W_{CP}. **c**, Pseudotachylyte fault and injection veins produced by frictional melting during seismic fault slip in a felsic granulite from the hanging wall of the Woodroffe Thrust (25°59'32'' S, 132° 8' 35'' E).

(see review by Cocco et al., 2023). Only a few studies have inferred these quantities from local observations along natural seismogenic fault zones (Chester et al., 2005; Ma et al., 2006; Pittarello et al., 2008; Johnson et al., 2021). Direct estimates of the on-fault energy budget from exhumed seismogenic faults may help to clarify the dynamics of coseismic processes in different structural settings and to bridge field observations and experimental results (Cocco et al., 2023).

The geological record of an earthquake can be exceptionally well preserved in exhumed faults that contain pseudotachylytes, which are quenched frictional melts recognized as the product of seismic slip (Di Toro et al., 2005a; Bestmann et al., 2012; Petley-Ragan et al., 2019; Campbell and Menegon, 2022; Mancktelow et al., 2022) (Fig. 1c). The microstructures of pseudotachylytes and surrounding fault rocks can capture snapshots of the loading history (Trepmann & Stöckhert, 2001; Brückner et

al., 2021; Campbell and Menegon, 2022), as well as the seismic rupture propagation and slip (e.g., fracturing and pulverization: Hawemann et al., 2019; Campbell and Menegon, 2022; Petley-Ragan et al., 2018, 2019; Mancktelow et al., 2022). Features like the presence of pulverized minerals, the fault roughness and the thickness of pseudotachylyte fault veins have been used to investigate earthquake mechanics and obtain mechanical parameters, such as the dynamic friction coefficient, the frictional heat, and the fracture energy. In particular, the study of a single-jerk pseudotachylyte fault vein, well characterized from a (micro-)structural point of view, is useful to associate the measured energy densities to a single event (e.g., Pittarello et al., 2008; Di Toro et al., 2005b). With this approach, uncertainties on the number of earthquakes responsible for the fault structure (Johnson et al., 2021, Chester et al., 2005) are avoided, although the information is necessarily local and limited to a small fault patch.

Although evidence of crystal-plastic and elastic effects in fault rocks surrounding pseudotachylytes have been described (e.g., Bestmann et al., 2012), the contribution of W_{CP} in the energy budget has never been properly quantified, as this requires precise measurements of elastic strains and the density of dislocations. High-angular resolution electron backscattered diffraction (HR-EBSD)—a material science technique only recently applied in geosciences—provides a new way to measure, with high precision and spatial resolution, the residual strains and dislocations stored in the lattices of minerals (Wilkinson et al., 2006; Wallis et al., 2019). Here, we present the first application of HR-EBSD to garnets that were seismically shocked at mid-crustal levels. The sluggish dislocation mobility in garnet at the ambient conditions of faulting, the absence of twinning and cleavage, and the high fracture toughness make garnet a suitable candidate to preserve coseismic residual strains and high densities of dislocations. Combined with estimates of W_{FH} and W_{FS} obtained from the study of the pseudotachylyte and pulverized portions of the host rock we provide a complete energy budget of the fault-zone work during a single earthquake revealing a precise hierarchy in the contributions of the different work-density components of an earthquake.

2. METHODS

2.1 Sample preparation and data acquisition

The thin section was mechanically polished and finished with a colloidal-silica suspension to ensure a damage-free surface required for high-angular resolution electron backscattered diffraction (HR-EBSD).

Backscattered-electron (BSE) imaging was performed with a TESCAN Solaris field emission gun scanning electron microscope (FEG-SEM) at the Department of Geosciences, University of Padova, equipped with a mid-angle BSE detector. Working conditions were: 5 kV acceleration voltage, 300 nA beam current and 4 mm working distance. Electron backscattered diffraction (EBSD) and energy-dispersive X-ray spectroscopy (EDS) data were acquired with a Hitachi SU500 FEG-SEM equipped with Dual Bruker Quantax XFlash 30 EDS system and a Bruker e-Flash HR EBSD system at the Goldschmidt Laboratory, Department of Geosciences, University of Oslo. Preliminary EBSD maps and maps for HR-EBSD were acquired and indexed with Esprit software and processed with the MTEX toolbox version 5.6.1 in MATLAB® (Hielscher and Schaeben, 2008).

EBSD maps were acquired with an acceleration voltage of 15 kV, working distance of 18 mm, sample tilt of 70° and detector tilt of 1.9°. Preliminary EBSD maps have step sizes in the range 0.8–0.3 μm. EBSD maps for HR-EBSD analysis have step sizes of 0.25 and 0.41 μm. For HR-EBSD, maps were acquired saving the patterns at a resolution of 1200×1200 pixels and subsequently processed with the commercial software CrossCourt Rapide 4.5.

EBSD maps for measurements of clast size were acquired with a TESCAN Solaris equipped with an Oxford Symmetry EBSD detector and indexed with Oxford AZtec software. Acquisition conditions were 20 kV of acceleration voltage, 10 nA of current, 15 mm of working distance and step size of 0.15 μm.

Chemical data were acquired with a Cameca SX100 electron probe micro-analyser equipped with 5 WDS spectrometers at the Department of Geosciences, University of Oslo. Conditions of acquisition were 15 kV acceleration voltage and 15 nA beam current.

2.2 High-angular resolution electron backscattered diffraction analysis.

HR-EBSD is based on cross-correlation between each EBSD pattern within grain and a pattern from the same grain chosen to be a reference. From the measurement of shifts in small regions of interest within the patterns, the rotation and strains of the crystal lattice can be measured with precision on the order of 10^{-4} (Wilkinson et al., 2006). A comprehensive review of HR-EBSD applied to geological materials is provided by Wallis et al. (2019).

EBSD maps were filtered (indexed bands > 6) prior to the cross-correlation, to exclude bad-quality patterns from the analysis. Patterns acquired along fractures or close to surface imperfections (as identifiable from band-contrast maps) were manually checked and deleted if blurred or showing superposition of two different patterns. A subsequent cleaning stage was performed after the first cross-correlation step to exclude other bad patterns previously neglected and subsequently evidenced by high values of mean angular error and HR-KAM (high-resolution kernel average misorientation). A reference point for every grain in the map was automatically selected by the software, initially based on the KAM values from the initial EBSD and, for subsequent cross-correlation stages, on the HR-KAM obtained after the first pass of cross-correlation. Where needed, other references points were added manually to improve the quality of the analysis. If more than one reference point was used, the results were automatically referred to the first reference point considered for each grain in the map by adjusting the others based on the differences in the measurements obtained in the overlapping regions for the respective reference points. Cross-correlation of each pattern with the reference pattern was performed considering 40 to 100 regions of interest (256 x 256 pixels in size) per pattern and applying the robust fitting procedure (Britton and Wilkinson, 2011). Cross-correlation is performed in Fourier space, and low- and high-pass filters were applied to the patterns to reduce the noise level of the measurements. An effective pixel size of 18.23 μm (calibrated on an unstrained Si crystal) was used to correct the shifts in the pattern due to scanning of the beam across the map area. Results were filtered to exclude pixels with bad quality of cross-correlation indicated by normalised peak heights in the cross-correlation function < 0.3 and pixels for which the displacement-gradient tensor was a poor fit to the measured shifts with mean angular error > 0.2292 ° (Britton and

Wilkinson, 2011). The mean angular error, to assess the quality of the analysis, and the high-resolution kernel average misorientation, useful to evaluate the contribution of noise in the analysis, are reported in App. 2 Fig. 1.

Residual stresses were calculated from the measured elastic strains using Hooke's law and considering elastic constants of garnet reported by Babuska et al. (1978). Values of residual stress are relative to the stress state at the reference point used for the cross-correlation. As most of the selected reference patterns come from areas affected by some residual elastic strains, the components of the residual stress tensor were normalized to their mean values for every grain to reduce the effect of the choice of reference pattern on the measurements (Mikami et al., 2015). Only the in-plane components of the stress tensor are presented since, given the assumption of plane-strain conditions required for the calculation of the strain matrix, the third dimension is not explorable with HR-EBSD. The direction perpendicular to the sample surface is also almost completely relaxed during sample preparation.

Probability plots are presented to show characteristics of the stress distributions in the maps following an approach similar to Wallis et al. (2021). Probability distributions are plotted considering a binwidth of 20 MPa. The distribution of normalized stresses is characterized by normal probability plots and the shape of the tails are studied with plots of the restricted second moments of the distributions (Groma et al., 1998; Wilkinson et al., 2014). Normal probability plots are plotted with the Y-axis scaled such that a normal distribution falls along a straight line. Departures from a straight line, indicating a deviation from a normal distribution, are typically associated with high stress magnitudes due to presence of dislocations. The restricted second moment (v_2) of the probability (P) distribution is calculated as the integral over restricted ranges of stress as $v_2(\sigma) = \int_{-\sigma}^{+\sigma} P(\sigma)\sigma^2 d\sigma$. A plot of v_2 versus $\ln(\sigma)$ is a straight line at high stress when the probability distribution has the form $P(\sigma) \propto |\sigma|^{-3}$ as expected for the stress field generated by the presence of dislocations, and its gradient is proportional to the total dislocation density (Groma et al., 1998).

2.3 Uncertainties in the calculation of W_{CP} from HR-EBSD data

As discussed above, HR-EBSD cannot measure rotations and strains in the third dimension (i.e. the dimension normal to the thin section). For this reason, total GNDs densities and residual elastic strains are underestimated, affecting the calculation of W_{CP}. Another potential cause of uncertainty in the calculation of $W_{\mathrm{CP}}$is due to the fact that in large portions of the maps, GNDs densities are below the noise level (Wallis et al., 2019). However, since E_{disl} is on average two orders of magnitude smaller than E_{st}, the effect of local overestimates of GND density may be neglected. Statistically stored dislocations (SSD) are also not measurable, but the measured residual elastic strains, being determined both by the presence of GNDs and SSDs, compensate the lack of a direct measure of SSDs.

2.4 Clast-size distributions from EBSD and high-resolution imaging

Four EBSD maps were acquired for grain-size analysis and were processed using MTEX. A threshold angle of 2° was used for the reconstruction to account also for small rotations between neighbour grains due to local shattering and the absence of shearing of the pulverised aggregates. Given the absence of subgrains in the garnets, the choice of a small misorientation angle is appropriate and does not affect the total count of grains. Grains with fewer than 7 pixels were discarded, limiting the measurement to a minimum equivalent radius of 0.22 μm.

Not indexed portions of the EBSD maps were investigated in three sites by high-resolution BSE imaging. Three images (3072×3072 pixels, field of view 25 μm, pixel size ~ 8.1 nm) were acquired in selected domains. Due to varying grey shades in the smaller grains (effect of nano-topographic imperfections and boundary effects), clasts were manually drawn in each figure. The drawn clasts were then measured using the image analysis software ImageJ.

Log-log plots of grain size vs. the cumulative number of grains were plotted for the four EBSD maps together and separately for the three images. The curves were fitted with different segments with slope D_{i}. A cumulative graph to compare the distributions was plotted by normalising every size class by the covered area. The cumulative distribution was considered as fractal with a common D value

of 2.1, considering that, due to limitations in the analysis method, the largest and smallest fragments may be underestimated (Pittarello et al., 2008).

2.5 Calculation of fracture energy

Fracture energy was calculated from the clast-size distribution following the approach proposed by Pittarello et al., 2008. Fracture energy was calculated as $W_{\mathrm{SF}} = A_{\mathrm{SZ}}\gamma$, where A_{SZ} is the new surface area of clasts per unit area of fault produced in the slipping zone and γ is the specific surface energy, γ = 3.551 J/m^2 (Tromans and Meech, 2002).

The measured 2-dimensional clast-size distribution was extrapolated to the corresponding 3-dimensional distribution, transforming the calculated fractal coefficient D into D^* (the 3-dimensional fractal distribution coefficient) following the equation $D^* = D + D'$, with D' in the range 0–1 (Bonnet et al., 2001).

A_{SZ} was calculated following the approach proposed by Pittarello et al (2008). The total surface area in the investigated domain, A_{SZi}, was calculated from the clast-size distribution by

$$A_{\mathrm{SZ}i} = \int_{r_{\min}}^{r_{\max}} 4\pi r^2 dN \approx \frac{4\pi C D^*}{2-D^*}\left(r_{\max}^{2-D^*} - r_{\min}^{2-D^*}\right). \quad (2)$$

A_{SZi} was then extrapolated to the volume of pseudotachylyte corresponding to a square metre of fault ($V_{SZ} = w * 1\mathrm{m}^2$ with w the thickness of the pseudotachylyte fault vein) by multiplying it by the ratio V_{SZ}/V_{SZi}. V_{SZi} is the volume of the fragments, approximated to spheres, of the investigated domain and was calculated from the clast-size distribution by

$$V_{\mathrm{SZ}i} = \int_{r_{\min}}^{r_{\max}} \frac{4}{3}\pi r^3 dN \approx \frac{4\pi C D^*}{3(3-D^*)}\left(r_{\max}^{3-D^*} - r_{\min}^{3-D^*}\right). \quad (3)$$

2.6 Heat calculation

The heat due to frictional heating during seismic slip per unit fault area can be calculated as $W_{\mathrm{FH}} = [H(1-\phi) + c_{\mathrm{p}}(T_{\mathrm{m}} - T_{\mathrm{hr}})]\rho w$, with H the latent heat of fusion, c_{p} the specific heat at constant pressure, T_{m} the maximum temperature of the melt, T_{hr} the temperature of the host rock, ρ the rock

density and ϕ the fraction of clasts in the pseudotachylyte vein (Di Toro et al., 2005b). ϕ was obtained by measuring the area of the clasts in the pseudotachylyte that where identifiable in the thin-section scan. Smaller clasts scattered in the pseudotachylyte matrix and visible only with the scanning electron microscope were neglected. The garnet fraction was extracted from a BSE transect across the entire vein, manually excluding large garnet clasts. Plagioclase and biotite fractions were measured from high-resolution BSE images acquired in homogeneous portions of the pseudotachylyte matrix, excluding micrometric clasts.

T_m, the temperature of the melt, was assumed to be 1450 °C in accordance with the temperatures proposed for superheated frictional melts in an upper crustal pseudotachylyte (Di Toro and Pennacchioni, 2004; Pittarello et al., 2008).

c_p and H are calculated from values for pure minerals ($c_{\mathrm{p}i}$, H_i) considering their relative abundance in the pseudotachylyte. Values of $c_{\mathrm{p}i}$ (1248, 1298 and 1347 $J/K^{-1}kg^{-1}$ for plagioclase, biotite and garnet respectively) were calculated for the given temperature conditions (maximum temperature of the melt, 1450 °C) from the database of Holland and Powell, 1998, considering a pure albite for plagioclase, phlogopite for biotite and pyrope for garnet. Values of H_i for silicates are commonly on the order of 500 kJ/kg (Thompson and Connolly, 1995). We used value of 302 kJ/kg for plagioclase and 453 kJ/kg for biotite from Di Toro and Pennacchioni (2004) along with a value of 500 kJ/kg for garnet.

2.7 Stress during dynamic fracture propagation

We used the asymptotic solution for an in-plane propagating fracture by Freund (1990) to calculate the stress fields surrounding the tip of a mode II fracture. In the 2D reference cartesian coordinate system, the fracture is parallel to the *x*-axis and propagates towards right.

Following Reches and Dewers (2005), two different reference frames are considered to calculate the stress: (i) one centred at the fracture moving tip, where the stress is calculated at every point P(r,θ) with r the distance from the tip of the fracture and θ the angle; and (ii) the other fixed in space where

the stress is calculated at a fixed point P(x,y) away from the passing fracture as a function of time t=x/v, with v the velocity of the fracture tip and x its position along the x-axis.

The stress field is expressed as:

$$\sigma_{ij} = \frac{K_{\mathrm{II}}}{\sqrt{2\pi r}} \sum_{ij}^{II}(\theta, v) \quad (4)$$

with $\sum_{ij}^{\mathrm{II}}(\theta, v)$ representing the angular variations of the stress components for any values of the instantaneous crack tip-speed:

$$\sum_{11}^{\mathrm{II}} = -\frac{2\alpha_{\mathrm{s}}}{D}\left[\left(1 + 2\alpha_{\mathrm{d}}^2 - \alpha_{\mathrm{s}}^2\right)\frac{sin0.5\theta_{\mathrm{d}}}{\sqrt{\gamma_{\mathrm{d}}}} - (1 + \alpha_{\mathrm{s}}^2)\frac{sin0.5\theta_{\mathrm{s}}}{\sqrt{\gamma_{\mathrm{s}}}}\right] \quad (5)$$

$$\sum_{12}^{\mathrm{II}} = \frac{1}{D}\left[(4\alpha_{\mathrm{d}}\alpha_{\mathrm{s}})\frac{cos0.5\theta_{\mathrm{d}}}{\sqrt{\gamma_{\mathrm{d}}}} - (1 + \alpha_{\mathrm{s}}^2)^2\frac{cos0.5\theta_{\mathrm{s}}}{\sqrt{\gamma_{\mathrm{s}}}}\right] \quad (6)$$

$$\sum_{22}^{\mathrm{II}} = \frac{2\alpha_{\mathrm{s}}(1+\alpha_s^2)}{D}\left[\frac{sin0.5\theta_{\mathrm{d}}}{\sqrt{\gamma_{\mathrm{d}}}} - \frac{sin0.5\theta_{\mathrm{s}}}{\sqrt{\gamma_{\mathrm{s}}}}\right] \quad (7)$$

The parameters in the equations are:

$$\alpha_{\mathrm{d}} = \sqrt{1 - v^2/C_{\mathrm{d}}^2}, \quad (8)$$

$$\alpha_{\mathrm{s}} = \sqrt{1 - v^2/C_{\mathrm{s}}^2}, \quad (9)$$

$$D = 4\alpha_{\mathrm{d}}\alpha_{\mathrm{s}} - (1 + \alpha_s^2)^2, \quad (10)$$

$$\gamma_{\mathrm{d}} = \sqrt{1 - (vsin\theta/C_{\mathrm{d}})^2}, \quad (11)$$

$$\gamma_{\mathrm{s}} = \sqrt{1 - (vsin\theta/C_{\mathrm{s}})^2}, \quad (12)$$

$$tan\theta_{\mathrm{d}} = \alpha_{\mathrm{d}} tan\theta, \quad (13)$$

$$tan\theta_{\mathrm{s}} = \alpha_{\mathrm{s}} tan\theta, \quad (14)$$

where C_{d} and C_{s} are the velocity of compressional and shear waves. The solution is valid for fracture velocities below the Rayleigh-wave velocity, $C_{\mathrm{r}} = 0.92\ C_{\mathrm{s}}$.

K_{II} is the stress-intensity factor and determines the magnitude of the crack-tip stress field. For a fracture propagating at equilibrium conditions, K_{II} is related to the energy release rate, G, and the Young modulus, E, by $G = K_{\mathrm{II}}^2/E$. For a dynamic fracture, the relation depends upon the propagation velocity, and can be written as (Freund, 1990)

$$G = \frac{1-\upsilon}{2\mu} A_{\mathrm{II}} K_{\mathrm{II}}^2, \qquad (15)$$

where

$$A_{II} = \frac{v^2 \alpha_s}{(1-\upsilon) C_S^2 D}. \qquad (16)$$

We considered the following material properties: density ρ = 2800 kg/m^3, shear modulus μ = 30 GPa and Poisson's ratio υ = 0.22. The energy-release rate of a propagating fracture can be considered equal to the fracture energy G_c of the host material. We considered a value of G_c of 10^6 J/m^2 compatible with values typical of earthquake ruptures (10^5-10^7 J/m^2) (Rice et al., 2005; Johnson et al., 2021). The velocity of propagation of the fracture has a first-order effect on the magnitude of the tip stress field. For our simulations we considered a velocity of $0.9C_s$, close to the Rayleigh velocity.

3. SAMPLE DESCRIPTION

The studied sample (25°59'48"S, 131°39'48"E) is from the hanging wall of the Woodroffe Thrust (Musgrave Ranges, central Australia), a major east-west-striking, shallowly-dipping, crustal-scale mylonitic zone developed at intermediate crustal levels during the Petermann Orogeny (630–520 Ma) (Camacho and Fanning, 1995; Walsh et al., 2013). The thrust juxtaposes upper-amphibolite/granulite facies rocks of the Fregon Subdomain in the hanging wall with amphibolite-facies granitoids and gneisses of the Mulga Park Subdomain in the footwall (Edgoose et al., 1993; Major and Conor, 1993). Towards the thrust, the Fregon Subdomain contains the largest volumes, worldwide, of tectonic pseudotachylytes (Camacho et al., 1995).

The sample, hosting a 3 mm-thick pseudotachylyte vein, is a felsic granulite composed of quartz, plagioclase, K-feldspar, centimetre-sized garnet, and minor biotite and sillimanite. The pseudotachylyte is pristine, without any overprint by solid-state ductile deformation and alteration. The average composition of the pseudotachylyte is: 61% (by area) plagioclase (andesine), 27% biotite and 12% garnet, plus rare K-feldspar and quartz. Clasts, mainly quartz and feldspars, account for 19.4 % of the total pseudotachylyte area (see App. 2 Fig. 2). The syn-melt flow foliation of the pseudotachylyte, oblique to the boundary (Fig. 2a), is marked by (i) elongated cauliflower-shaped

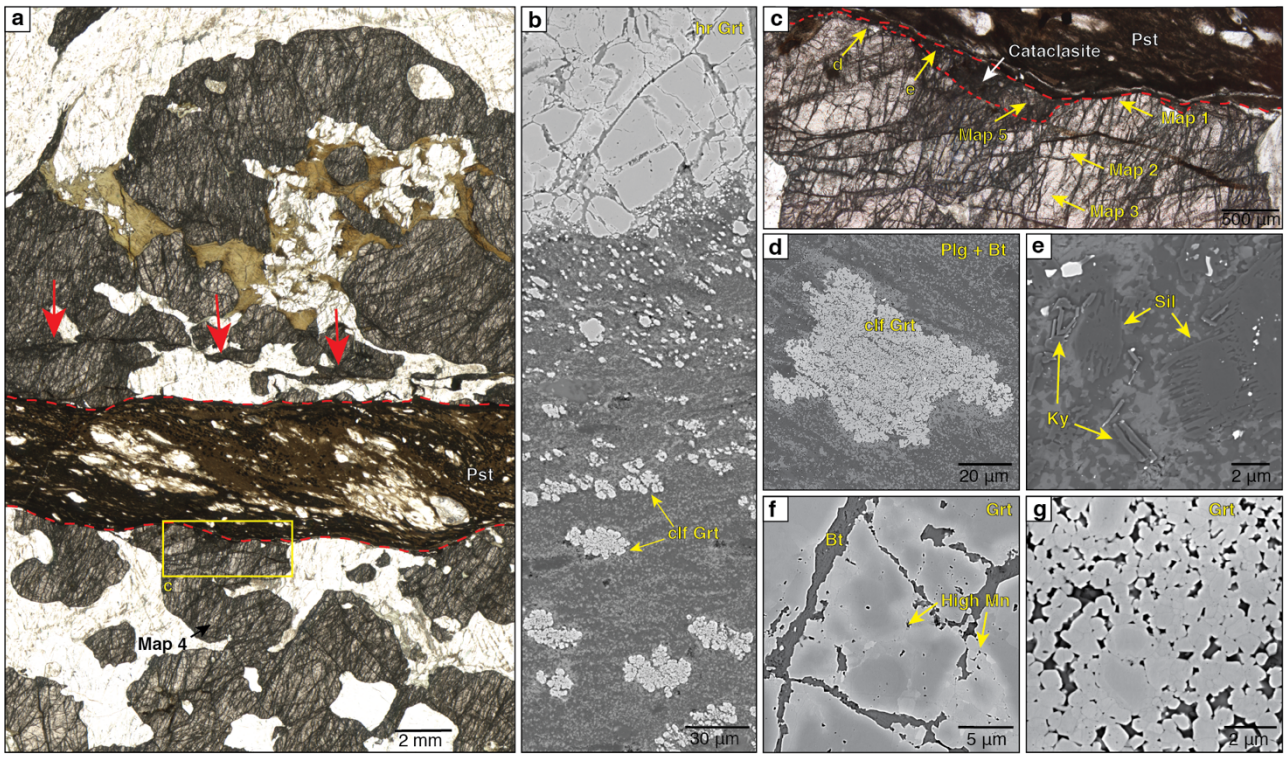

Fig. 2 | Microstructures. **a**, Overview of the pseudotachylyte (Pst) vein crosscutting the host rock fractured garnets with quartz (light coloured) and biotite (brown-green) inclusions. Red arrows indicate auxiliary sharp zones of cataclasis. The location of the Map 4 and the yellow rectangle (enlarged in **c** and including the locations of Maps 1–3 and 5) are shown. **b**, Fractured garnet in the pseudotachylyte host rock and cauliflower-shaped garnets (clf Grt) inside the pseudotachylyte with increasing sizes towards the vein core. **c**, Detail of the host-rock garnet showing locations of Maps 1, 2, 3 and 5. **d**, Cauliflower garnet in the layered plagioclase-biotite matrix of the pseudotachylyte. The matrix has an equant polygonal microstructure, locally with shape preferred orientation of biotite parallel to the flow foliation. **e**, Kyanite (Ky) and sillimanite (Sil) microlites within the pseudotachylyte crosscutting a peraluminous host-rock layer. Sil microlites overgrow Sil clasts from the host rock. **f**, **g**, back-scattered electron images showing details of the fractured and cataclastic garnet close to the pseudotachylyte. Light-grey portions are enriched in Mn. **a** and **c** are visible-light microscope images in plane polarized transmitted light). **B** and **d**-**g** are backscattered electron images.

garnet microlites (locally overgrowing clasts of host-rock garnet) of increasing grain size towards the vein centre (Fig. 2b), and (ii) a local compositional banding of the fine-grained (< 1 µm grain size) biotite-plagioclase (±quartz, ±K-feldspar) matrix (Fig. 2d). Pseudotachylytes from the same sampling outcrop, cutting across peraluminous gneisses, contain abundant microlites of sillimanite and kyanite (Fig. 2e) together with minor andalusite and garnet. This constrains the ambient temperature and pressure of seismic faulting to have been around 500 °C and 0.5 GPa respectively (Toffol et al., 2022; Wex et al., 2017).

The granulitic almandine-rich ($Almandine_{0.66}$ $Pyrope_{0.21}$ $Spessartine_{0.08}$ $Grossular_{0.05}$) host-rock garnet shows the same intense fracturing on both sides of the pseudotachylyte (Fig. 2a–c). The microfractures are arranged in two main sets with slightly different orientations in different garnet grains. Most fractures are filled with biotite and, mostly, do not offset the garnet boundary. The biotite-filled fractures crosscut fractures overgrown, and partially healed, by garnet that is enriched in Mn (up to 8 wt. % from the 2–3 wt. % in the host) (Fig. 2f). These healed fractures are especially developed nearby the pseudotachylyte. Here, garnet is ultra-cataclastic (grain size as small as 0.02 μm in contact with the pseudotachylyte) (Fig. 2g) and the clasts are typically rimmed by new Mn-enriched garnet, resulting locally in a polygonal aggregate with tight, triple grain junctions (Fig. 2f). Similar polygonal aggregates occur along healed microfractures (Fig. 2f) and along sharp auxiliary cataclastic bands, subparallel to the pseudotachylyte vein, across the host granulitic garnet.

4. RESULTS

4.1 HR-EBSD maps result

Five areas (approximately 1900–5200 μm^2) were selected for HR-EBSD mapping. Maps 1–4 are in the host-rock garnet at increasing distances (approximately 0, 0.3 0.6 and 2 mm, respectively) from the pseudotachylyte boundary. Map 5 is within the cataclastic garnet at the contact with the pseudotachylyte (see Fig. 2 and App. 3 Fig. 3 for locations). The five areas were selected after inspection of standard EBSD maps (App. 3 Fig. 3).

The estimated in-plane components (i.e. acting in the thin-section plane) of the residual stress tensor and the geometrically necessary dislocation (GND) densities are shown in Fig. 3 and 4. The stress values are relative to the unknown stress state at the selected reference points, and therefore provide a measure of the spatial heterogeneity in stress rather than absolute values. To provide an intuitive measure, we normalise the stresses by subtracting the average of each component within each grain/fragment to present stress heterogeneity relative to the unknown average stress state within each area (see Methods).

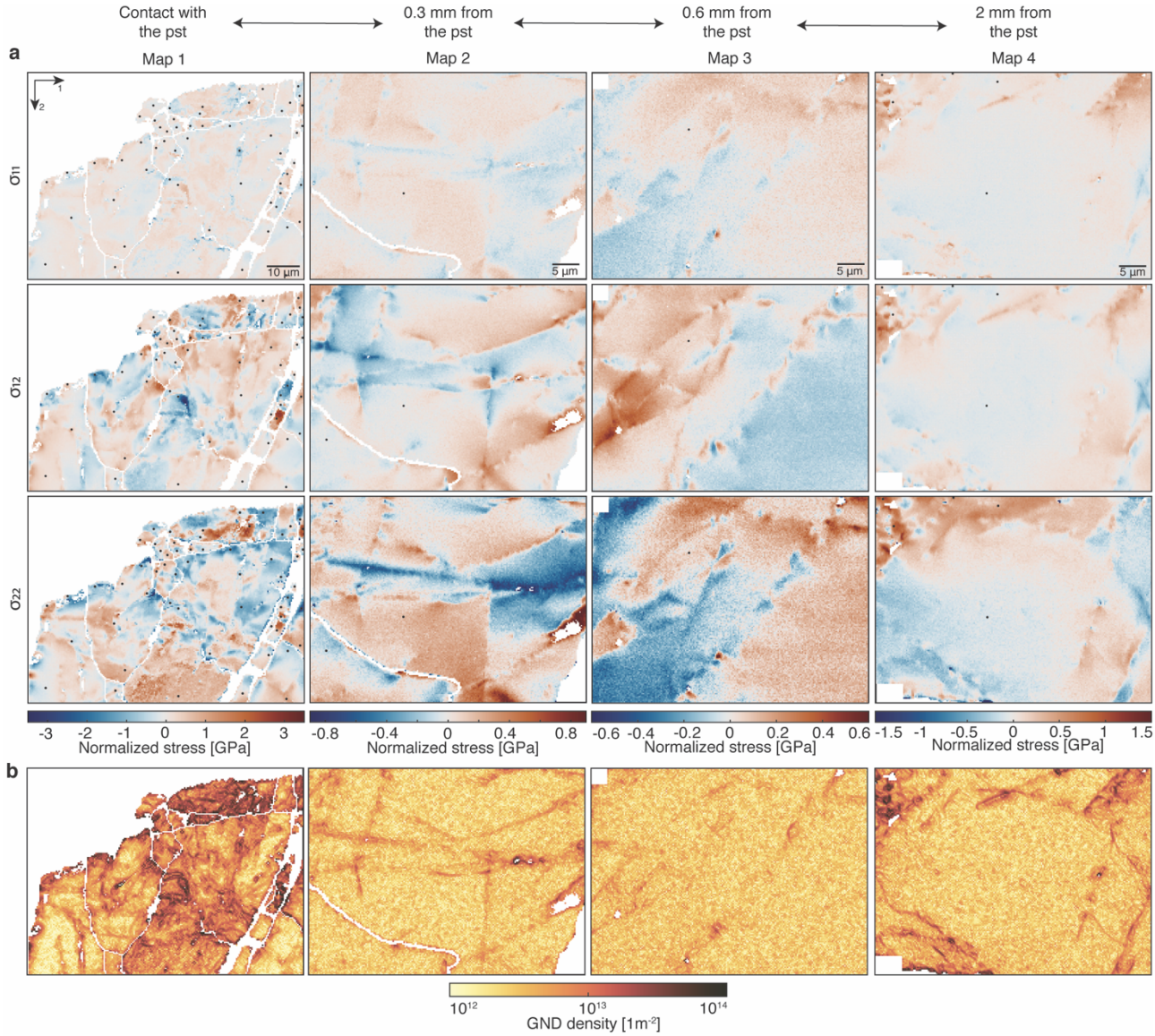

Fig. 3 | Residual stress heterogeneities and GND densities at increasing distance from the pseudotachylyte fault vein. **a**, In-plane components of the residual stress. Stress is normalized to the mean stress for each grain (see Methods). White areas are not-indexed pixels or pixels that do not meet the quality criteria (see Methods). Black dots mark the selected reference points. **b**, GND densities obtained from the measured lattice rotations.

In Maps 1–3 the heterogeneity in intragranular in-plane residual stress increases from a few hundreds of megapascals (Map 3) to more than 5–6 GPa (Map 1, σ_{12} and σ_{22}) approaching the pseudotachylyte. Maps 2 and 3 show abrupt variations and change in sign of residual stress across straight bands. In Map 1, stress heterogeneity occurs over smaller length scales and is more irregularly distributed in space. Map 4, located farther away (approximately 2 mm) from the pseudotachylyte than Map 3, exhibits greater stress values than in both Maps 2 and 3, and smoother stress changes without sharp straight boundaries of abrupt stress variation. Therefore, Map 4 does not fit with the gradient of

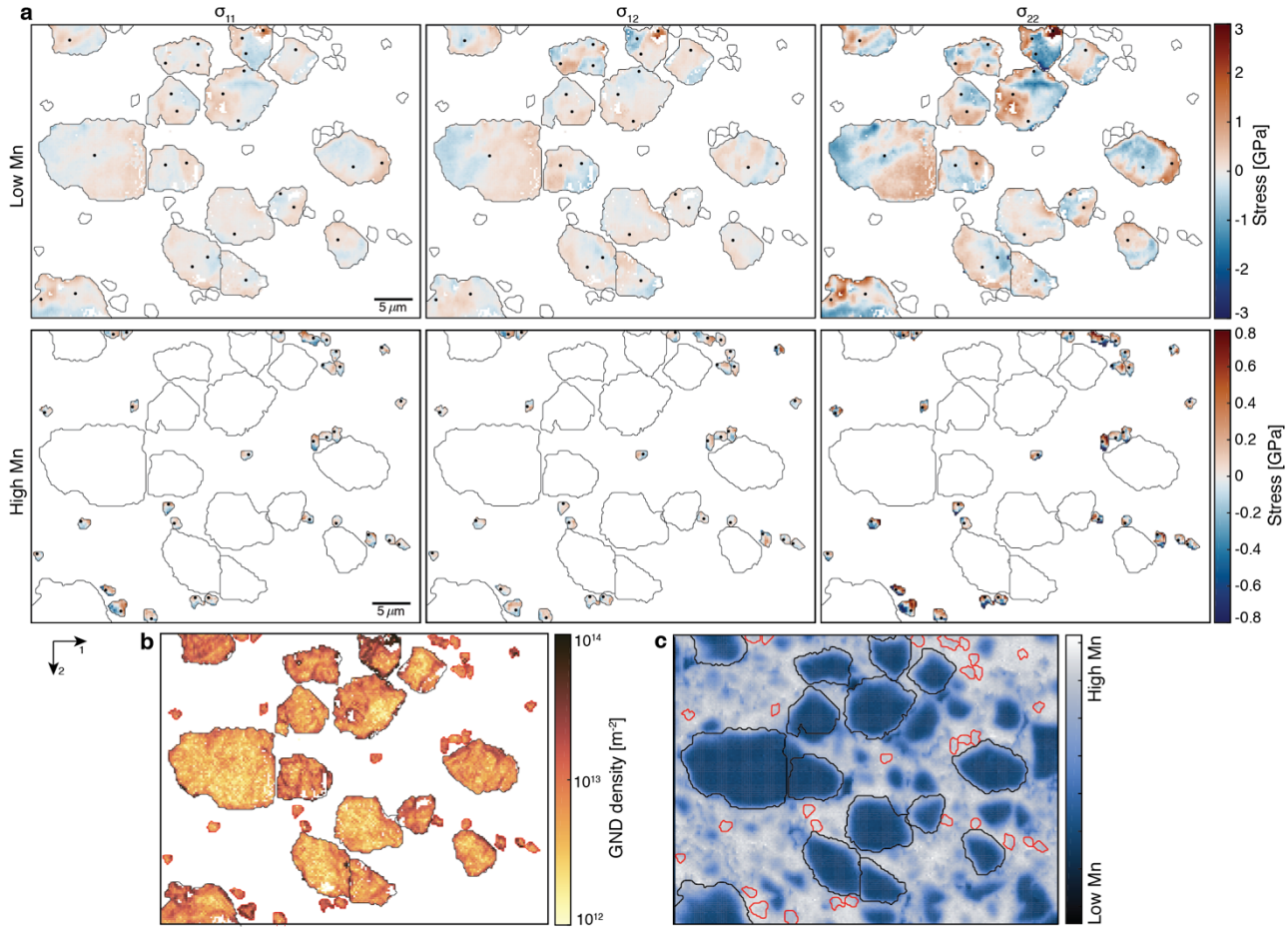

Fig. 4 | Residual stress heterogeneities and GND densities in the cataclastic domain. **a**, In-plane components of the residual stress. Stress is normalized to the mean stress for each grain (see Methods). White areas are not-indexed pixels or pixels that do not meet the quality criteria (see Methods). Black dots mark the selected reference points. Results are divided between low-manganese and high-manganese garnets (see c). Only selected grains were analysed due to the heterogeneous quality of the EBSD patterns. **b**, GND densities obtained from the measured lattice rotations. **b**, Chemical map of manganese. Black and red lines mark the boundaries of the low-manganese and high-manganese garnets, respectively.

progressive decrease of residual stress observed from Map 1 to Map 3. The same spatial gradient observed for the residual stresses is reflected in the GND densities, with the highest values measured close to the pseudotachylyte (Map 1), locally up to 3×10^{14} m^{-2}. With increasing distance, the GND densities decrease to $< 10^{13}$ m^{-2} with only local higher values. High GND densities are typically located along the straight boundaries at which the sign of stress switches and, in general, correspond to the areas in the maps where the highest residual stresses are recorded

Map 5 (Fig. 4) images a band of cataclastic garnet directly in contact with the pseudotachylyte. The clasts are overgrown by garnet enriched in Mn, with euhedral shapes in the finest micrometric clasts. The larger clasts (5–15 μm in diameter) record stress heterogeneity in the range 2–4 GPa (σ_{12} and

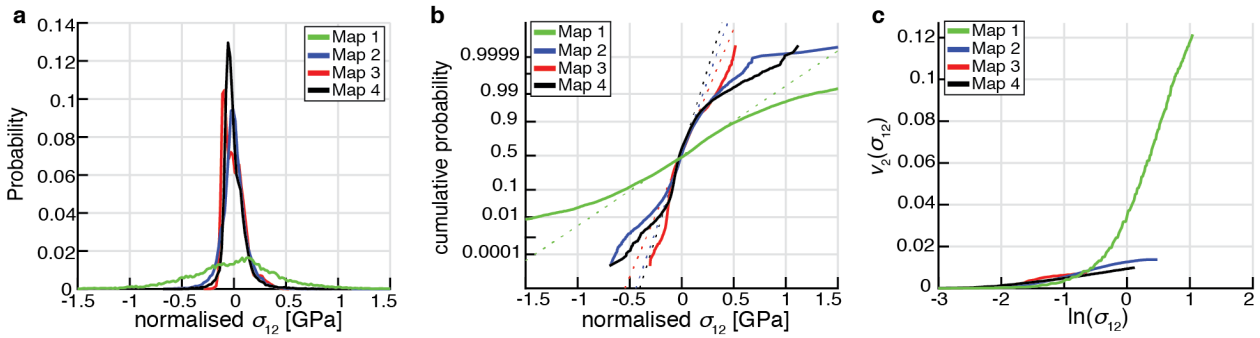

Fig. 5 | Probability distribution and distribution form analysis of the stress heterogeneities in Maps 1–4. a, Probability distribution of normalized σ_{12} for the four maps, calculated with a bin width of 20 MPa. **b**, Normal probability plot of normalized σ_{12} for the four maps. Normal distributions correspond to straight lines (represented as dotted lines). **c**, Restricted second moments of the normalized σ_{12} for the four maps. Straight lines represent probability following $P(\sigma) \propto |\sigma^{-3}|$.

σ_{22}), comparable to values measured in Map 1. In contrast, the smaller, Mn-enriched garnet clasts are less distorted and exhibit stress heterogeneities of up to 1–1.5 GPa. However, measurements in small grains must be considered with caution as measurement points could be influenced by topographic effects due to sample preparation. The GND densities, similar to the residual stress heterogeneities, are comparable to those measured in Map 1.

Figure 5 presents probability distributions of the normalized σ_{12} in-plane stress component and characterises the shape of the high-stress tails of the distributions (also App. 2 Fig. 4). The stress distributions are broadest in Map 1, where the highest residual stresses heterogeneity is measured. Normal probability plots, in which the cumulative-probability axis is scaled such that a normal distribution is represented by a straight line, are useful to visualise the shape of the high-stress tails of the distributions (Fig. 5b). The central, low-stress portion of each distribution follows a straight line whereas the high-stress tails deviates from the linear trend indicating that they do not follow the same normal distribution. The deviation is most accentuated in Map 1. The shapes of the tails are characterized by plots of the restricted second moments (υ_2) of the stress distributions versus $\ln(\sigma)$ (Fig. 5c; App. 2 Fig. 4; see Methods for details). At high stresses the distributions follow straight lines, meaning that $P(\sigma_{12}) \propto |\sigma_{12}^{-3}|$, with Map 1 having a steeper slope extending to higher stresses. The inverse cubic form is expected if the stress field is determined by the presence of dislocations,

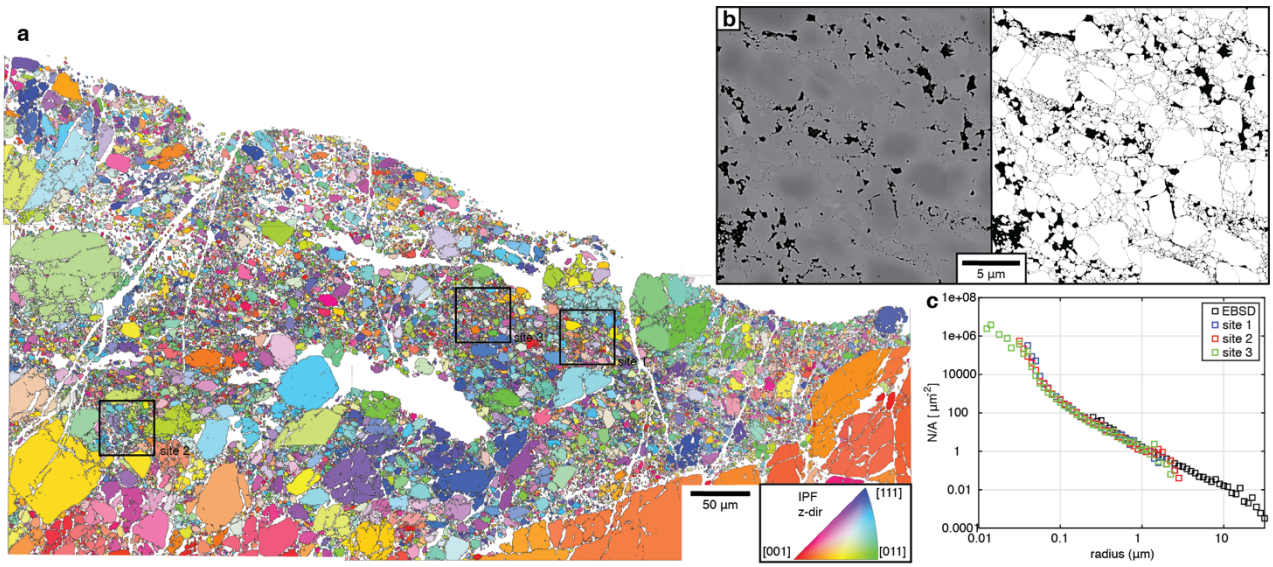

Fig. 6 | Grain-size analysis for the cataclastic domain. a, Mosaic of four EBSD maps color-coded by the mean orientation of every grain according to the inset inverse pole figure. **b**, High-resolution BSE image of a fine-grained portion (site 3 marked in the EBSD map) and segmented garnet grains (white). **c**, Area-weighted (cumulative number of grains divided by the total area of the fragments, N/A) clast-size distributions determined from EBSD data and the three high-resolution BSE-images plotted in a log–log space;

and the gradient of the curve is proportional to the total dislocation density (Groma et al., 1998). We also subset each map based on the corresponding GND densities at each pixel and computed the restricted second moments of the stress distributions for each subset (App. 2 Fig. 5). Subsets with greater GND densities exhibit steeper slopes of the straight portions of the curves and in general extend to higher stresses. Only Map 3 shows similar curves for all the subsets.

4.2 Clast size distribution

The clast size distribution was measured in the cataclastic domain where Map 5 was acquired. Large EBSD maps (Fig. 6a), covering most of the domain, allow clasts down to size of 0.22 µm to be well-indexed and measured. The remaining non-indexed portions in the EBSD maps (~ 30 %) correspond to phyllosilicates, holes and the finest-grained garnet clasts. High-resolution BSE images were used to measure the clast size distribution of these finer-grained (down to 20 nm in equivalent radius) portions (Fig. 6b, App. 2 Fig. 6). The clast-size distributions plotted in a log-log diagram can be fitted with polylines with slopes (D) in the range -1.9–-2.3, for most of the grain sizes, except for the

smallest grains ($D \geq -1$ for grain sizes $\lesssim 0.1$ μm) (Fig. 6c). The clast-size distribution normalised by the total area covered by each fragment class (Fig. 6c) shows a good match between the clast-size distributions determined independently by EBSD and high-resolution BSE imaging over the range of overlapping equivalent radii.

5. DISCUSSION

5.1 Lattice damage by dynamic rupture propagation

The HR-EBSD maps reveal high GND densities and high magnitudes of stress heterogeneity stored in the lattice of garnet crystals damaged during an earthquake. The zone of high stress and high GND density extends only a few millimetres in thickness from the pseudotachylyte boundary. Heterogeneity in residual stresses of as much as 5–6 GPa at the contact with pseudotachylyte decrease to a few hundred megapascals over a distance of less than 1 mm. Such an extreme and localized gradient of GND density and residual stress heterogeneity well match the dynamic stress field surrounding the tip of an earthquake rupture propagating at a velocity close to the Rayleigh velocity (Reches and Dewers, 2005).

Elastic straining of the garnet lattice took place associated with pulverization. Extreme comminution occurred mainly at the contact with the pseudotachylyte, where the greatest residual stresses are stored, but also along auxiliary planes. Pulverization is common in the damage zone of upper crustal faults (Doan and Gary, 2009; Mitchell et al., 2011) but has been also described from high-pressure natural and experimental pseudotachylytes. Austrheim et al. (2017) interpreted pulverized garnets within a few millimetres distance from a pseudotachylyte to be the result of fault slip due to changes in stress between compression and extension. Coseismic pulverization in the process zone was described in garnets and pyroxenes from lower-crustal rocks (Mancktelow et al., 2022; Campbell and Menegon, 2022), and in olivine, clinopyroxene and plagioclase in ophiolites exhumed from an intermediate-depth subduction environment (Pennacchioni et al., 2020). Pulverization was also reproduced experimentally at high pressure conditions (Incel et al., 2019), and interpreted as the result of a high stress pulse during fracture propagation. Therefore, we infer that garnet comminution and

fracturing and the associated high GND densities and residual stresses were produced during the propagation of the earthquake rupture tip. This interpretation is reinforced by the fact that fracturing predates melting along the fault plane since pulverized material is crosscut by pseudotachylyte injection veins and included as clasts in the pseudotachylyte (as also interpreted by Mancktelow et al., 2022). The abrupt variations in magnitude and sign of stress across sharp bands without offset are also features consistent with pulverisation, since the sharp bands are likely healed or incipient cracks. This interpretation is consistent with features in Map 5, where the later high-Mn garnets record lower GND densities than the original low-Mn garnet clasts in the same structural position.

The residual stresses and GND distributions in the garnet likely resulted from the dynamic stress field around the tip of a mode II fracture propagating close to the Rayleigh-wave velocity. Following Freund (1990), the stress field can be calculated as

$$\sigma_{ij} = \left(\frac{K_{II}}{\sqrt{2\pi r}}\right) * \sum_{ij}^{II}(\theta, v), \qquad (17)$$

and its magnitude is controlled by the stress intensity factor K_{II}, the fracture-propagation velocity v, the distance from the tip, r, and the angle θ (see Methods). Assuming typical material properties for middle-crustal rocks and a fracture energy of 10^6 J/m^2, in the range of values proposed for earthquake ruptures (Cocco et al., 2023), calculations show that the short-lived (a few microseconds), high-stress pulse can exceed 10 GPa and stresses significantly drop over a few millimetres distance from the slipping plane (App. 2 Fig. 7). The distance of host-rock domains from the original earthquake rupture plane cannot be precisely established, since the process zone associated with the earthquake rupture propagation was reworked by frictional wearing and melting during seismic slip. However, the measured domains of Maps 1–3 within the host-rock garnet still preserve a GND-density gradient compatible in shape with the stress field predicted nearby the rupture plane and with the sharp spatial gradient normal to the fracture. Map 4 does not strictly follow the gradient recorded by Map 1–3. This deviation may reflect local variations of the propagating rupture stress field, effects of secondary fractures or interactions between different grains.

5.2 Preservation of GNDs and residual stress

The restricted second moment of the probability distributions of stress shows that at higher stresses the distributions have the form $P(\sigma_{ij}) \propto |\sigma_{ij}^{-3}|$. This distribution indicates that the residual stress heterogeneity results from the stress fields around dislocations (Groma et al., 1998; Wallis et al., 2021). High dislocation densities were described from olivine and quartz that have been experimentally deformed at coseismic conditions and not subsequently annealed (Druiventak et al., 2011; Trepmann et al., 2013). High dislocation densities were also observed in quartz in host rock flanking upper-crustal pseudotachylytes and were interpreted to result from high coseismic stress (Bestmann et al., 2012; Trepmann et al., 2017). Within quartz, dislocations are recovered during the high thermal pulse in contact with the pseudotachylyte (Bestmann et al., 2012). In contrast, the increase in GND density and residual stress towards (and up to the contact with) the pseudotachylyte is preserved within the garnet analysed here, which we interpret to be due to the more sluggish mobility of dislocations in garnet than in quartz at the ambient deformation conditions (Phillips et al., 2021). The seismically-induced dislocation arrays in shattered quartz described by Bestmann et al. (2012) were completely erased by annealing during the thermal transient associated with frictional heating and melting (see their figure 6). However, it is of note that this dislocation array is preserved about a hundred μm away from the pseudotachylyte despite seismic faulting occurring at ambient conditions close to the low-temperature limit of crystal plasticity in quartz. These observations suggest that earthquake-induced dislocations can be preserved after formation through the exhumation path to Earth's surface even at temperatures close to the onset of crystal plasticity. This is even more valid for garnet that typically deforms by crystal plasticity at higher temperature than quartz, and well above the ambient condition of the pseudotachylyte formation studied here (Voegelé et al., 1998, Phillips et al., 2021).

The lack of recovery of GNDs in the studied sample is responsible for the measured residual stresses. The absence of any other deformation, metamorphism and interaction with fluids after the earthquake

allowed preservation of the crystal lattice distortions produced during the earthquake-rupture propagation.

5.3 Energy budget of an earthquake

The energy stored in the lattice of the host-rock garnets, in terms of GND densities and associated residual elastic strains, corresponds to the energy necessary for dislocation generation (Andersen, 2017). Thus, the energy density can be used to quantify the damage imparted to the rock during the propagation of the earthquake rupture at the studied patch of seismic fault. The total energy density stored in the lattice (E_{cp}) can be calculated as the sum of the energy density stored as elastic strain (E_{st}) and the energy density stored as dislocation cores (E_{disl}), which are computed as

$$E_{\mathrm{st}} = 1/2 * (\sigma_{11}\varepsilon_{11} + \sigma_{22}\varepsilon_{22} + 2\sigma_{12}\varepsilon_{12}) \quad (18)$$

and

$$E_{\mathrm{disl}} = \rho_{\mathrm{GND}} * (G * b^2)/(2\pi), \qquad (19)$$

with G the isotropic shear modulus (100 GPa), b the length of the Burgers vector (1 nm: Meagher, 1980) and ρ_{GND} the density of GNDs measured with HR-EBSD at every pixel of the map. The energy estimates are shown in Fig. 7. Average values of each map are considered as the mean energy densities at the specific distance from the pseudotachylyte (6.8×10^6, 2.6×10^5, 1.6×10^5 and 9.2×10^4 J/m^3 at 0, 0.3, 0.6 and 2 mm of distance from the pseudotachylyte respectively; 15×10^6 J/m^3 in the large clasts of the cataclastic portion).

To convert E_{cp} (J/m^3) into W_{CP} (J/m^2) we computed the interpolating function of the energy densities collected in the same garnet for the Maps 1–3, and then integrated it across the investigated garnet over a distance of approximately 1.2 mm. W_{CP} estimated from the host-rock garnet varies between 1.5×10^3 and 2.4×10^3 J/m^2 depending on weather a linear or power-law interpolation is considered, respectively. However, consistent with the observations of Pittarello et al. (2008), the breakdown work recorded in the host rock adjacent to the pseudotachylyte is likely a minor component of the real work density, since most of the highly strained and comminuted material was extensively consumed during the frictional melting. We therefore calculate the bulk energy by extrapolating the

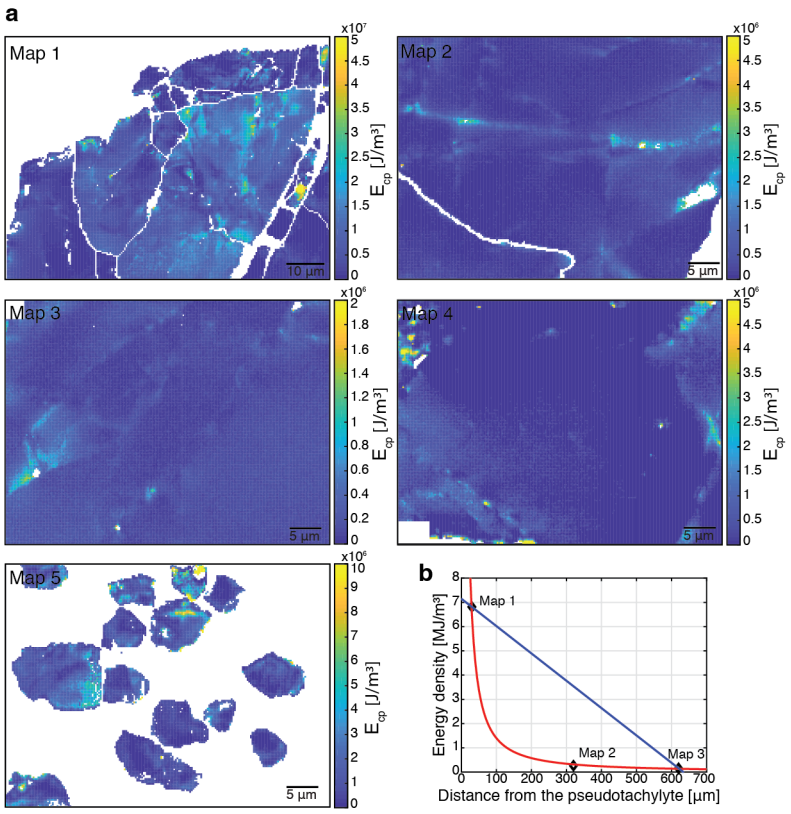

Fig. 7 | Energy densities stored as dislocations and their strain fields. a, Maps of energy density stored in the lattice of the garnet, calculated from HR-EBSD data shown in Fig. 3 and 4. **b**, Mean energy density as a function of distance from the pseudotachylyte margin for Maps 1–3. Red and blue curves show the power-law and linear interpolation curves.

maximum estimated value of E_{cp} (in Map 1) over the total thickness of the pseudotachylyte with the awareness that this estimate still provides an underestimate of the actual energy. Under this assumption, and also assuming that the pseudotachylyte thickness is representative for the studied seismic fault, we estimate 2×10^4 J/m^2 as bulk W_{CP} value. A further complication is related to the intrinsic uncertainties of the HR-EBSD measurements (see methods).

W_{FS} is calculated from the clast size distributions measured in the cataclastic domain. As for the calculation of W_{CP}, the clast-size distribution measured in contact with the pseudotachylyte has been considered representative of the material consumed by frictional melting within the pseudotachylyte and therefore extrapolated over the whole pseudotachylyte thickness. We use a value of $D = 2.1$ that best approximates the slope of the clast-size distribution in the semi-logarithmic plot over most of the measured dimensional range (0.02 – 20 µm clast equivalent radii). The estimated values of W_{FS} for this fractal number and grain-size range vary between 1.3×10^4 and 2.9×10^5 J/m^2 (Methods). These

values fall on the low side of other measurements reported for natural faults in the literature (1×10^4 – 1×10^7 J/m^2: Johnson et al., 2021; Chester et al., 2005; Mei et al., 2006; Pittarello et al., 2008). Our upper value of W_{FS} is similar to the estimate of Pittarello et al. (2008), who also considered a single-jerk, pseudotachylyte-bearing, upper-crustal fault within tonalite in their study and used the same approach of extrapolating the locally-measured clasts-size distribution of host-rock plagioclase over the whole pseudotachylyte thickness.

Frictional heat was calculated considering the energy consumed in rock heating, melting and further heating of the melt (Di Toro et al., 2005) (Methods). We assumed a maximum temperature of the melt of 1450 °C, based on the observation that plagioclase preferentially melted whereas quartz persisted as clasts of disaggregated fragments. For a 3-mm thick pseudotachylyte fault vein made of plagioclase, biotite and garnet and with ~ 20% of clasts, the energy dissipated by frictional heating W_{FH} is approximately 13×10^6 J /m^2, on the same order of magnitude as that estimated by Pittarello et al. (2008) for their pseudotachylyte-bearing fault.

In summary, W_{FH} is two orders of magnitude greater than W_{FS} and three orders of magnitude greater than W_{CP}.

6. CONCLUSIONS

The high dynamic stresses at the tip of a propagating earthquake rupture induce, together with host-rock fracturing and cataclasis, intense elastic deformation and GNDs in the lattice of host-rock minerals. These latter microstructures can escape annealing along the exhumation path to Earth's surface. We have quantified the energy component associated with the coseismic crystal-plastic damage produced by the earthquake rupture and have estimated the other components of breakdown work spent on the fault during an earthquake from an exhumed pseudotachylyte-bearing mid-crustal fault providing a complete on-fault energy budget. The estimates establish a clear hierarchy in the energy-density partitioning of breakdown work. Heat accounts for the largest part of the energy consumed on fault, as it is two and three orders of magnitude greater than the fracture energy and the

crystal-plastic energy, respectively. The local accumulation of crystal-plastic energy densities in the lattice of faulted minerals, here exceptionally preserved in the host-rock garnet, may eventually play a role in post seismic physical-chemical processes on the fault plane, e.g., by hampering post seismic creep due to local strain hardening or by promoting metamorphic re-equilibration providing energy expendable to overstep reactions.

Chapter 3: How to quake a subducting dry slab at intermediate depths: inferences from numerical modelling

Toffol, G.[1], Yang, J.[1], Pennacchioni, G.[1], Faccenda, M.[1], Scambelluri, M.[2]
[1] University of Padova, Department of Geosciences, Padova, Italy
[2] University of Genova, Department of Earth, Environment and Life Sciences, Genova, Italy

This chapter, in a slightly different version, is published in the journal Earth and Planetary Science Letters (Toffol et al., 2022)
Authorship contribution statement:
GT: Conceptualization, Investigation, Visualization, Interpretation, Writing – original draft, Writing – review & editing. **JY**: Software, Supervision, Writing – review & editing. **GP**: Conceptualization, Supervision, Writing – review & editing **MF**: Supervision, Writing – review & editing **MS**: Conceptualization, Writing – review & editing

Abstract

The origin of intermediate-depth subduction seismicity is a topic of research since long time. While plate unbending is considered as one of the main stress loading mechanisms, the processes responsible for earthquake nucleation are still unclear and depend on the question of whether failure occurs in the wet dehydrating portion of the slab or in the predominantly dry portion. Recently, the seismogenic portions of subducting oceanic slabs has been proposed to consist of dominantly dry metaperidotite that deforms by seismic brittle failure in absence of fluid-mediated embrittlement.

In this work, we quantify by numerical modelling the differential stress achievable during unbending of a subducting slab. We show that the presence of discrete hydrated domains in a dry, strong slab amplifies the differential stress to high seismogenic values (ca. 3-4 GPa in the 100-200 km depth range) at intermediate depths. We also consider the effects of low temperature plasticity in olivine that can hinder the build-up of high differential stress to the first 100 km of depth.

1. INTRODUCTION

Subduction margins record most of the earthquakes occurring on Earth. However, the origin of intermediate-depth seismicity, approximately between 60 and 300 km of depth, is still controversial (Frohlich, 2006; Zhan, 2020). Intermediate-depth hypocentres typically cluster along two distinct layers at the slab interface (upper plane of seismicity: UPS) and 20-40 km within the slab (lower plane of seismicity: LPS), showing downdip compressional and extensional focal mechanisms, respectively (Brudzinski et al., 2007). Seismicity decreases exponentially with depth in most cases, and the two layers merge between 150 and 300 km of depth depending on the slab temperature (Wei et al., 2017; Florez and Prieto, 2019). This seismicity is consistent with unbending of the rigid portion of the slab (Engdahl and Scholz, 1977). Despite there is a general agreement that slab unbending could be one of the main stress-loading processes in the subducting lithosphere, the mechanisms responsible for seismic failure are still debated. The conundrum is whether earthquakes occur in presence of fluids (a dehydrating slab) or in a dominantly dry lithosphere.

In presence of fluids released by breakdown of hydrous minerals, the build-up of fluid pressure may lead to brittle failure at relatively low differential stresses even at relatively high confining pressure (the dehydration embrittlement triggering mechanism: Raleigh and Paterson, 1965; Yamasaki and Seno, 2003). The pressure and temperature conditions of dehydration estimated from experiments and thermo-mechanical modelling roughly correspond to the locations of intermediate-depth earthquake hypocentres (Brudzinski et al., 2007; Abers et al., 2013; Hasegawa and Nakagima, 2017; Ferrand, 2019). This correspondence has been brought as evidence for the occurrence of dehydration embrittlement, despite antigorite dehydration has been shown to be related with low-slip events rather than unstable faulting and earthquake nucleation (Chernack and Hirth, 2011). The occurrence of veining in the exhumed blueschist-eclogite facies ophiolites (i.e. exhumed remnants of subducted oceanic lithosphere) was also presented as a possible geological record of dehydration embrittlement (Angiboust et al., 2012), although direct evidence of an effective link of seismicity with veining is ambiguous or missing. Anyway, the effectiveness of this process for the whole range of intermediate-

depth earthquakes is still debated since it implicitly would involve extensive hydration and serpentinization of the subducting slab.

Antithetic to dehydration embrittlement, the seismic brittle failure of predominantly dry and strong oceanic lithosphere has been proposed. In this case, very high differential stress is required at high confining pressure for brittle failure (~6 GPa at 100 km of depth under compression; ~3 GPa considering a semi-brittle behaviour, i.e. the Goetze criterion). Recent observations of exhumed ophiolites bring support to this theory.

The only recognised geological record for ancient intermediate-depth seismicity is represented by rare pseudotachylytes (quenched frictional melts, widely accepted as a marker for earthquakes) in blueschist-eclogite facies ophiolites (Zambia: John and Schenk, 2006; Alpine Corsica: Andersen and Austrheim, 2006; Fabbri et al., 2018; and Moncuni-Lanzo Massif (western Alps): Scambelluri et al., 2017, Pennacchioni et al., 2020). These occurrences suggest that subduction earthquakes can nucleate in an essentially dry and strong mantle peridotite with only minor serpentinized portions. In particular, the glassy pseudotachylytes preserved in Moncuni (Pennacchioni et al., 2020) testify for water-absent conditions during and after seismic failure at subduction depths of ca. 70 km. The absence of mylonites coeval with the pseudotachylytes excludes a thermal runaway process (Kelemen and Hirth, 2007). In the dry slab model, the base of the seismic lithosphere is marked by the brittle-ductile transition of olivine at 700-800 °C (Ueda et al., 2020; Pennacchioni et al., 2020). This temperature is consistent with the seismic cut-off estimated for subducting slabs at intermediate depths (Yamasaki and Seno, 2003; Hacker et al., 2003), as well as for locked subducted remnants (Ferrand and Manea, 2021).

Moncuni pseudotachylyte-bearing dry ophiolites do not represent the fossilized record of a circum-Pacific-like setting, where most of intermediate-depth earthquakes occurs. Nonetheless these field evidences provide a viable proxy for the rheological behaviour of a dry mantle slab during intermediate-depth subduction seismicity. If this model is accepted, it implies brittle failure at extremely high differential stress. This interpretation is supported by the huge volumes of

pseudotachylytes at Moncuni and Corsica, as also reported for earthquakes in the dry lower continental crust (Menant et al., 2018; Menegon et al., 2017). A similar conclusion of earthquakes generated by brittle failure in a dry and strong peridotitic slab arises from the interpretation of seismic data of various double planes of seismicity of subduction systems (Florez and Prieto, 2019).

With this work we investigate, by numerical modelling, the effective capacity of a subducting slab of building up the high differential stress required for brittle failure at intermediate-depth conditions in absence of fluid-mediated embrittlement processes. We test (i) a homogeneous, dry slab of peridotite, and (ii) a dry peridotite slab with scattered weak domains of serpentinite, representative of limited local hydration. We also test the effect of low-temperature plasticity of olivine, as main mineral component of peridotite, on the stress build-up.

2. METHODS

2.1. Numerical approach

Pseudo-2D numerical simulations were performed with the thermomechanical code LaMEM (Lithosphere and Mantle Evolution Model) (Kaus et al., 2016). The code, based on the finite differences and marker-in-cell method, solves the conservation equations of mass, momentum and energy:

$$\frac{\partial v_i}{\partial x_i} = 0 \tag{1}$$

$$\frac{\partial \tau_{ij}}{\partial x_j} - \frac{\partial P}{\partial x_i} + \rho g_i = 0 \tag{2}$$

$$\rho C_p \left(\frac{\partial T}{\partial t} + v_i \frac{\partial T}{\partial x_i}\right) - \frac{\partial}{\partial x_i}\left(k \frac{\partial T}{\partial x_i}\right) - H = 0 \tag{3}$$

where v_i are the components of velocity, x_i the spatial coordinates, η is the viscosity, P the pressure, ρ the density, g the gravitational acceleration, C_p the heat capacity, T the temperature, k the thermal conductivity and H the heating term. This latter term includes shear heating ($H_S = \tau_{ij} \times (\dot{\varepsilon}_{ij} - \dot{\varepsilon}_{ij}^{el})$) and adiabatic heating ($H_a = T\alpha\rho g v_z$), with τ_{ij} the deviatoric stress tensor and $\dot{\varepsilon}_{ij}^{el}$ the elastic strain rate tensor.

The density ρ is computed considering the thermal expansion (α) and the compressibility (β) according to the following equation: $\rho = \rho_0 [1 + \beta(P - P_0)] \times [1 - \alpha(T - T_0)]$ with ρ_0 the density at the reference pressure (P_0) and temperature (T_0).

The model considers Maxwell materials with a visco-elasto-plastic rheology. The total deviatoric strain rate is expressed as:

$$\dot{\varepsilon}_{ij} = \dot{\varepsilon}_{ij}^{viscous} + \dot{\varepsilon}_{ij}^{elastic} + \dot{\varepsilon}_{ij}^{plastic} = \frac{1}{2\eta_{eff}}\tau_{ij} + \frac{1}{2G}\frac{D\tau_{ij}}{Dt} + \dot{\lambda}\frac{\partial Q}{\partial \sigma_{ij}} \quad (4)$$

where on the left there is the total deviatoric strain rate and on the right the respective viscous, elastic and plastic deviatoric strain rate components. η_{eff} is the effective viscosity, G elastic shear modulus, t time, $\dot{\lambda}$ plastic multiplier, Q plastic flow potential, and $\sigma_{ij} = -P + \tau_{ij}$ the total stress. $\dot{\varepsilon}_{ij(plastic)} = 0$ if $\tau_{II} < \tau_{yield}$.

The viscous behavior is given by a combination of flow laws of dislocation creep (power law creep), diffusion creep (linear creep) and, when considered, Peierls creep (exponential creep). These relations are expressed in terms of effective creep viscosity as (Kaus et al., 2016; Popov et al., 2008):

$$\eta_{eff} = \frac{\tau_{II}}{2\dot{\varepsilon}_{II}^{viscous}} \quad (5)$$

$$\dot{\varepsilon}_{II}^{viscous} = \dot{\varepsilon}_{disl} + \dot{\varepsilon}_{diff} + \dot{\varepsilon}_{pei} = A_{disl}{\tau_{II}}^{n} + A_{diff}\tau_{II} + A_{pei}(\frac{\tau_{II}}{\gamma\tau_p})^{s} \quad (6)$$

$$A_{disl} = B_{disl}\exp(-\frac{E_n + PV_n}{RT}) \quad (7)$$

$$A_{diff} = B_{diff}\exp(-\frac{E_d + PV_d}{RT}) \quad (8)$$

$$A_{pei} = B_{pei}\exp(-\frac{E_p + PV_p}{RT}(1 - \gamma)^2) \quad (9)$$

$$s = 2\gamma(1 - \gamma)\frac{E_p + PV_p}{RT} \quad (10)$$

with $B_{disl,diff,pei}$ prefactors, $E_{n,d,p}$ activation energies, $V_{n,d,p}$ activation volumes, γ a constant and τ_p the Peierls stress. The dependence on pressure of τ_p is expressed as $\tau_p = \tau_p^0(1 + {G'}/{G} * P)$ (with G and G' values of shear modulus and its pressure derivative, 78.4 GPa and 1.7 respectively, as in Kawazoe et al., (2009)). Strain hardening is computed as $\tau_p = \tau_p(1 + A(\varepsilon_{pei} - \varepsilon_{pei1})/(\varepsilon_{pei2} - \varepsilon_{pei1}))$, with

A the hardening factor, ε_{pei} the accumulated Peierls strain ($\int \dot{\varepsilon}_{pei} dt$), ε_{pei1} and ε_{pei2} the minimum and maximum Peierls strains. A was set to 0.23, allowing for a maximum strain hardening of ~2 GPa in accordance with values estimated by *Hansen et al., 2019*. ε_{pei2} was set to 0.1. If $\varepsilon_{pei} > \varepsilon_{pei2}$ the strain hardening is the maximum, $\tau_p = \tau_p * (1 + A)$.

The creep viscosity of materials is calculated as the harmonic mean:

$\eta_{creep} = \eta_{min} + (\frac{1}{\eta_{disl}} + \frac{1}{\eta_{diff}} + \frac{1}{\eta_{Peierls}} + \frac{1}{\eta_{max}})^{-1}$, with η_{max} $(= 10^{24}\ Pa\ s)$ and η_{min} $(= 10^{18}\ Pa\ s)$ respectively the upper and lower viscosity cut-offs.

The visco-elastic viscosity is given by:

$\eta_{ve} = \eta_{min} + (\frac{1}{\eta_{el}} + \frac{1}{\eta_{disl}} + \frac{1}{\eta_{diff}} + \frac{1}{\eta_{Peierls}} + \frac{1}{\eta_{max}})^{-1}$, where η_{el} is the viscosity representative of the elastic behavior for a Maxwell body. η_{el} depends upon the Maxwell relaxation time and the computational timestep, and it is expressed as $G\Delta t$ if $\Delta t \ll \Delta t_{Maxwell} = {\eta_{vp}}/{G}$.

The plastic failure is described by the Drucker-Prager criterion $\tau_{yield} = C\cos\theta + P\sin\theta$, where C is the cohesion and θ the internal friction angle. Plastic viscosity is given by $\eta_{pl} = \frac{\tau_{II}}{2\dot{\varepsilon}_{II}}$ when the second invariant of the deviatoric stress exceeds the yield stress.

The visco-elasto-plastic viscosity is $\eta_{vep} = \min(\eta_{ve}, \eta_{pl})$.

2.2. Large-scale subduction model setup

The model domain is 2600 km × 2 km × 670 km in x_1-x_2-x_3 directions, resolved with a discrete grid of 961 × 3 × 627 nodes. We refine a region of 500 km × 560 km around the subduction zone obtaining a higher resolution of 1 km × 1 km to capture stress localization during slab bending and unbending (Faccenda et al., 2009). The mechanical boundary conditions are free slip for all boundaries. To mimic free surface in finite difference method, we use a 10-km-thick low viscosity 'sticky-air' ($10^{18}\ Pa\ s$) with a free surface stabilization algorithm (Kaus et al., 2010).

The modelled subducting plate is 100 km thick and 1550 km long. The upper 7 km represents the crust (we employ a wet quartz rheology to ensure lubrication at the plate top boundary) and the rest

Phase	ρ_0 (kg/m^3)	C_p (J/kg/K)	k (W/m/K)	α (1/K)	β (1/Pa)	Viscous flow law	G (Pa)	C (Pa)	θ (°)
Sticky air	1	1 x 10^6	1000	3 x 10^{-5}	-	1 x 10^{18} Pa·s	-	-	-
Weak zone	3200	1200	3	3 x 10^{-5}	1 x 10^{-11}	1 x 10^{19} Pa·s	10 x 10^{10}	-	-
Oceanic crust	3200	1200	3	3 x 10^{-5}	1 x 10^{-11}	Wet quartzite (disl)	5 x 10^{10}	1 x 10^6	1
Oceanic mantle	3300	1200	3	2.7 x 10^{-5}	1 x 10^{-11}	Dry olivine (disl + diff (+ pei))	10 x 10^{10}	2 x 10^7	30
Asthenosphere	3300	1200	3	3 x 10^{-5}	1 x 10^{-11}	Dry olivine (disl + diff (+ pei))	10 x 10^{10}	2 x 10^7	20

Table 1: List of parameters of the large-scale subduction models.

Flow laws	$B_{(n,d,p)}$ (Pa^n/s)	$E_{(n,d,p)}$ (J/mol)	$V_{(n,d,p)}$ (m^3/mol)	n	d (μm)	p	Tensor correction	γ	τ_{pei} (Pa)
Wet quartzite (disl)[1]	3.2 x 10^{-4}	154 x 10^3	0	2.3	-	-	Uniaxial	-	-
Dry Olivine (disl)[2]	1.1 x 10^5	530 x 10^3	1.5 x 10^{-5}	3.5	-	-	Simple shear	-	-
Dry olivine (diff)[2]	1.5 x 10^9	375 x 10^3	5 x 10^{-6}	1	1000	3	Simple shear	-	-
Olivine (pei)[3]	5.7 x 10^{11}	540 x 10^3	0	-	-	-	-	0.1	8.5 x 10^9

Table 2: Parameters of the flow laws implemented in the model (after 1: Ranalli, 1995; 2: Hirth and Kohlstedt, 2003; 3: Kameyama et al., 1999). Prefactors $B_{n,d}$ for dislocation and diffusion creep are corrected in the code for the experimental conditions (tensor correction as in *Gerya, 2019*) and comprise the effect of grain size.

is the oceanic mantle (dry olivine rheology). In front of the plate a 40 km × 40 km square of weak material with low viscosity (the weak zone of App. 3 Fig. 1) eases plate subduction.

The thermal profile of the plate is given by the half space cooling with the thermal age ranging from 100 My to 10 My. We use a mantle potential temperature of 1275 °C and a mantle adiabatic gradient of 0.4 °C/km.

The subduction is driven by the density contrast of the oceanic plate and surrounding mantle. In order to slightly enhance the density contrast and to obtain a self-sustained subduction, different thermal expansion coefficients are used for the plate and the surrounding mantle (2.7×10^{-5} and 3×10^{-5} $°C^{-1}$, respectively).

Circular inclusions (radius = 2 km) are scattered in the upper 40 km of the plate and make up 5% to 20% of the volume in the various simulations. A simulation with two sets of weak layers (thickness of 2 km, inclined at 60° to the surface and spaced 11 km), resembling a set of mutually crosscutting faults (Faccenda et al., 2009) was also performed. Inclusions are present in the plate since the beginning of the simulation but with the same properties of the surrounding material. Inclusions are activated by changing elasticity and viscosity parameters (i) once the slab reaches the 660 km depth and flattens on the lower boundary, or (ii) before the slab flattens, with the tip close to the 660 km of depth (i.e. hanging slab). Solutions are then saved after 10 timesteps. Some models were run for more than 10 timesteps to catch the maximum deviatoric stress around the inclusions. See *Table 1 and 2* for the complete list of rock properties and parameters and figure B.1 for a schematic representation of the initial setup.

2.3 Small-scale benchmark model: stress field around a single circular inclusion

A series of simplified simulations were performed to investigate the effect of a weak circular inclusion in a stronger matrix to test the code. The models have (i) 100 km × 50 km size, (ii) 1 km to 0.01 km grid resolution, and (iii) a central circular inclusion of 2 km radius. For sake of simplicity, visco-elastic materials with constant viscosities are considered. All the simulations were run under a constant strain rate of 10^{-14} s^{-1} (compression in the horizontal direction), unless otherwise specified.

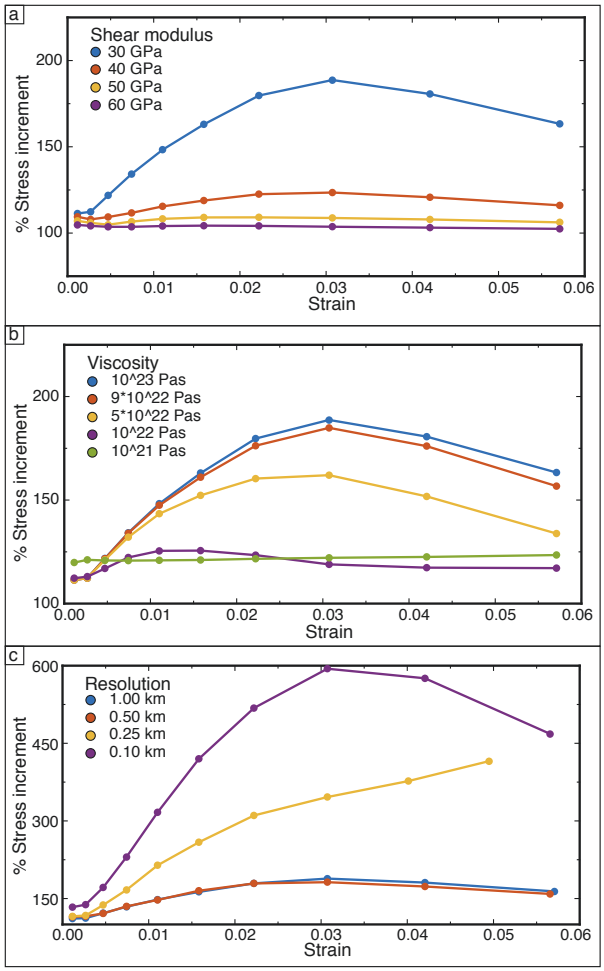

Fig. 1 | Small-scale benchmark models: stress amplification, defined as the maximum deviatoric stress around the inclusion divided by the far field stress in the matrix ($max(\tau_{II})/\tau_0$), as a function of strain. Simulations were run for 30 timesteps; stress values are plotted every three timesteps. **a,** Effect of shear modulus contrast. Matrix has η = 10^{23} Pas and *G* = 100 GPa; the inclusion has same viscosity as the matrix and variable *G*. Model resolution: 1 km. **b,** Effect of the viscosity contrast. Matrix has η =10^{23} Pas and *G* = 100 GPa; the inclusion has *G* = 30 GPa and variable viscosity. Model resolution: 1km. **c,** Effect of resolution. Matrix has η = 10^{23} Pas and *G* = 100 GPa; the inclusion has the same viscosity as the matrix and *G* = 30 GPa. The model resolution ranges from 1 km to 0.1 km.

The tests are performed at conditions analogous to that encountered in the cold portion of the slab during subduction simulations: (i) strong material with viscosity 10^{23} Pas and shear modulus 100 GPa, and (ii) weak inclusion with viscosity ranging from 10^{23} to 10^{18} Pas and shear modulus in the range from 100 GPa to 20 GPa. The simplified model results confirm that in a viscoelastic material the amplification of the outer stress field (defined here as second invariant of the deviatoric stress normalized to far field stress: τ_{II}/τ_0) around a circular inhomogeneity (i) increases with increasing

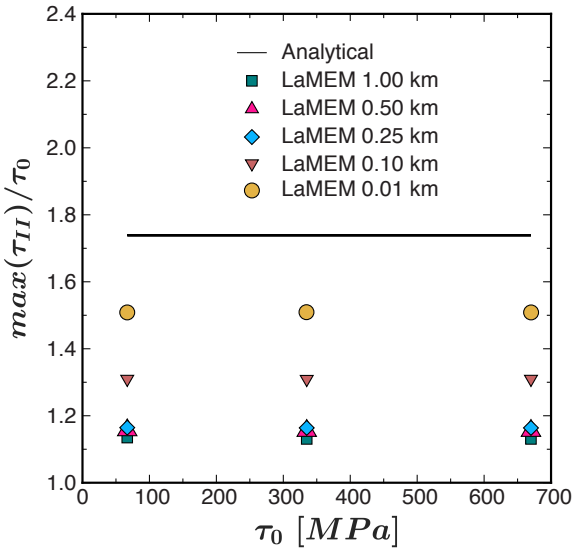

Fig. 2 | Analytical vs. numerical benchmark. Values of the maximum second invariant of deviatoric stress of the first timestep normalized to the far field stress ($max(\tau_{II})/\tau_0$). The three small-scale models (matrix with η = 10^{23} Pas and *G* = 100 GPa, inclusion with η = 10^{23} Pas and *G* = 30 GPa, resolution from 1 km to 0.01 km) are run at different strain rates (10^{-14}, $5*10^{-14}$ and 10^{-13} s^{-1}) corresponding to different far-field stresses. The black line represents the maximum stress amplification predicted by the analytical solution.

shear modulus contrast, and (ii) decreases with increasing viscosity contrast (at a given contrast in shear modulus) (Fig 1 a, b).

A set of simulations is used to test the effect of grid resolution on the magnitude of stress amplification. Results show that stress amplification is strongly resolution-dependent (Fig 1 c). The maximum values of τ_{II}/τ_0, obtained from the first timesteps of the simplified numerical simulations are compared with the value predicted by the analytical solution (see App. 3) with same shear moduli and aspect ratio of the inclusion. Varying the resolution of the numerical simulations from 1 km (resolution of the subduction models) to 0.01 km, the τ_{II}/τ_0 values progressively increase still remaining below the analytical prediction (Fig 2; Fig B.2). The numerical results also do not change by considering different far field stresses (obtained using strain rates of 10^{-14}, $5*10^{-14}$ and 10^{-13} 1/s). This is in agreement with theoretical predictions since stress amplification does not depend upon stress magnitude. These observations indicate that the stress perturbations around the inclusions obtained from our numerical simulations are reliable and can be considered as lower limits for the effective stress amplification.

3. RESULTS

The numerical models simulate self-sustained free subduction of an oceanic slab of dry peridotite into a homogeneous mantle. In the simulations, the slab negative buoyancy relative to the underlying mantle is the driving force of subduction. During subduction the slab bends at the trench, unbends at intermediate depths and leans against the lower mantle boundary, represented by the lower boundary of the model domain, at 660 km of depth. Subduction is faster in its initial stage due to high density contrast between the asthenosphere and the cold slab tip and it slows down once the slab reached the lower boundary of the model and starts to flatten. Fast subduction, combined with the initial thermal profile of the slab (colder towards the tip), allows for the preservation of a colder core at depth. This is evidenced by the 600 °C isotherm on the left side in Fig. 3. This thermal behaviour doesn't affect the reliability of our simulations.

In the bending region, the deviatoric stress in the rigid portion of the slab describes two paired arcs, with the outer one under extension and the inner one under compression. The stress fields, and associated under- and overpressure arcs, are reversed during slab unbending at ca. 60 km of depth (Fig. 3). Deviatoric stress is higher in the outer arc than in the inner arc, regardless of being in extension or compression, due to a general increase of stress at the crust-mantle interface. The rigid slab layer, that includes the two stressed arcs, is ca. 40 km thick and is confined at the base by the 800 °C isotherm. At the intermediate-depth conditions of our simulations, this isotherm roughly marks the transition to crystal-plastic behaviour of olivine (App. 3 Fig. 3).

Two main sets of numerical experiments were performed, with the viscous behaviour described by flow laws including (i) diffusion and dislocation creep and (ii) diffusion, dislocation and Peierls creep (low-temperature plasticity, LTP). The two configurations represent end-member behaviours for the rigid plate under subduction: (i) without a stress cut-off determined by LTP and (ii) with low-temperature plasticity controlling the deformation of the plate. These two viscous behaviours, presented in the sections 3.1 and 3.2, determine dramatic differences in the obtained stresses. Tested parameters and results of all the simulations are summarized in *Table 3*.

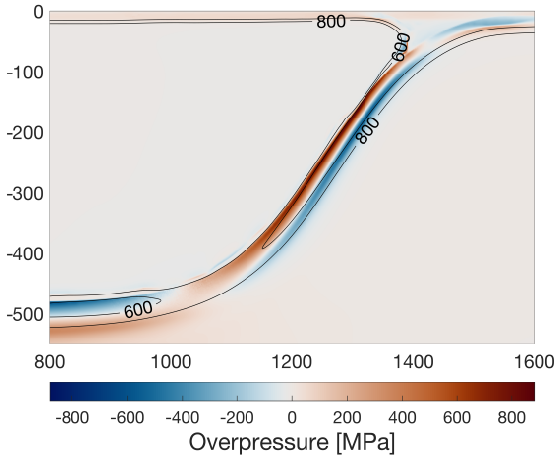

Fig. 3 | Overpressure (total pressure minus lithostatic pressure) distribution in the subducting slab (homogeneous case, viscous rheology defined by diffusion and dislocation creep; *model 14*). At intermediate depths, strong positive and negative overpressures affect the upper 40 km of the slab, i.e. the colder and stronger portion. Isotherms of 600 °C and 800 °C are reported. Distances are in km.

3.1 Models without LTP

In absence of stress cut-off, in a homogenous dry slab, the deviatoric stress reaches a maximum of ca. 1 GPa in the unbending region once the subducting slab leans on the boundary at 660 km depth (Fig. 4a; model 14). For a hanging slab the deviatoric stress is higher, ca. 1.6 GPa (model 1). Given the transient higher velocities (~ 100 cm/y) in the hanging slab, we consider the first case, with subduction velocity ca. 10 cm/y, as more representative of common conditions for subducting slabs (e.g., Lallemand et al., 2008).

The presence of weak circular inclusions, simulating isolated serpentinized domains of peridotite, induces a several-folds amplification of the stress field observable in both the outer compressional arc and in the inner extensional arc. The magnitude of the local stress amplification solely depends on the contrast in material properties since we considered circular inclusions (so without further amplification due to geometrical effects (App. 3 Fig. 4)).

The highest deviatoric stresses, 3.5 – 4.5 GPa, are observed in the unbending region when the shear modulus of inclusions is markedly reduced (70% lower than in the pristine peridotite, in the model 30 GPa and 100 GPa, respectively) at constant viscosity (Fig. 4b-e; models 15-18). Amplification would be even larger with higher (but unrealistic) contrast in shear modulus (model 19). Smaller

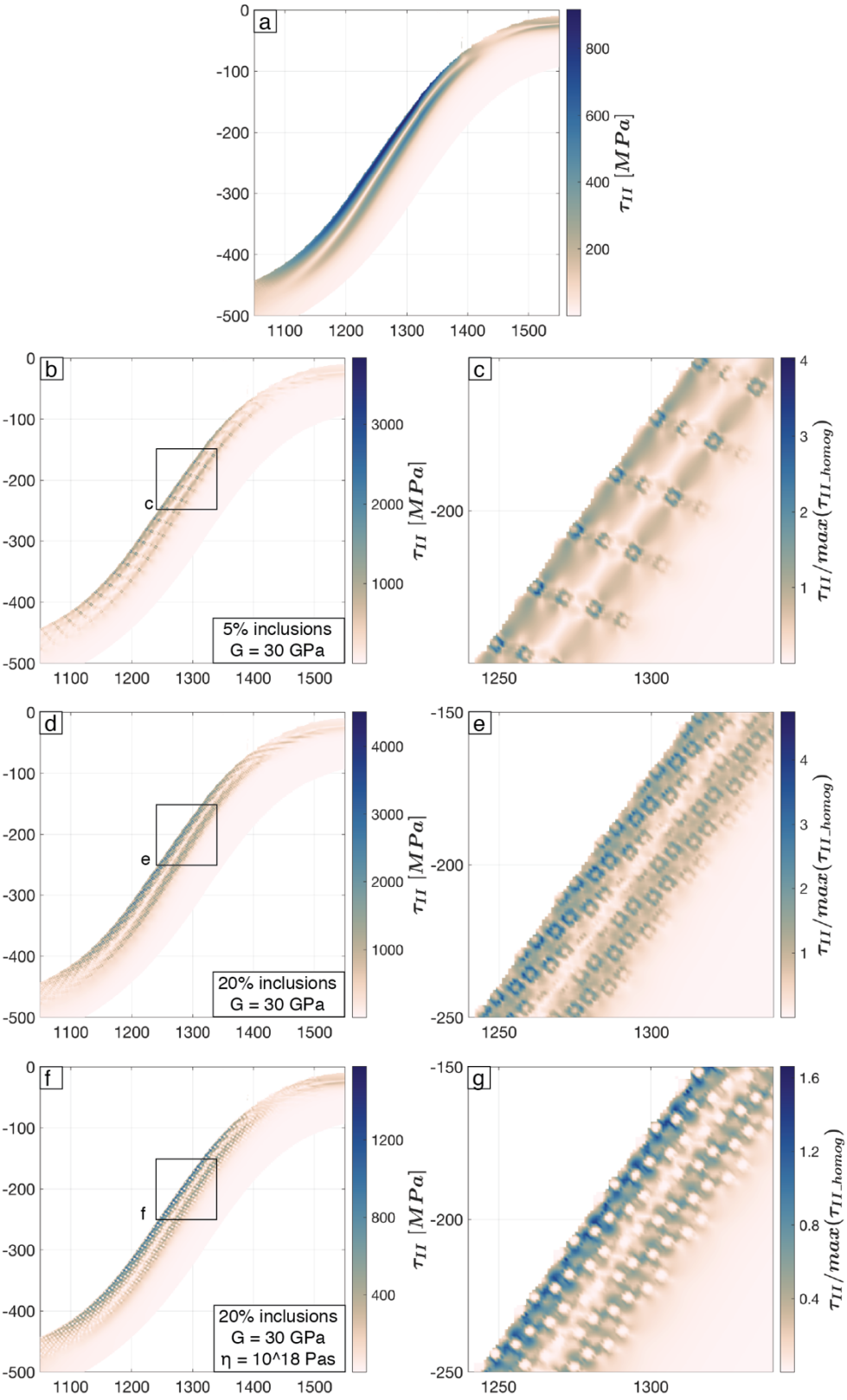

Fig. 4 | Magnitude of the deviatoric stress (τ_{II}) in the subducting plate for models without LTP. **a,** Homogeneous slab (*model 14*). **b,** 5% of weak (G = 30 GPa) inclusions (*model 15*). **d,** 20% of weak (G = 30 GPa) inclusions (*model 18*). f) 20% of weak (G = 30 GPa and μ = 10^{18} Pas) inclusions. **c, e, g,** details of b, d, f with stress normalized to the maximum value of the homogeneous case ($\tau_{II}/max(\tau_{II\_homog})$). Distances are in km.

contrasts in shear modulus, or a decrease in inclusions viscosity, results in smaller stress amplification. An increase in the spatial density of inclusions (from 5% to 20% of the first 40 km of the slab) leads to a general increase in the stress amplification. This effect is caused only by the reciprocal position of inclusions, whose outer stress fields locally interact.

The values of relative stress amplification are 200-250% and 400-480%, respectively, in the case of a hanging slab and a flattened slab at the 660 km boundary. The discrepancy is due to differences in the computed timesteps (in the flattened configuration timesteps are roughly two to three times larger than with the faster hanging slab), causing variations in accumulated strain.

Some simulations were run longer than the reference 10 timesteps to test the effect of larger strains in the slab (models 31-33). The deviatoric stress increases with increasing strain. In these simulations stress reaches its upper boundary, the implemented yield criterion. The progressive increase of stress is determined by the build-up of elastic strain which is not dissipated until yielding. The yield criterion is reached faster when the shear modulus contrast is higher and is not reached if the contrast is too low (shear modulus of inclusions reduced by 20% with respect to the slab).

3.1.1 Faults

A simulation of a more realistic geometry of the distribution of the weak material was performed considering only diffusion and dislocation creep flow laws for simplicity (Fig B.5, models 34, 35). The conjugate pattern of weak (G = 30 GPa) tabular zones simulates faults produced at the trench during slab bending (Faccenda et al., 2009). With this configuration the stress amplification is of the same order of magnitude as for circular weak flaws. It is worth noting, however, that because of the limitations in the grid spacing, which results in overrepresentation of the thickness of the weakened faulted lithosphere, the models may not reproduce the highest stress values or a different behaviour due to the load-bearing weak material.

3.2 Models with LTP

LTP models were performed: (i) without accounting for pressure effects, following the widely used formulation of Kameyama et al. (1999); (ii) considering the pressure-dependence of the Peierls stress and the activation volume (Kawazoe et al., 2009); (iii) considering the effect of strain hardening in olivine (Hansen et al., 2019). In the simulations with LTP we obtain higher subduction velocities due to easiness of the slab to deform viscously and sink compared to the simulations not including LTP. In the simulations (ii) and (iii) the subduction is slower than in (i), but still faster than in simulations without LTP. This effect occurs because the slab viscosity slightly increases due to effects of pressure and hardening. Also, the Peierls creep was arbitrarily excluded above 1100 °C, giving raise to differences in the calculation of the effective viscosities.

The exponential creep, assumed to be active in the range of temperatures typical of a subducting slab, introduces a stress cut-off. This results in reduced deviatoric stresses with respect to the previous set of models: ca. 0.5 GPa in the homogeneous slab case (Fig. 5a; models 36, 42, 46, 50, 54) and 1 - 1.3 GPa in presence of weak (G = 30 GPa) circular inclusions after 10 timesteps (Fig. 5b-e; models 38, 44, 48, 52, 56), resulting in a relative stress increase of 200%, lower than the values obtained without LTP.

In presence of LTP, the effects of shear modulus contrast, viscosity contrast and spatial distribution of the inclusions described in section 3.1 are still valid. Contrary to the simulations without LTP, the progressive increase of stress with increasing strain is hampered. As result, the maximum achieved deviatoric stress is ca. 1.5 GPa (model 41) when considering the LTP formulation of Kameyama et al. (1999). The effect of pressure on the Peierls stress is small, leading to an increase of the maximum deviatoric stress around inclusions of ca. 200 MPa. The effect of the activation volume is more noticeable, especially at high pressure in the lower part of the unbending region, and results in a maximum differential stress of 3 GPa. Strain hardening also shows a positive impact on the stress build-up allowing for a maximum of ca. 2 GPa around inclusions. When both pressure effects and strain hardening are considered in the LTP formulation a maximum stress of ca. 3.8 GPa is achieved.

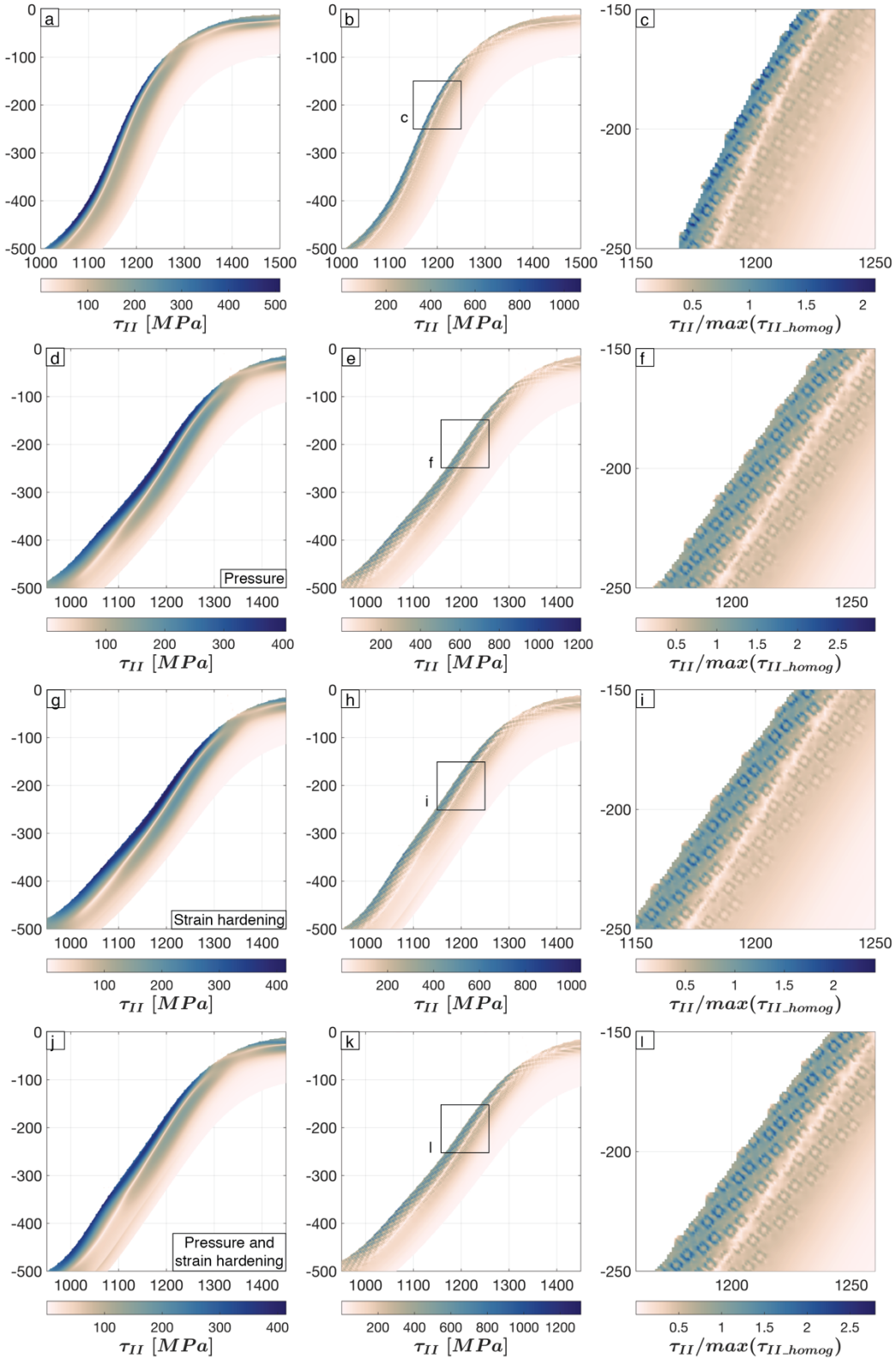

Fig. 5 | Magnitude of the deviatoric stress (τ_{II}) in the subducting plate for models with LTP. **a, d, g, j** homogeneous cases, with the standard LTP formulation, with pressure dependence, strain hardening, and both pressure and strain hardening, respectively. **b, e, h, k** 20% of weak (G = 30 GPa) inclusions. **c, f, i, l** Details of b, e, h, k, with stress normalized to the maximum value of the homogeneous case ($\tau_{II}/max(\tau_{II\_homog})$). Distances are in km.

4. DISCUSSION

Similar to previous studies (Faccenda et al., 2012), our numerical models of subduction reproduce two paired zones of overpressure and underpressure at the outer and inner arc of the unbending rigid slab layer, respectively. This stress distribution is compatible with the downdip contractional and extensional focal mechanisms of intermediate-depth earthquakes (Engdahl and Scholz, 1977).

In a homogeneous dry peridotitic slab, not considering LTP, the maximum differential stress during unbending (~ 1 GPa) is not high enough for Byerlee's brittle yielding below 40-50 km of depth (i.e. at the subduction depth of the eclogite-facies pseudotachylytes exhumed in the Lanzo Massif: Scambelluri et al., 2019; Pennacchioni et al., 2020). To expand the brittle field below this depth in the intermediate-depth seismic domain, in absence of fluid-assisted embrittlement, higher deviatoric stresses are required. These stresses are locally achievable in presence of weak heterogeneities under conditions of low-efficiency or absence of LTP. The nature of the weak heterogeneities, the interpretation of intermediate-depth seismicity in the light of our findings and the role of low-temperature plasticity of olivine in hindering stress build-up are discussed in the following sections.

4.1 Stress amplifiers in the slab

In a dominantly dry slab, weak flaws required for stress amplification may correspond to discrete domains of serpentinization. Serpentinite has a much lower shear modulus (<30 GPa) than peridotite (>80 GPa) (Abramson et al., 1997; Bezacier et al., 2010) and even partial serpentinization can significantly reduce the rock shear modulus (Jacobsen et al., 2006). Serpentinite has a much lower viscosity than peridotite (Hilairet et al., 2007), but partially serpentinized (meta)peridotite may retain a high viscosity, similar to that of peridotite, as indicated by the preservation of the pseudomorphosed, original magmatic fabric in the Moncuni peridotite body (Scambelluri et al., 2017).

Serpentinization of mantle peridotites may occur (i) in oceanic environments, (ii) along extensional faults during slab bending at the trench, and (iii) during subduction by occurrence of dehydration reactions in the crustal sections at the slab interface and subsequent interaction of fluids with originally dry peridotites (Faccenda, 2014; Ferrand, 2019). Serpentinization likely affects relatively

shallow portions of the slab within the upper plane of seismicity but fluids can locally redistribute to the underpressured lower plane of seismicity during unbending (Faccenda et al., 2012). Seismological data (Reynard et al., 2010; Kita and Ferrand, 2018; Florez and Prieto, 2019) suggest, however, that the LPS consist of essentially dry peridotites, confining the zones of deep hydration and serpentinization to discrete patches along percolation channels, rather than in continuous layers along faults (Ferrand et al., 2019). Moreover, a relevant fraction of chemically-bounded water in the mantle, once released during dehydration reactions, may leave the system by forced flow along high-porosity channels (Plumper et al., 2017), thus preserving the host peridotite and preventing more diffused weakening. From these considerations the representation of the weak serpentinized domains as spherical bodies (circles in the 2D view of our models) surrounded by dry peridotite may be an acceptable simplification. More complex shapes of isolated hydrated domains (e.g ellipsoids) would result in higher stress concentrations (Eshelby, 1957) (Figs. B.4, B.5)

Based on geophysical data, on the interpretation of the exhumed Lanzo ophiolites as a proxy for the inner portions of an oceanic slab, and on the results of our numerical models, we therefore envisage the seismogenic oceanic slab at intermediate subduction depths as a layer of dominant dry peridotite with scattered patches of meta-peridotite. These weak patches, likely aligned along healed faults, act as stress amplifiers in the surrounding pristine peridotite to GPa-level stresses necessary for brittle failure in absence of free fluids. In this view the base of the lower plane of seismicity can be interpreted as both the brittle/ductile transition for peridotite (Pennacchioni et al., 2020) and the bottom boundary of fragmentary fluid percolation/alteration inside the slab (Ferrand et al., 2017). This base was set at 40 km in our simulations based on the thickness of the stressed portion of the slab and in accordance with the thickness of double seismic zones within old oceanic lithosphere (e.g. Tonga double seismic zone (Wei et al., 2017)).

Our model results are quite consistent with the dehydration-driven stress transfer (DDST) proposed by Ferrand et al. (2017), based on laboratory-scale experiments and validated against seismological data (Kita and Ferrand, 2018). The experiments show that the negative volume change (not

implemented in our models) associated with dehydration of isolated serpentinite domains can even further enhance stress amplification in the load-supporting dry mantle peridotite of the slab. With respect to their model we share the same initial assumption of a predominantly dry and strong subducting plate with scattered domains of weak hydrated material, but here we demonstrate that seismogenic stresses are achievable independently of serpentine dehydration. The portion of slab where the highest stresses are observed in our simulations, at $T < 600$ °C, is compatible with the P-T conditions at which antigorite can still be stable as constrained from exhumed serpentinites (Gilio et al., 2019) and numerous petrological experiments and numerical simulations (for a review see Ferrand et al., 2019).

In agreement with the DDST model, our numerical results indicate, to a larger scale, that stress amplification is efficient for a relatively small volume of scattered, weak meta-peridotite domains. The DDST model predicts that the increase of serpentinization over a critical threshold turns into weakening of peridotite, with serpentinite forming an interconnected network of weak load-supporting layers and preventing the strong material to reach high stresses. In the simulation with fault-like weak material the overrepresentation of the weak phase imposed by the grid resolution leads to what could represent a load-supporting network. Nevertheless, even with that abundance of weak material, a marked amplification of stress in the strong domains is observed. This result could be an artifact due to insufficient grid resolution in the simulation. Another possible bias in our models is that viscosity of the weak material was kept equal to the viscosity of the surrounding peridotite, while it is probable that for large, laterally continuous serpentinite domains the viscosity would decrease as well. An extensive hydration, responsible for such a wide weakening, is not considered in our simulations, since it would result in major variations of the overall subduction behavior, whose investigation is beyond the scope of this paper. Hypothetically the strong blocks bounded by interconnected load-bearing serpentinite can still be seismic, reaching high deviatoric stress by jamming (Beall et al., 2019; Campbell et al., 2020). In the case of high degrees of hydration, that likely dominate close to the slab subduction interface, earthquakes may instead be triggered by dehydration/transformation-induced embrittlement.

4.2 Present day intermediate-depth seismicity

Positive correlations between the occurrence frequency of earthquakes and the presence of factors facilitating hydration of the plate have been reported for various subductions. Even if these observations are mainly interpreted in terms of dehydration-related events, they are also compatible with brittle failure under high differential stress since the amplification model proposed here requires a local hydration of the slab.

Assuming that intermediate-depth earthquakes are determined by the local stress amplification, they can be directly correlated with the number of weak inclusions capable of amplifying the stress in the dry strong peridotite: the higher the quantity of restricted-in-space weak inclusions, the higher the chance that stress locally reaches the yield criterion. Also, as observed in simulations with higher abundance of inclusions, if weaker and closely spaced inclusions are present (for example where multiple clusters of fault planes crosscut mutually) the chance of interaction increases resulting in a local further increase of deviatoric stress.

As discussed in section 4.1 weak inclusions are the product of localized hydration of the plate, so all the factors enhancing plate hydration should favour a high number of seismic events during subduction. Age of the plate, dipping angle, angle of convergence, and inherited structures are all elements that control plate hydration. For example, the variations in intermediate-depth seismicity observed for two adjacent segments of the Pacific plate subducting beneath the Alaska Peninsula have been related with different pre-subduction fabrics responsible of different amount of water entering the system (Shillington et al., 2015). The depth of outer rise faulting plays a major role in exerting a control on the hydration depth (Boneh et al., 2019). The thickness of the sedimentary cover has been shown to influence the rate of seismicity, since the thicker the crust the lesser the mantle hydration by outer rise faulting (Wagner et al., 2020). A similar dependency has been proposed also for the lower planes of seismicity of the Kuril and Japan subduction zones (Kita and Ferrand, 2018) and discussed in the light of the DDST theory. The minor frequency of lower-plane earthquakes with respect to the upper ones is compatible with our model, since deep plate hydration is more difficult and consequently stress amplification become less probable.

The reduction in frequency of events with increasing depths can be ascribed to the increasingly higher stresses required for brittle failure. The higher the yield stress the lower the probability to locally have a favourable configuration of inclusions (in terms of rheology, shape and spatial distribution) that could promote the seismic brittle failure.

4.3 Low-Temperature Plasticity

Low-temperature plasticity (LTP), also known as exponential creep or Peierls creep, is a deformation mechanism related to dislocation glide. The energy of activation depends on the stress required for motion of a dislocation along the crystal lattice, the Peierls stress. At low-T conditions, dislocations tend to pile up at lattice barriers since recovery processes are inefficient (e.g, dislocation climb). This results in strain hardening and eventually failure of the material. Strain hardening is a well-known process in material science and has been studied extensively for metals (Kocks and Mecking, 2003). Low-temperature plasticity is predicted at $T<0.3*T_{melt}$ (Evans and Goetze, 1979) that, for olivine, falls in the temperature range typical of subducting slabs at intermediate-depth conditions. The occurrence of LTP should prevent the slab from reaching extremely high differential stresses (Kameyama and Karato, 1999). Due to the exponential dependency upon stress, LTP represents a stress cut-off, in agreement with what observed in our simulations with pressure-independent LTP where the stress thresholds are (i) 500-600 MPa in a homogeneous slab, and (ii) ca. 1.5 GPa in presence of local stress amplifiers.

Several flow laws for LTP are reported in the literature, based on experimental deformation of olivine single crystals and polycrystals at various pressures and temperatures (Evans And Goetze, 1979; Kawazoe et al., 2009; Hansen et al., 2019; Fig. 6 and App. 3 for other references). However, the extrapolations of experimental results to natural conditions are not always concordant (Jain et al., 2017). The effect of pressure, in terms of activation volume and pressure-dependence of the Peierls stress, is not considered in many experiments due to its difficult quantification. This makes the extrapolated flow laws less predictive at depths of a few hundreds of km in subduction zones.

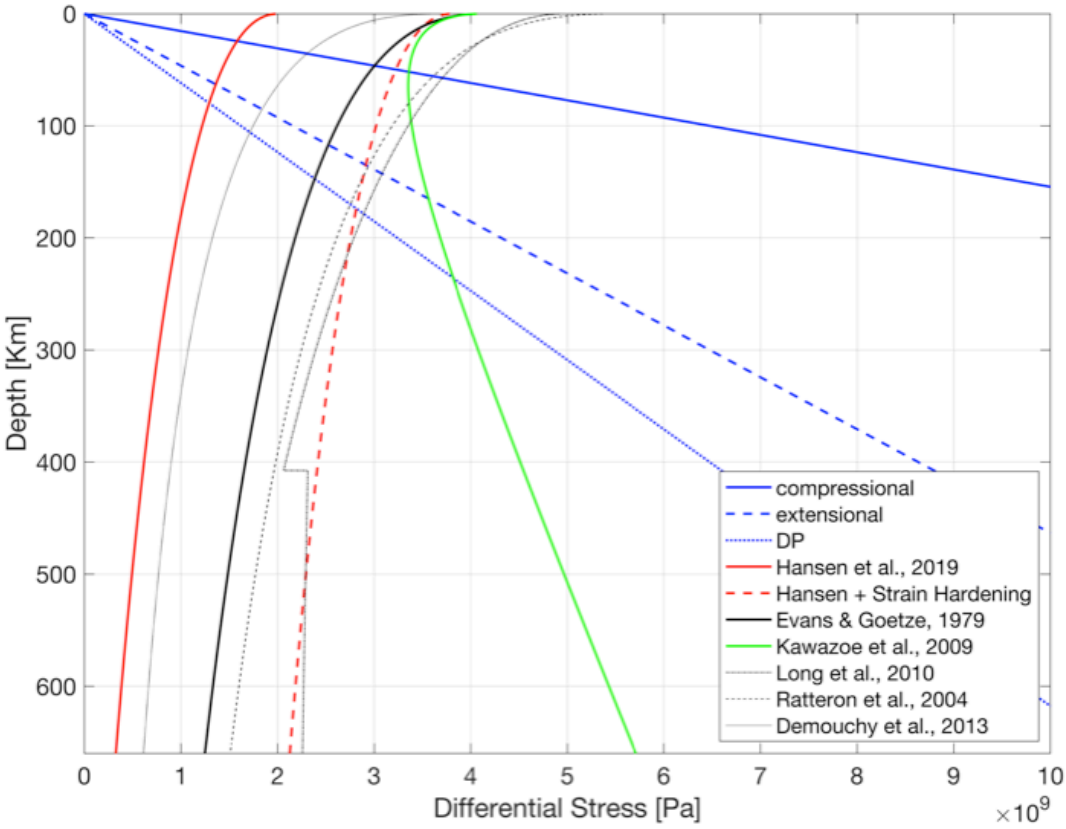

Fig. 6 | Deviatoric stress vs. depth profile for P, T conditions of a subducting slab (plate age 100 My, subduction velocity of 10 cm/s, strain rate of 10^{-14} s^{-1}, average density 3300 kg/m^3; thermal profile calculated following Frohlich, 2006, pages 41-42; see App. 3 Fig. 6 for pressure and temperature profiles). Blue curves: rupture criteria (compressional and extensional failure, Drucker-Prager criterion (DP) and Goetze criterion (GC)). Red, black and green curves: low temperature plasticity flow laws from the literature. See *App. 3* for input parameters.

The representation of a few flow laws for LTP (Fig. 6, App. 3) highlights the above-mentioned discrepancy. The stress curves presented in the figure are calculated for pressure and temperature conditions of an old and cold slab, compatible with conditions of Tonga (Wei et al., 2017) (App. 3 Fig. 6). For hotter slabs the stress values would be lower. In presence of LTP, the slab is prevented to reach brittle yielding below 80 – 100 km of depth, therefore excluding seismic brittle failure below this depth. LTP is dependent on temperature and strain rate, so old cold slabs should have a wider brittle field than young hot slabs. Nevertheless, temperature cannot be too low and strain rate too high at the slab-scale in a subduction zone and the brittle field should not extend deeply in excess of 100 km of depth. However, the strain rate can increase above the bulk slab-scale value in the stress-amplification sites around weak inclusions, which results in an extension of the brittle field to deeper levels in these highly stressed domains.

The pressure dependence of LTP, disregarded in many existing studies, is a factor that requires attention. Our simulations performed considering a pressure-dependent LTP flow law yielded higher stresses in the intermediate-depth region, due to a general strengthening with depth. The extrapolation of a pressure-dependent flow law to generic subduction conditions agrees with our observations and seems to allow brittle failure deeper than the other flow laws.

Recently a strain hardening behaviour has been proposed to occur during LTP of olivine (Hansen et al., 2019; Wallis et al., 2020). Authors suggest that strain hardening is determined by the back stress, i.e. the internal stress generated by dislocations pile-up. A relevant strain hardening, of ~2 GPa was estimated after 2% strain. In general, high strains are not common in the subducting homogeneous plate, but can be locally achieved around the weak inclusions in response to amplified stress. In the numerical models, despite the high stresses, we do not obtain very high strains (maximum values are ca. 0.7-0.8 and affect mainly the lower hotter part of the slab), but this is likely related to the grid resolution. In contrast, the boundary between rock domains with different mechanical properties is likely quite irregular in the oceanic lithosphere, which favours strain localization and stress amplification.

The occurrence of strain hardening during LTP of olivine can explain the extension of the brittle field below 100 km of depth in subduction zones. In this view the two sets of simulations performed here could represent end member behaviours. One end member involves strain hardening which ultimately results in the exclusion of LTP as an active deformation mechanism and leads to stress increase limited only by the occurrence of brittle failure. The second end member involves fully efficient LTP acting as stress cut-off mechanism and preventing build-up of extreme deviatoric stresses.

Without detailed studies of olivine behavior at intermediate-depth subduction conditions an exact quantification of the contribution of strain hardening is not possible. However, the pervasively damaged rocks surrounding pseudotachylytes reported in the Moncuni-Lanzo Massif (Scambelluri et al., 2018; Pennacchioni et al., 2020) may well represent the geological record of LTP eventually

evolved by strain hardening into brittle seismic failure, represented by the coeval eclogite-facies pseudotachylyte veins.

5. CONCLUSION

Numerical simulations show that a dry, strong, oceanic slab with scattered serpentinized (meta-peridotite) patches can reach differential stresses compatible with earthquake nucleation during intermediate-depth subduction. Meta-peridotites behave as local stress amplifier yielding differential stresses ≥4 GPa in the region of slab unbending. Stresses are high enough for triggering seismic brittle failure in the intermediate-depth subduction region, in accordance with recent field interpretations, experimental achievements and seismological data.

The stress amplification model requires the presence of partially serpentinized patches of material with deteriorated shear modulus but still high viscosity in the otherwise dry and strong peridotite. The extension of the model to the whole range of intermediate-depth earthquakes is limited by the occurrence of LTP in olivine. LTP would dramatically limit the amplification of stress around inclusions, preventing seismic brittle failure below 80-100 km of depth. However, the effectiveness of this deformation mechanism and its quantification, especially in terms of strain hardening and dependence upon pressure, is still a matter of ongoing study. We envisage that it could represent the key for the full comprehension of brittle failure under extremely high differential stress at high confining pressure.

CONCLUSIONS AND FUTURE DEVELOPMENTS

1. GENERAL CONCLUSIONS

In this thesis I studied the mechanics of the earthquake rupture at different ambient conditions and at different scales of investigation, from the micrometric to the lithospheric scale, by combining different techniques and approaches. The results and implication of this research project span from (i) the regional evolution of the Musgrave Ranges, one of the most famous localities hosting relatively-deep (middle- to lower-crustal) tectonic pseudotachylytes in the world, to (ii) the application of a cutting-edge analytical technique to geological seismically shocked materials with the goal of improving the knowledge of earthquake mechanics at the micrometric scale, to (iii) the extrapolation of the geological record of ancient seismicity to a realistic model of the predisposing conditions for earthquake failure at intermediate-depth conditions. But the implications of each chapter are broader and cover several subsidiary aspects of the wide fields of earthquake mechanics and lithosphere rheology.

The study of exhumed fault rocks bearing pseudotachylytes represents the core of the research project. From the direct observation and quantification of earthquake processes to the extrapolation of published data to a general field-constrained model of seismic failure, pseudotachylytes are here presented as the main source of information about the earthquake processes at depth. The three main chapters, although apparently only slightly linked with each other, represent three directions of the current research in the field of earthquake mechanics. The manifold implications of these studies, starting points for the development of future research, are here briefly reassumed.

i. In **Chapter 1**, I present new pressure estimates for the northern exposures of the Woodroffe Thrust based on the presence of stable andalusite and kyanite crystallizing together as microlites in the pseudotachylytes. The new pressure estimate, < 0.5 GPa, is in contrast with

previously published ones (0.8–1.1 GPa) and imply a steeper geometry of the thrust, with a dip angle of 20–25 ° instead of the previously proposed ~ 0.6 °. Apart from the important implications for the reconstruction of the tectonic setting of the region, this study rises the problem of assessing with high accuracy the ambient conditions of seismic faulting from pristine pseudotachylytes. High-resolution imaging and analytical techniques are shown to be fundamental to properly recognise the nanometric assemblages that crystallize during quenching and that can eventually be used to constrain the ambient conditions.

ii. In **Chapter 2**, I present the first complete estimate of the energy consumed on the fault plane during an earthquake from the study of a single-jerk pseudotachylyte produced at mid-crustal conditions. Together with the heat (~ 13 MJ/m^2) and the fracture energy (up to 0.29 MJ/m^2), I estimated the energy consumed during distortion of the crystal lattice of the host rock minerals (0.02 MJ/m^2) by measuring residual elastic strains and GNDs stored in seismically shocked garnets with HR-EBSD. The investigation by HR-EBSD of the coseismic crystal-plastic damage, here exceptionally preserved in the lattice of the garnets, paves the way for new approaches in the study of earthquake mechanics from exhumed pseudotachylytes.

iii. In **Chapter 3**, I propose a possible mechanism based on numerical simulations constrained from the occurrence of deep-seated pseudotachylytes in alpine ophiolites to explain brittle seismic failure at intermediate-depth conditions in dry and strong peridotites of the subducting oceanic slab with the presence of patchy serpentinized domains. The weak serpentinized domains, with degraded shear modulus but still relatively high viscosity, can induce a local amplification of the stress field determined by the unbending of the plate at depth. The amplified high differential stress can reach seismic values and it is only limited by the onset of low temperature plasticity in olivine, the main mineral constituting the slab. The role of low temperature plasticity in limiting the viability of this mechanism is discussed and the need

of more in depth experimental investigations of its behaviour under high confinement pressure is highlighted.

2. FUTURE DEVELOPMENTS

The results presented in this thesis are a reminder of the amount of information that can be extracted from pseudotachylytes-bearing rocks and how their investigation can expand our knowledge of the earthquake mechanics and in particular of the processes involved with seismic failure under high-grade conditions. As such, the new data, observations and interpretations proposed in the three chapters may have several follow ups arising from the main results. Thus, this thesis is proposed to be also of stimulus to further investigate the behaviour of geological materials under high stress, both in the brittle and in the ductile fields, as well as the preservation in time of the geological record of an earthquake and of the multifaceted spectra of information that can be extracted from it once it is exhumed to the surface.

Among the several open questions arising from the investigations performed in this thesis, the following may be of relevant interest:

i. The estimate of the energy consumed in the crystal-plastic straining of the garnet lattice (Chapter 2) represent a single and punctual observation of a process that took place along the whole fault and interested different minerals. Given the different fracture toughness, dislocation mobility, and available crystal-plastic mechanisms, it is reasonable to hypothesize that different minerals may react differently to the high stress earthquake rupture propagation. Thus, the application of HR-EBSD to different phases affected by the same seismic event and the combination of the observations may provide further insights into the mechanics of seismic rupture. Another interesting development would also be to investigate seismically shocked garnets from faults at different crustal levels to compare the role of crystal-plastic work in the energy budget of shallow and deep earthquakes. These studies may also be

integrated by TEM observation to properly characterize GNDs and learn more about the processes of energy density preservation in seismically shocked minerals.

ii. The efficiency of the mechanism of stress amplification around the weak serpentinized domains in the unbending subducting slab is principally governed by the onset of low temperature plasticity in olivine (Chapter 3). The flow laws implemented in the models may not be sufficiently accurate, especially at the high confinement pressure of the intermediate-depth region. Thus, better constrained flow laws, accounting for the effect of pressure and of strain hardening, could represent the key to obtain a complete comprehension of the brittle failure at those depths. In the light of the proposed model, it might also be relevant to perform micro- and nano-scale investigations on pseudotachylyte-bearing ophiolites with cutting-edge techniques like HR-EBSD to search for possible evidences of strain hardening processes predating the seismic failure.

Appendix 1

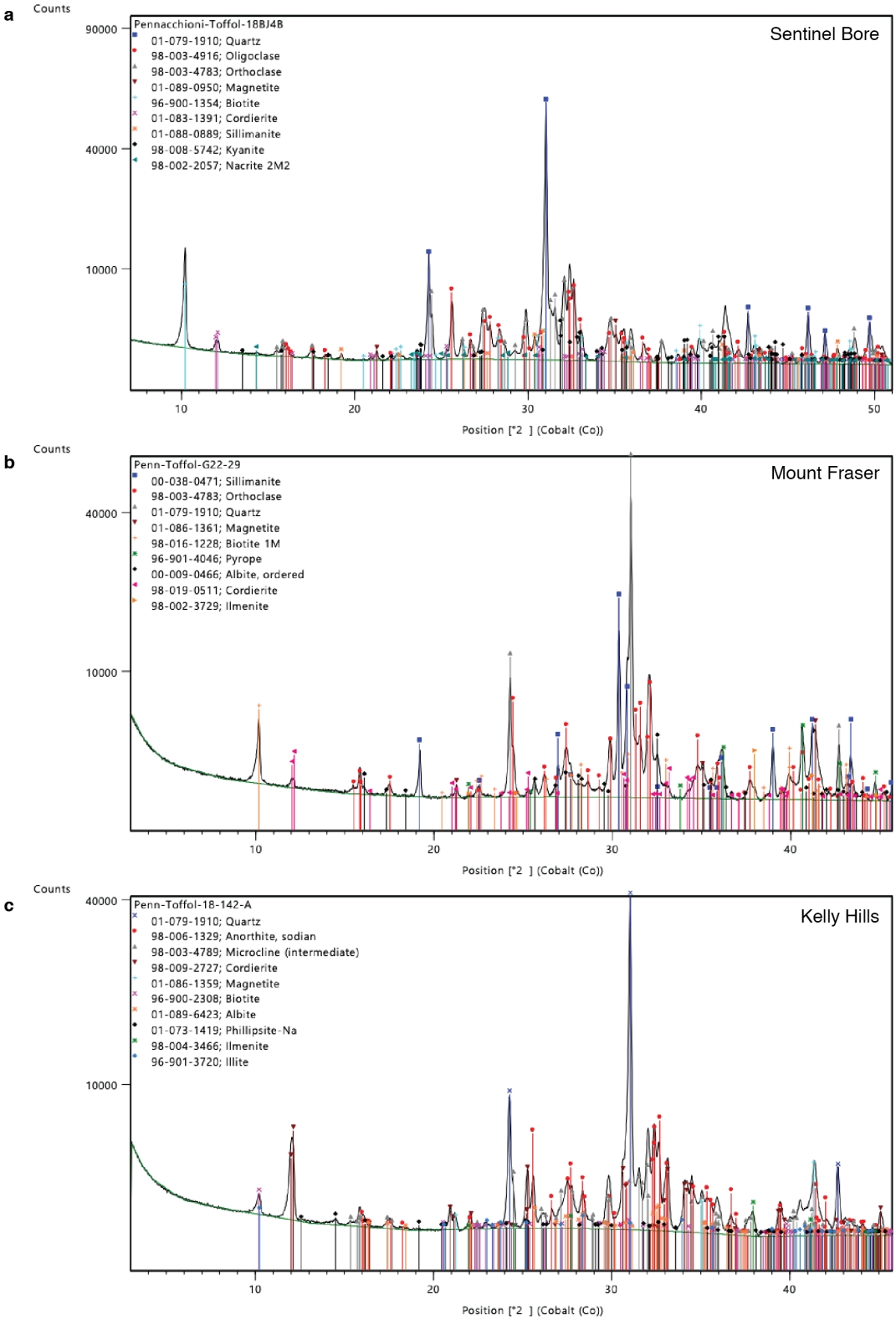

App. Fig. 1 | XRPD spectra. Mineralogical composition of the investigate samples from: **a,** Sentinel Bore; **b,** Mount Fraser; **c,** Kelly Hills.

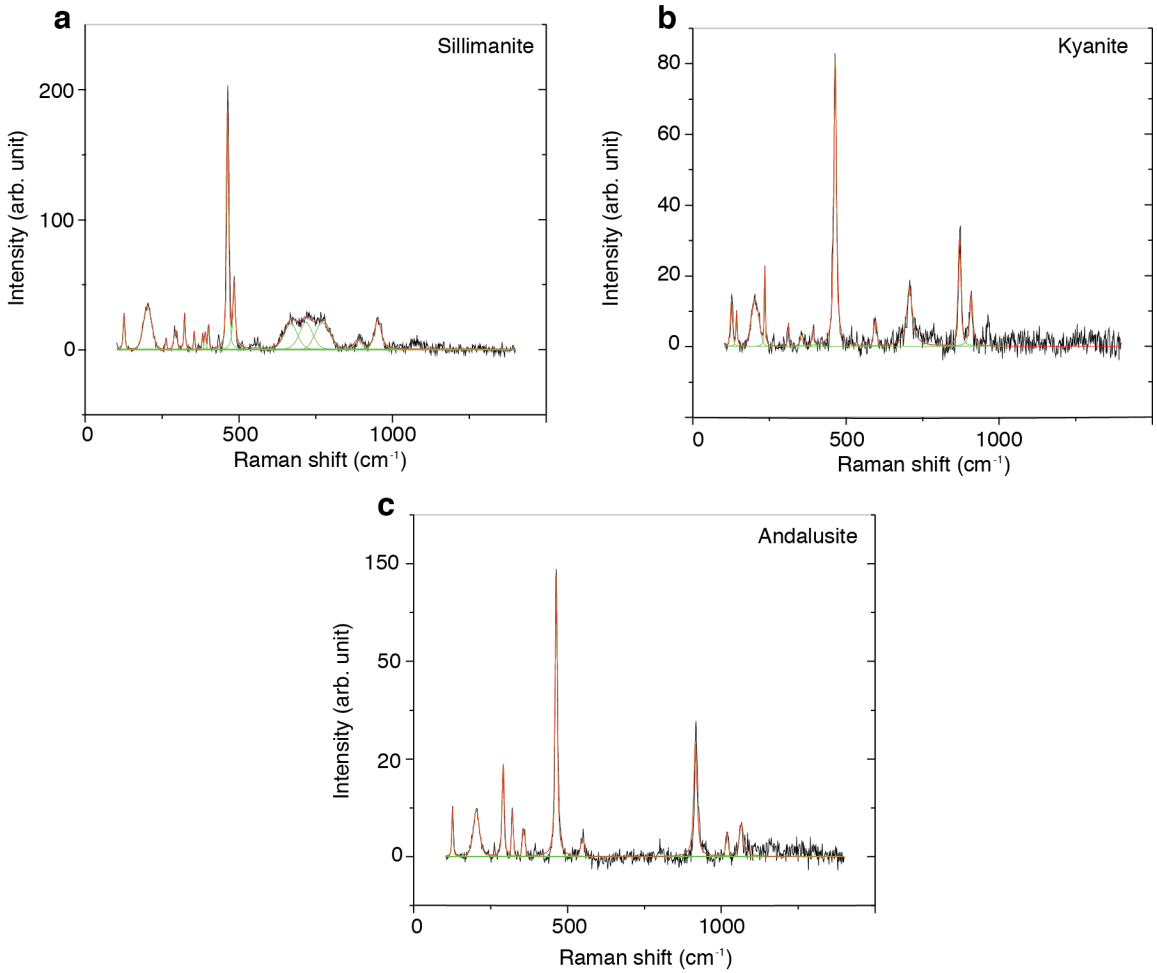

App. Fig. 2 | Raman spectra of microlites in a pseudotachylyte injection vein from Sentinel Bore. a, Sillimanite needles overgrowing a sillimanite clast. **b,** kyanite microlite. **c,** andalusite intergrowth with quartz. Due to the extremely small grain size of the studied microlites, all the spectra show peaks of other phase (quartz, biotite).

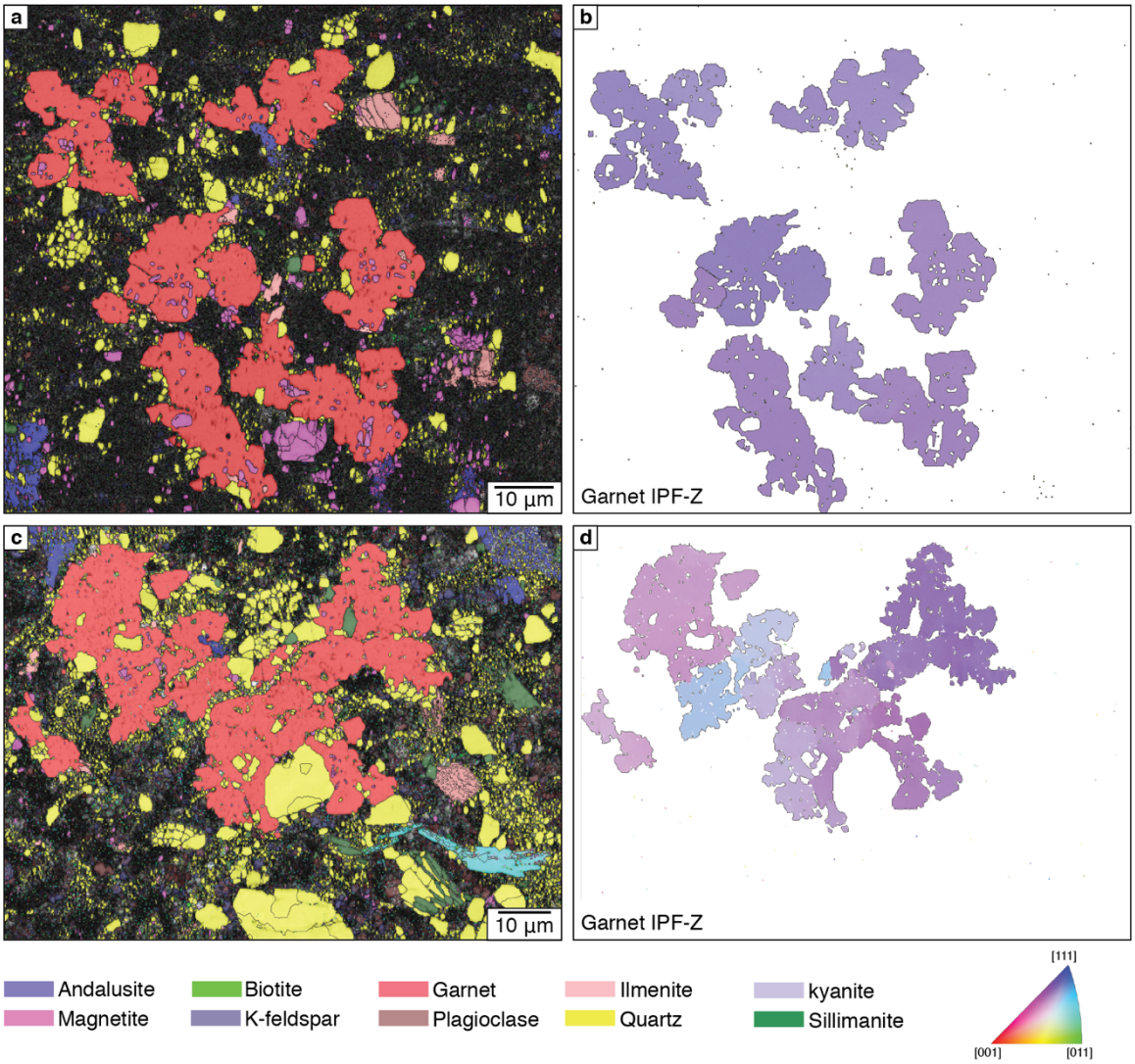

App. Fig. 3 | EBSD map of microlitic garnets from Sentinel Bore pseudotachylyte. a, c, phase maps plotted over EBSD band contrast. **b, d,** garnets colour-coded in function of their orientation according to the inverse pole figure reported in the bottom right corner.

%Ox	Sentinel Bore	Mount Fraser	Kelly Hills
SiO_2	66,03	57,99	66,51
TiO_2	0,78	1,03	0,77
Al_2O_3	15,99	25,74	16,48
Fe_2O_3	6,66	8,80	6,78
MnO	0,22	0,07	0,14
MgO	1,31	1,60	1,64
CaO	1,36	0,21	1,52
Na_2O	2,70	0,81	1,91
K_2O	4,67	4,62	3,85
P_2O_5	0,10	0,04	0,04
Tot	99,82	100,91	99,64
L.O.I.	0,50	0,40	0,88

Tab. 1 | XRF bulk rock compositions

Appendix 2

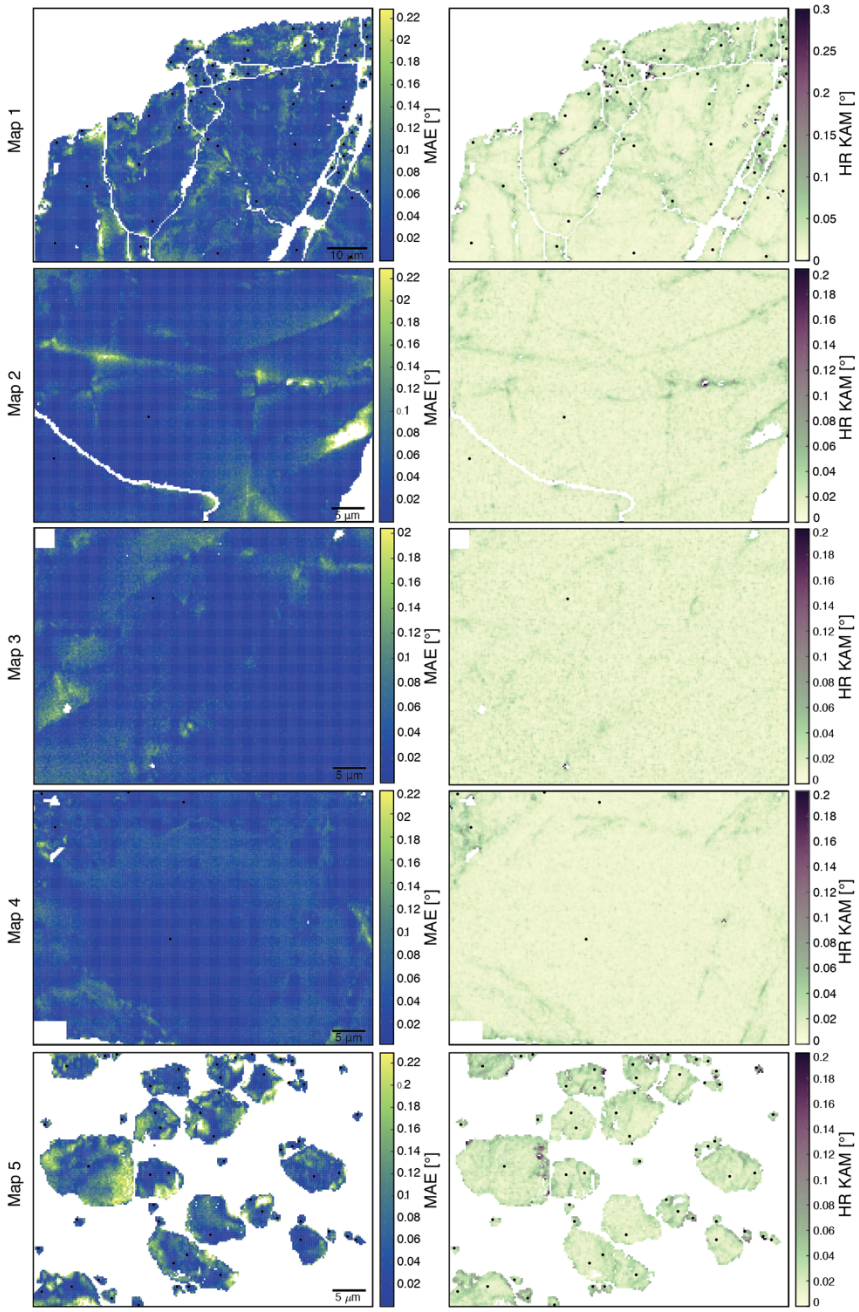

App. 2 Fig. 1 |Mean angular error (MAE) and high-resolution kernel average misorientation (HR-KAM). MAE is a parameter useful to evaluate the quality of the crosscorrelation. Only points with MAE below 0.2292° are considered reliable for the analysis.
HR-KAM, calculated in every pixel as the average misorientation with respect to the surrounding pixels, is useful to visualize the noise contribution in the analysis.

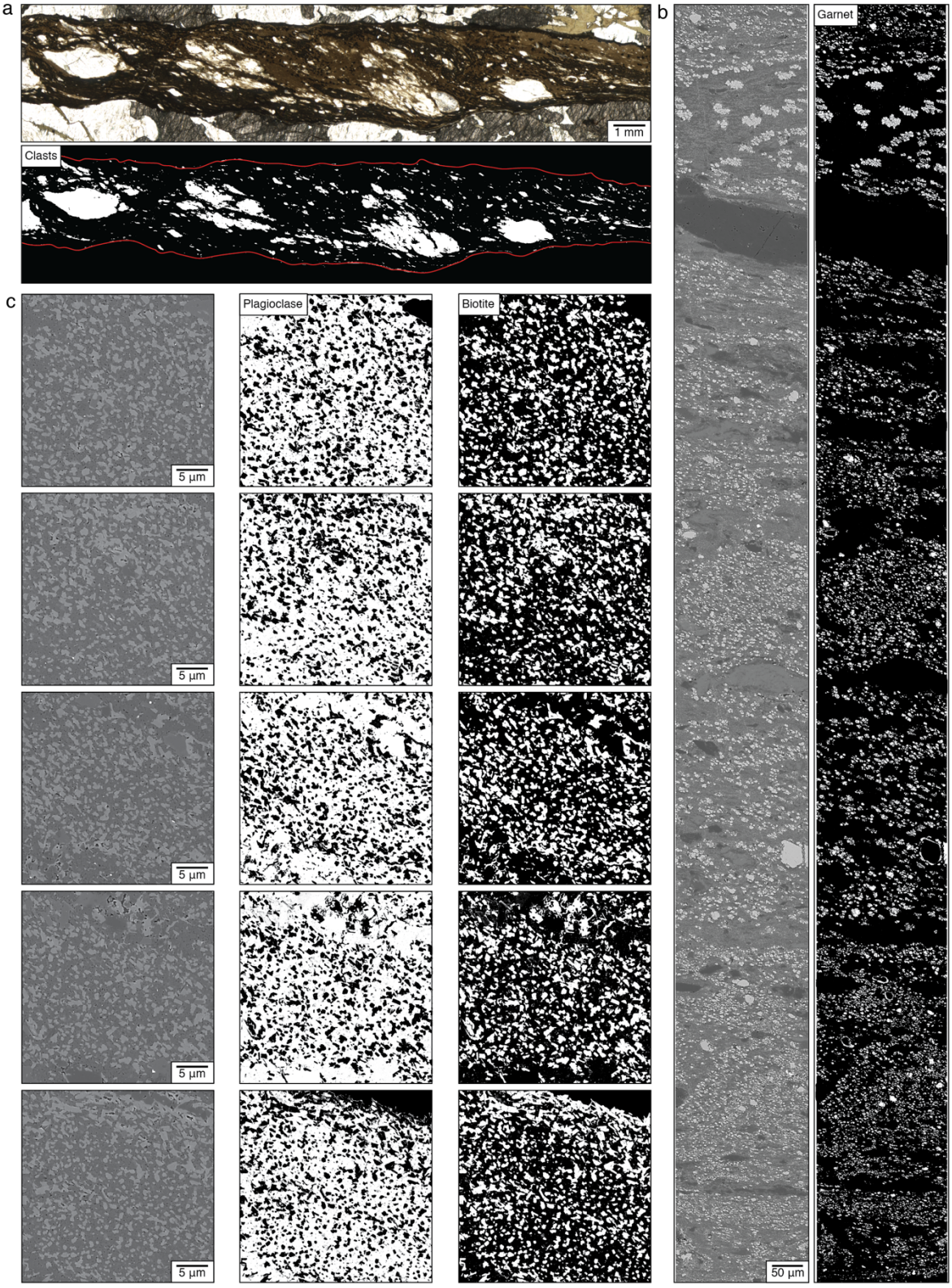

App. 2 Fig. 2 | a, Pseudotachylyte fault vein and segmented clasts. **b,** BSE transect across the pseudotachylyte and segmented garnet microlites. **c,** High-resolution BSE images of the pseudotachylyte matrix and segmented plagioclase and biotite.

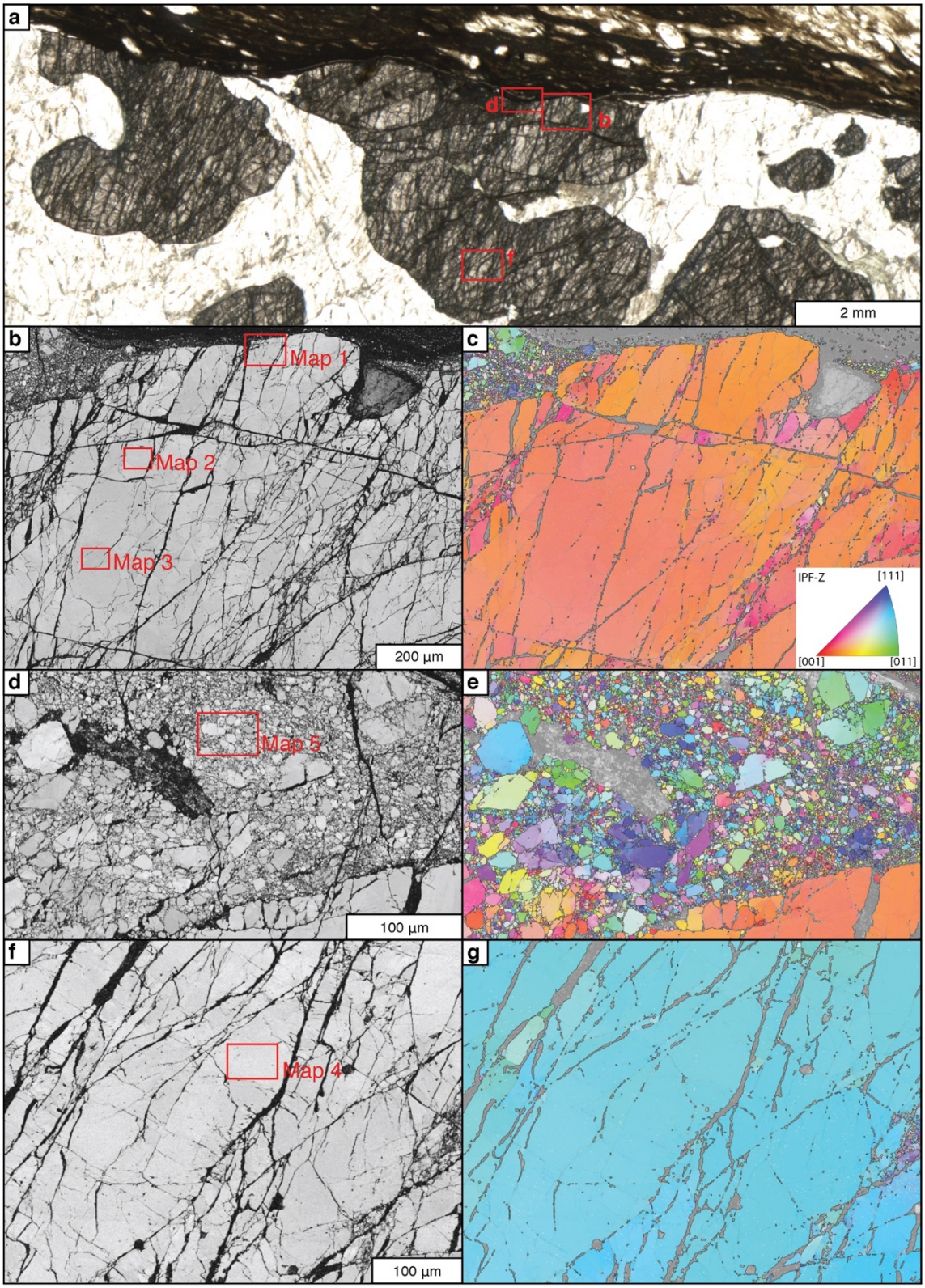

App. 2 Fig. 3 | a, Visible light image of the investigated garnets. Red squares mark the locations of the EBSD maps. **b, d, f**, Band-contrast EBSD maps. Red squares mark the locations of the five HR-EBSD maps. **c, e, g**, EBSD maps colour-coded by crystal orientation according to the inverse pole figure inset in the bottom-right corner of **c** with respect to the Z direction.

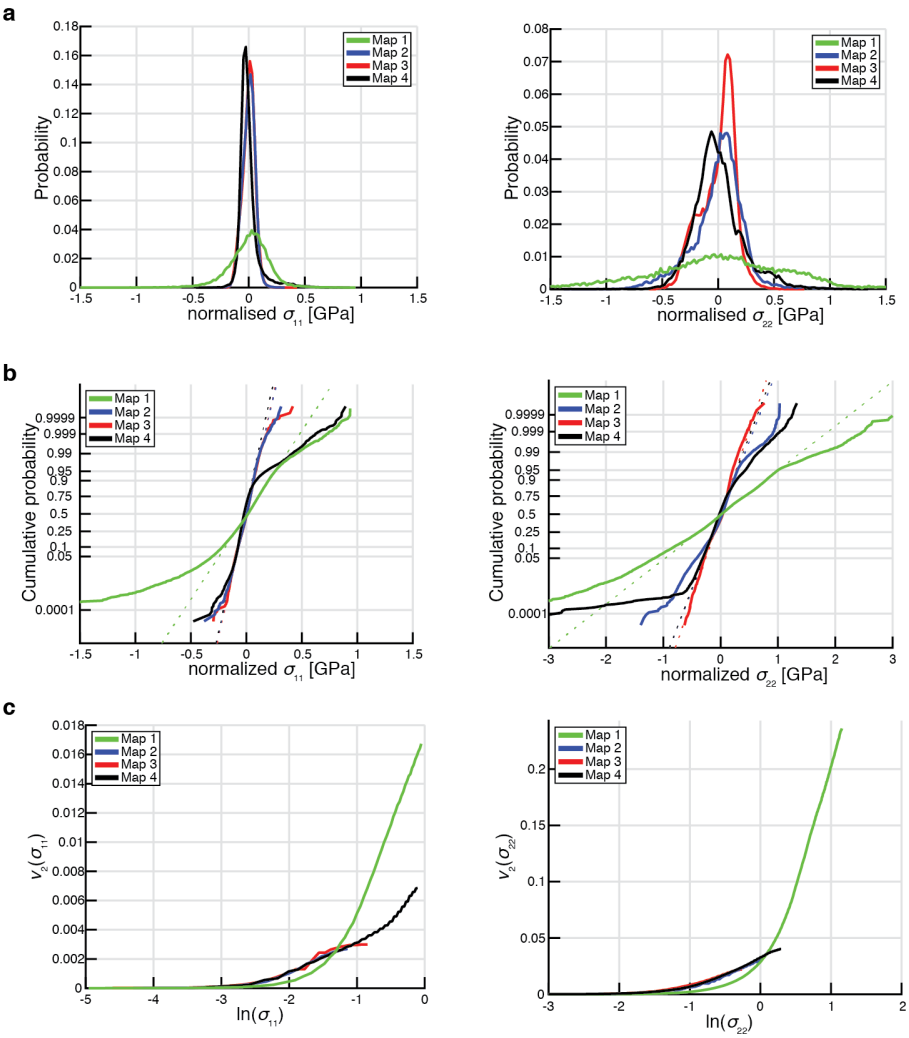

App. 2 Fig. 4 | Probability distribution and distribution form analysis of the stress heterogeneities for σ_{11} and σ_{22}. a, probability distribution. **b,** normalized probability distribution. **c,** restricted second moment of the probability distribution

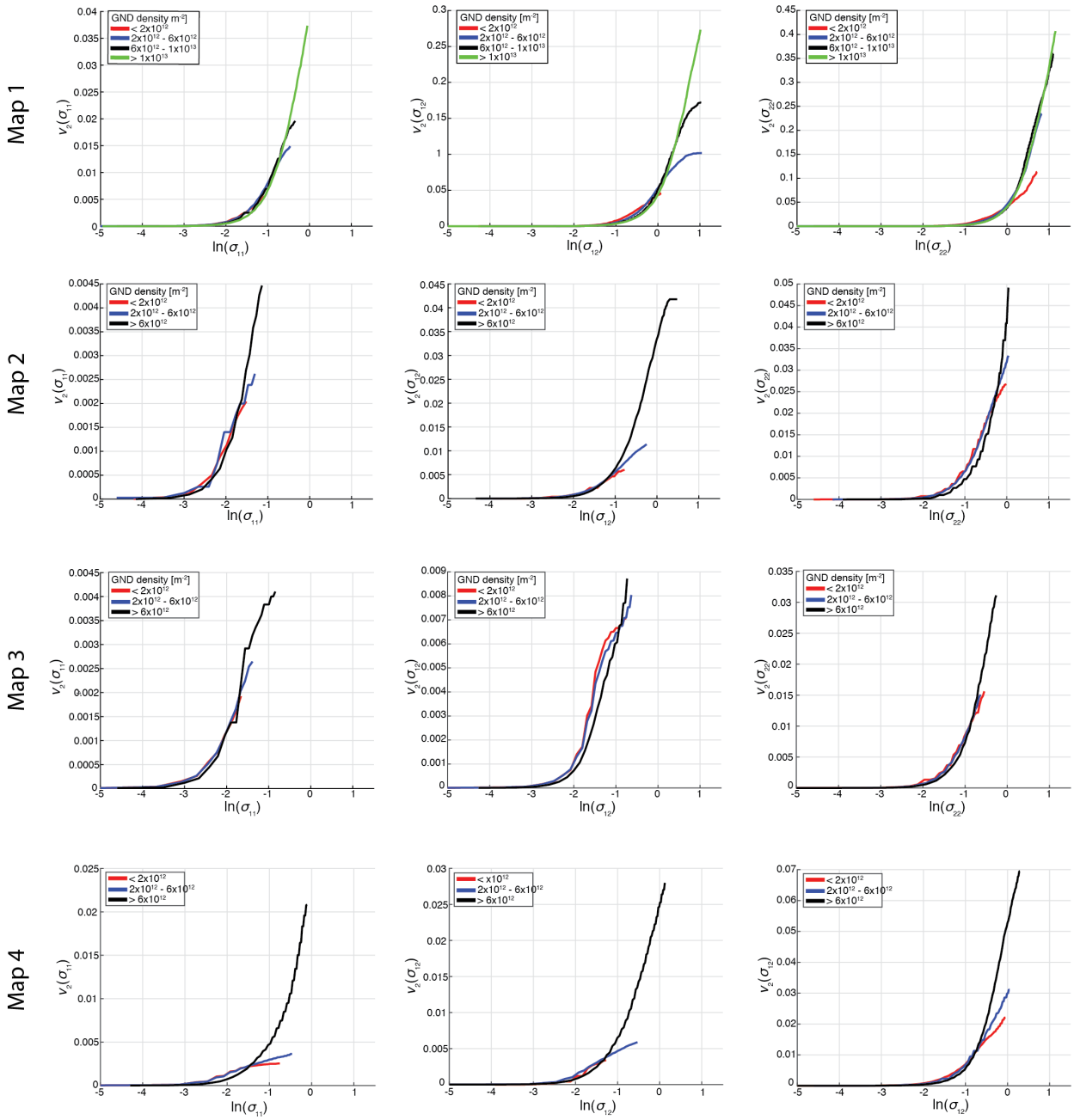

App. 2 Fig. 5 | Restricted second moments of the stress distributions for the three in-plane components of the residual stress. Different subsets are plotted for every map based on intervals of increasing GND densities.

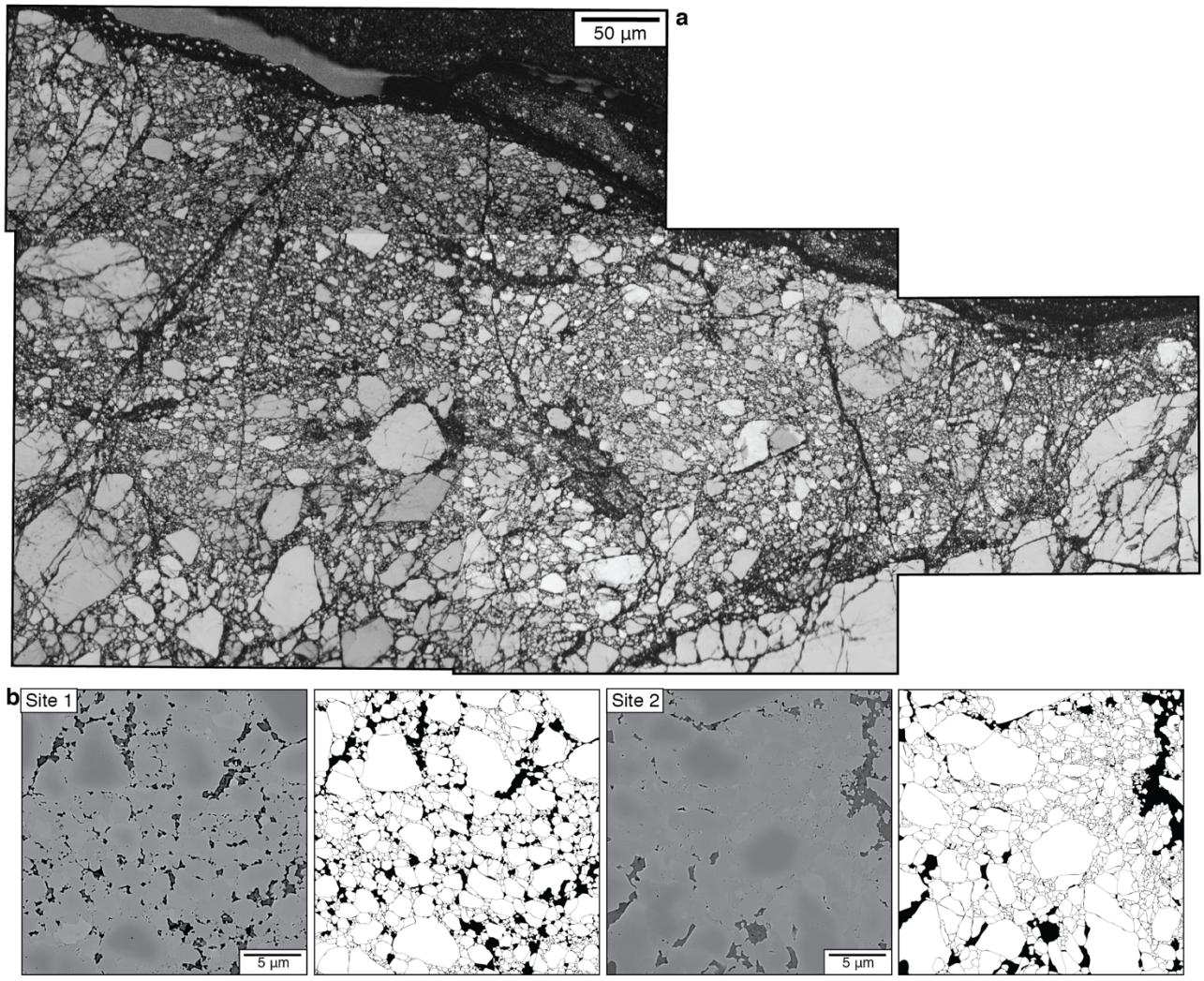

App. 2 Fig. 6| a, EBSD band-contrast maps of the cataclastic domain considered for clast-size analysis and presented in Fig. 6. **b,** High-resolution BSE images and segmented garnet grains for the Sites 1 and 2.

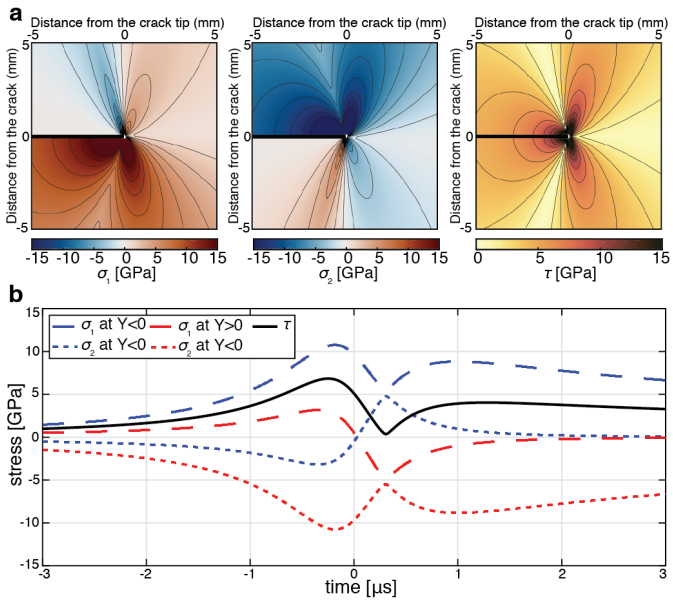

App. 2 Fig. 7 | Stress field surrounding the tip of a mode II propagating fracture. Stress components calculated for a fracture propagating at a velocity corresponding to 0.9 of the shear wave velocity, close to Rayleigh velocity (0.92 of the shear wave velocity) in a material with elastic properties typical of middle-crustal felsic rocks (see Methods). Calculations are performed in a reference frame moving with the tip of the fracture and in a fixed frame. **a,** aximum principal stress, minimum principal stress and shear stress around the tip of a propagating fracture. The interval of stress contours is 1.5 GPa. **b**, Stress plotted as function of time at a fixed point located at a distance of 3 mm (above, Y>0, and below, Y<0) from the rupture surface during fracture propagation. At t = 0 s, the fracture tip is at the shortest distance from the fixed point; the fracture tip is approaching the point and proceeding away from it at negative and positive values, respectively.

Supplementary MATLAB code: 1 | 2D stress distribution around the tip of a propagating fracture

```
% this matlab script is used to calculate the stress field around the tip
% of a propagating fracture. Calculations are after "Freund 1990 - DYNAMIC
% FRACTURE MECHANICS"

%% input parameters
clear , close all

global Xmm Ymm

rho = 2800; %density [kg*m^-3]
nu = 0.22; %Poisson's ratio
mu = 30e9; %Shear Modulus [Pa]

Cd = sqrt((2*mu+(2*mu*nu/(1-2*nu)))/rho); %compressional wave velocity
Cs = sqrt(mu/rho); %Shear wave velocity
Cr = 0.92*Cs; %Rayleigh wave velocity
v = 0.9*Cs; %propagation velocity

dx=1e-4; dy=1e-4;
x=-5e-3:dx:5e-3; xnum=size(x,2);
y=-5e-3:dy:5e-3; ynum=size(y,2);
[X,Y]=meshgrid(x,y);
Xmm=X.*1e+3; Ymm=Y.*1e+3;

r = (X.^2+Y.^2).^0.5; %radius [m]
theta= atan2d(Y,X); % angle [¬∞]

%% calculate stresses
ad = sqrt(1-v^2/Cd^2);
as = sqrt(1-v^2/Cs^2);
D = 4*ad*as - (1+as^2)^2;

G = 1e6; % energy-release-rate = fracture energy [J/m^2]
K = ( (G*2*mu*Cs^2*D) / (v^2*as) )^0.5; % stress intensity factor

cost=cosd(theta);   sint=sind(theta);
thetad = atan2d(ad*sint,cost);
thetas = atan2d(as*sint,cost);

gd = sqrt(1-(v*sind(theta)/Cd).^2);
gs = sqrt(1-(v*sind(theta)/Cs).^2);

% angular variation of stress components
sig11 = -2*as/D * ((1+2*ad^2-as^2)*sind(0.5*thetad)./sqrt(gd) - ...
   (1+as^2)*sind(0.5*thetas)./sqrt(gs));

sig12 = 1/D * (4*ad*as*cosd(0.5*thetad)./sqrt(gd) - ...
   (1+as^2)^2*cosd(0.5*thetas)./sqrt(gs));
```

```
sig22 = 2*as*(1+as^2)/D * (sind(0.5*thetad)./sqrt(gd) -...
   sind(0.5*thetas)./sqrt(gs));

% stress components
S11 = K./sqrt(2*pi*r) .* sig11;
S12 = K./sqrt(2*pi*r) .* sig12;
S22 = K./sqrt(2*pi*r) .* sig22;
SII = (0.5.*(S11.^2+S22.^2)+S12.^2).^0.5;

% principal stress
S1 = (S11+S22)/2 + ( ((S11-S22)/2).^2 + S12.^2 ).^(1/2);
S2 = (S11+S22)/2 - ( ((S11-S22)/2).^2 + S12.^2 ).^(1/2);
TAU = (((S11-S22)/2).^2 + S12.^2) .^0.5;
% mean stress
Smean = (S1+S2)./2;

% polar coordinates
Srr = S11 .* (cosd(theta)).^2 + S22 .* (sind(theta)).^2 + S12 .* sind(2*theta);
Stt = S11 .* (sind(theta)).^2 + S22 .* (cosd(theta)).^2 - S12 .* sind(2*theta);
Srt = sind(theta) .* cosd(theta) .* (S22-S11) + S12 .* cosd(2*theta);
Sii = (0.5.*(Srr.^2+Stt.^2)+Srt.^2).^0.5;

%% plot figures
st_range = 15000;
st_step = 1500;

%figure(1)
ss = get(0,'ScreenSize');
f = figure('Name',['Stress tensor components (Cartesian)'],...
   'NumberTitle','off','OuterPosition',[0.0*ss(3) 0.6*ss(4) 0.3*ss(3) 0.45*ss(4)],'Visible','off');
figure(f)
plot2D(221,S11./1e+6,-st_range,st_step,st_range,'\sigma_{11}')
plot2D(222,S22./1e+6,-st_range,st_step,st_range,'\sigma_{22}')
plot2D(223,S12./1e+6, -st_range/2,st_step,st_range/2,'\sigma_{12}')
plot2D(224,SII./1e+6,    0,st_step,st_range,'\sigma_{II}')

%figure(2)
f = figure('Name',['Stress tensor components (polar)'],...
   'NumberTitle','off','OuterPosition',[0.33*ss(3) 0.6*ss(4) 0.3*ss(3) 0.45*ss(4)],'Visible','off');
figure(f)
plot2D(221,Srr./1e+6,-st_range,st_step,st_range,'\sigma_{rr}')
plot2D(222,Stt./1e+6,-st_range,st_step,st_range,'\sigma_{\theta\theta}')
plot2D(223,Srt./1e+6,-st_range,st_step,st_range,'\sigma_{r\theta}')
plot2D(224,Sii./1e+6,    0,st_step,st_range,'\sigma_{II}')

%figure(3)
f = figure('Name',['Principal stress components'],...
   'NumberTitle','off','OuterPosition',[0.66*ss(3) 0.6*ss(4) 0.3*ss(3) 0.45*ss(4)],'Visible','off');
figure(f)
plot2D(221,S1./1e+6,-st_range,st_step,st_range,'\sigma_{max}')
plot2D(222,S2./1e+6,-st_range,st_step,st_range,'\sigma_{min}')
```

```
plot2D(223,TAU./1e+6,   0,st_step, st_range/2,'\tau')
plot2D(224,Smean./1e+6,-st_range,st_step,st_range,'\sigma_{mean}')



% plotting function
function plot2D(sp,A,cmin,cstp,cmax,tname)

global Xmm Ymm

subplot(sp)
pcolor(Xmm,Ymm,A)
shading interp
colorbar
axis image
hold on
c=cmin:cstp:cmax;
contour(Xmm,Ymm,A,c,'k');
%clabel(c,h)
hold off
caxis([cmin cmax ])
title(tname)
xlabel('Distance ahead of the crack tip (mm)')
ylabel('Distance from the crack (mm)')

% cl_pt = '/Users/giovannitoffol/Documents/MATLAB/CRAMERI_color';
% load([cl_pt,'/','vik.mat']); %colorscale
% load([cl_pt,'/','lajolla.mat']); %colorscale
% colormap(vik)


%Plot crack as a thick line wide as half the domain along X
cnum=find(Xmm(1,:)==0,1);
crack=zeros(1,cnum);
hold on
plot(Xmm(1,1:cnum),crack,'r','LineWidth',5)
hold off

end
```

Supplementary MATLAB code 2 | Stress during fracture propagation in a fixed reference frame

```
% this matab script is used to calculate the stress during the propagation
% of a fracture in a fixed reference frame. Calculations are after "Freund
% 1990 - DYNAMIC FRACTURE MECHANICS"

%% input parameters
clear all, close all

rho = 2800; %density [kg*m^-3]
nu = 0.22; %Poisson's ratio
mu = 30e9; %Shear Modulus [Pa]

Cd = sqrt((2*mu+(2*mu*nu/(1-2*nu)))/rho); %compressional wave velocity
Cs = sqrt(mu/rho); %Shear wave velocity
Cr = 0.92*Cs; %Rayleigh wave velocity
v = 0.9*Cs; %propagation velocity
y_pos = 0.003; % y coordinate (fixed) [m]
y_pos = [-y_pos,y_pos];

dt=1e-8;
time = -3e-6:dt:3e-6; % time [s] (microseconds)

ad = sqrt(1-v^2/Cd^2);
as = sqrt(1-v^2/Cs^2);
D = 4*ad*as - (1+as^2)^2;

G = 1e6; % energy-release-rate = fracture energy [J/m^2]
K = ( (G*2*mu*Cs^2*D) / (v^2*as) )^0.5; % stress intensity factor calculated

%% calculate stress
for i=1:2
    y = y_pos(i);
    x = v*time; % x coordinate [m]
    r = sqrt(x.^2+y^2); % radius [m]
    theta = atan2d(y,-x); % angle [∞]

    % calculate thetad, thetas, gammad, gammas
    cost=cosd(theta);   sint=sind(theta);
    thetad = atan2d(ad*sint,cost);
    thetas = atan2d(as*sint,cost);

    gd = sqrt(1-(v*sind(theta)/Cd).^2);
    gs = sqrt(1-(v*sind(theta)/Cs).^2);

    % angular variation of stress components
    sig11 = -2*as/D * ((1+2*ad^2-as^2)*sind(0.5*thetad)./sqrt(gd) - ...
        (1+as^2)*sind(0.5*thetas)./sqrt(gs));

    sig12 = 1/D * (4*ad*as*cosd(0.5*thetad)./sqrt(gd) - ...
        (1+as^2)^2*cosd(0.5*thetas)./sqrt(gs));
```

```
    sig22 = 2*as*(1+as^2)/D * (sind(0.5*thetad)./sqrt(gd) -...
        sind(0.5*thetas)./sqrt(gs));

    % stress components
    S11 = K./sqrt(2*pi*r) .* sig11;
    S12 = K./sqrt(2*pi*r) .* sig12;
    S22 = K./sqrt(2*pi*r) .* sig22;

    % principal stress
    S1{i} = (S11+S22)/2 + ( ((S11-S22)/2).^2 + S12.^2 ).^(1/2);
    S2{i} = (S11+S22)/2 - ( ((S11-S22)/2).^2 + S12.^2 ).^(1/2);
    TAU{i} = (((S11-S22)/2).^2 + S12.^2) .^0.5;
    % mean stress
    Smean{i} = (S1{i}+S2{i})./2;
    % second invariant of the stress tensor
    SII{i} = (0.5.*(S11.^2+S22.^2)+S12.^2).^0.5;

end


%% figure
figure(1)
subplot(321)
plot(time,S1{1}/1e6,'b','LineWidth',2)
hold on
plot(time,S1{2}/1e6,'r','LineWidth',2)
%ylim([-6e3 1.4e4])
grid on
legend({'\sigma_1 at Y<0','\sigma_1 at Y>0'},'FontSize',14)
xlabel('time [s]'), ylabel('stress [MPa]')

subplot(322)
plot(time,S2{1}/1e6,'b','LineWidth',2)
hold on
plot(time,S2{2}/1e6,'r','LineWidth',2)
%ylim([-6e3 1.4e4])
grid on
legend({'\sigma_2 at Y<0','\sigma_2 at Y>0'},'FontSize',14)
xlabel('time [s]'), ylabel('stress [MPa]')

subplot(323)
plot(time,TAU{1}/1e6,'b','LineWidth',2)
hold on
plot(time,TAU{2}/1e6,'r--','LineWidth',2)
%ylim([-6e3 1.4e4])
grid on
legend({'\tau at Y<0','\tau at Y>0'},'FontSize',14)
xlabel('time [s]'), ylabel('stress [MPa]')

subplot(324)
```

```
plot(time,Smean{1}/1e6,'b','LineWidth',2)
hold on
plot(time,Smean{2}/1e6,'r','LineWidth',2)
%ylim([-6e3 1.4e4])
grid on
legend({'(\sigma_1 + \sigma_2) / 2 at Y<0','(\sigma_1 + \sigma_2) / 2 at Y>0'},'FontSize',14)
xlabel('time [s]'), ylabel('stress [MPa]')

subplot(325)
plot(time,SII{1}/1e6,'b','LineWidth',2)
hold on
plot(time,SII{2}/1e6,'r--','LineWidth',2)
%ylim([-6e3 1.4e4])
grid on
legend({'\sigma_{II} at Y<0','\sigma_{II} at Y>0'},'FontSize',14,'location','southeast')
xlabel('time [s]'), ylabel('stress [MPa]')


%% figure (as in the paper)
figure(2)
plot(time*1e6,S1{1}/1e9,'b--','LineWidth',2)
hold on
plot(time*1e6,S2{1}/1e9,'b:','LineWidth',2)
plot(time*1e6,S1{2}/1e9,'r--','LineWidth',2)
plot(time*1e6,S2{2}/1e9,'r:','LineWidth',2)
plot(time*1e6,TAU{1}/1e9,'k','LineWidth',2)
%ylim([-6e3 1.4e4])
grid on
legend({'\sigma_1 at Y<0','\sigma_2 at Y<0','\sigma_1 at Y>0','\sigma_2 at Y>0','\tau',}...
   ,'FontSize',14,'NumColumns',3,'Location','NW')
xlabel('time [\mus]','FontSize',14), ylabel('stress [GPa]','FontSize',14)
```

Appendix 3

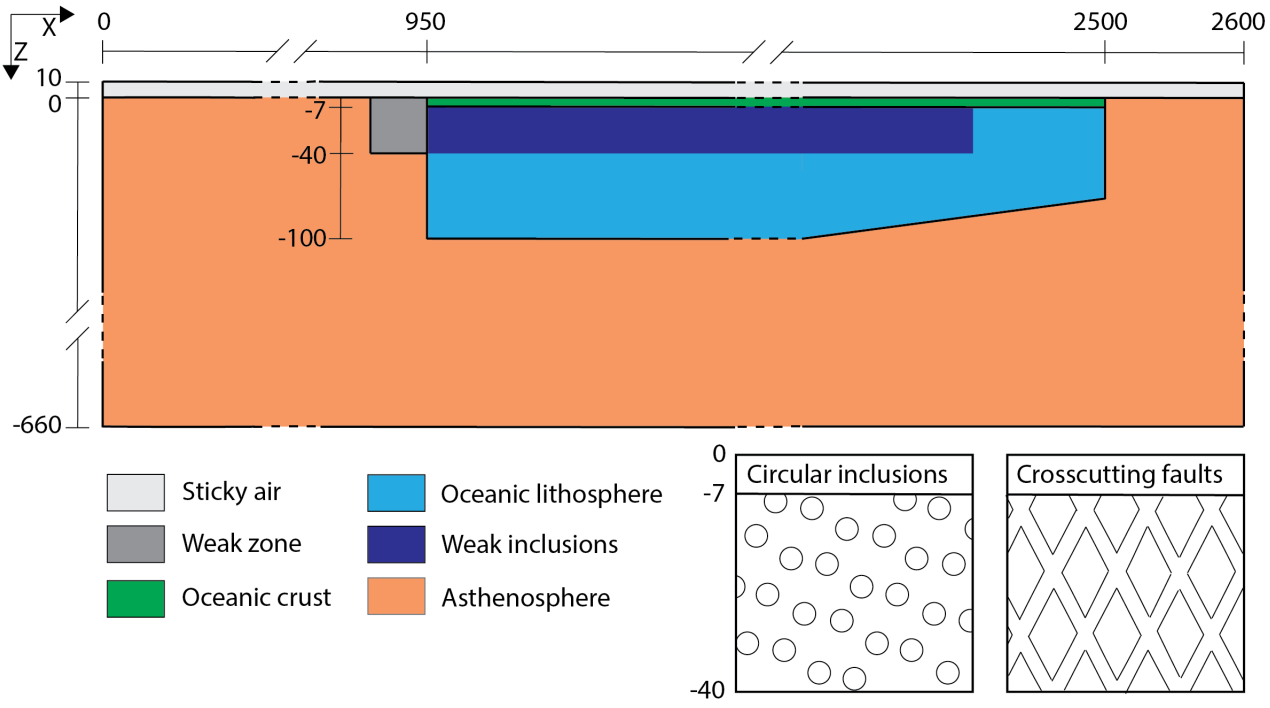

App. 3 Fig. 1 | Sketch of the initial setup of the subduction simulations. Distances are in km.

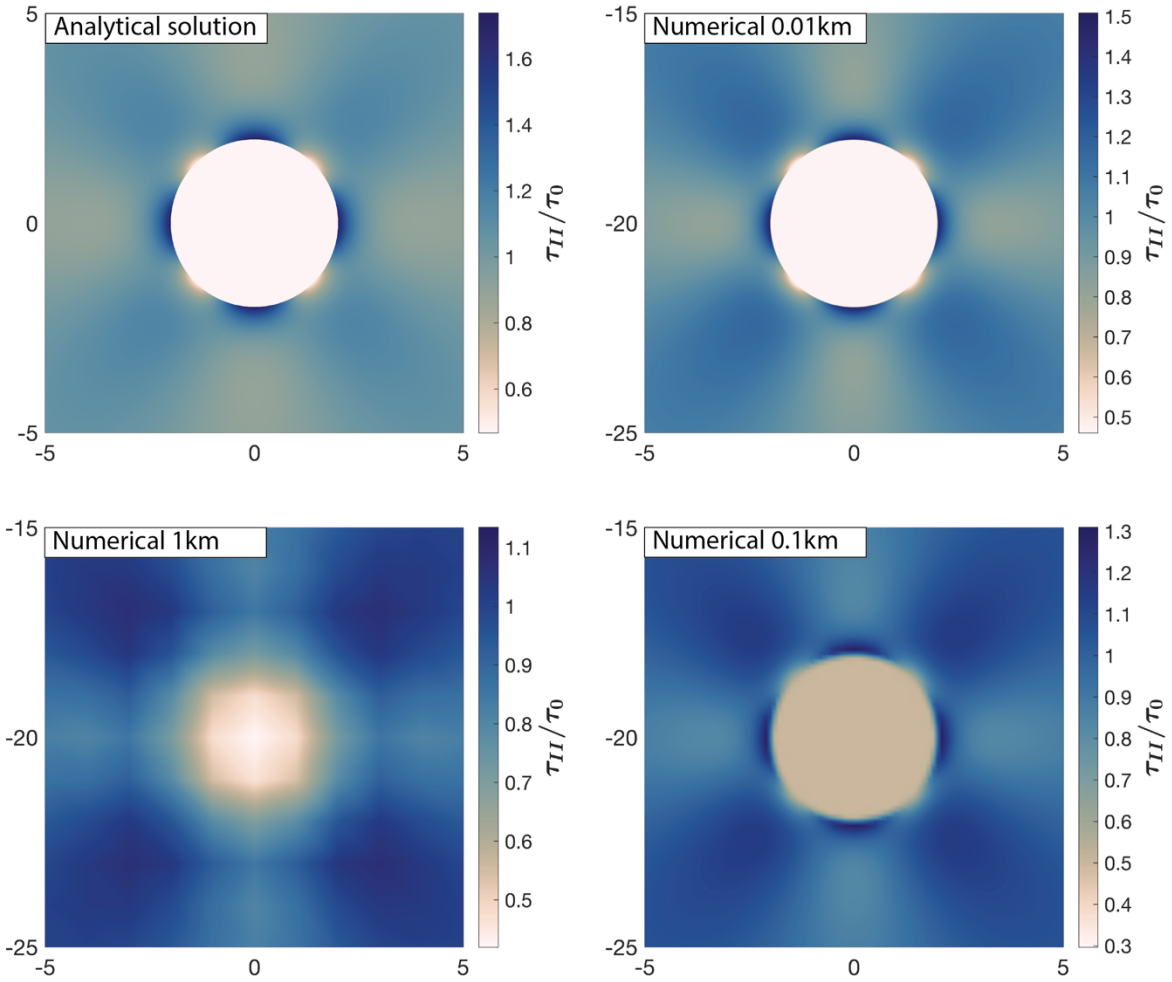

App. 3 Fig. 2 | Magnitude of the deviatoric stress normalized to the far field stress (τ_{II}/τ_0) around a weak inclusion (G = 30 GPa) in a strong matrix (G = 100 GPa). Values predicted by the analytical solution and values of the first timestep of small-scale benchmark models calculated with LaMEM with resolutions of 1, 0.1 and 0.01 km. Distances are in km.

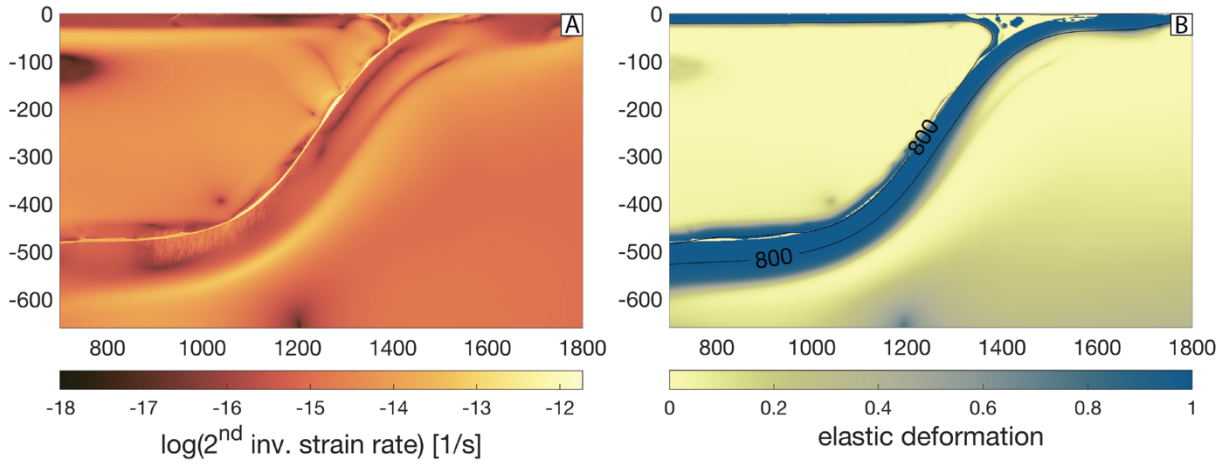

App. 3 Fig. 3 | Subducting slab (homogenous case, viscous rheology defined by diffusion and dislocation creep; model 14). A) Logarithm of the second invariant of the deviatoric strain rate. B) Fraction of deformation accommodated elastically in the slab (0 = deformation accommodated only by viscous / plastic mechanisms; 1 = deformation accommodated elastically). The value is calculated as: $1 - (\eta_{vep}/\eta_{vp})$. The 800 °C isotherm is plotted as a reference.

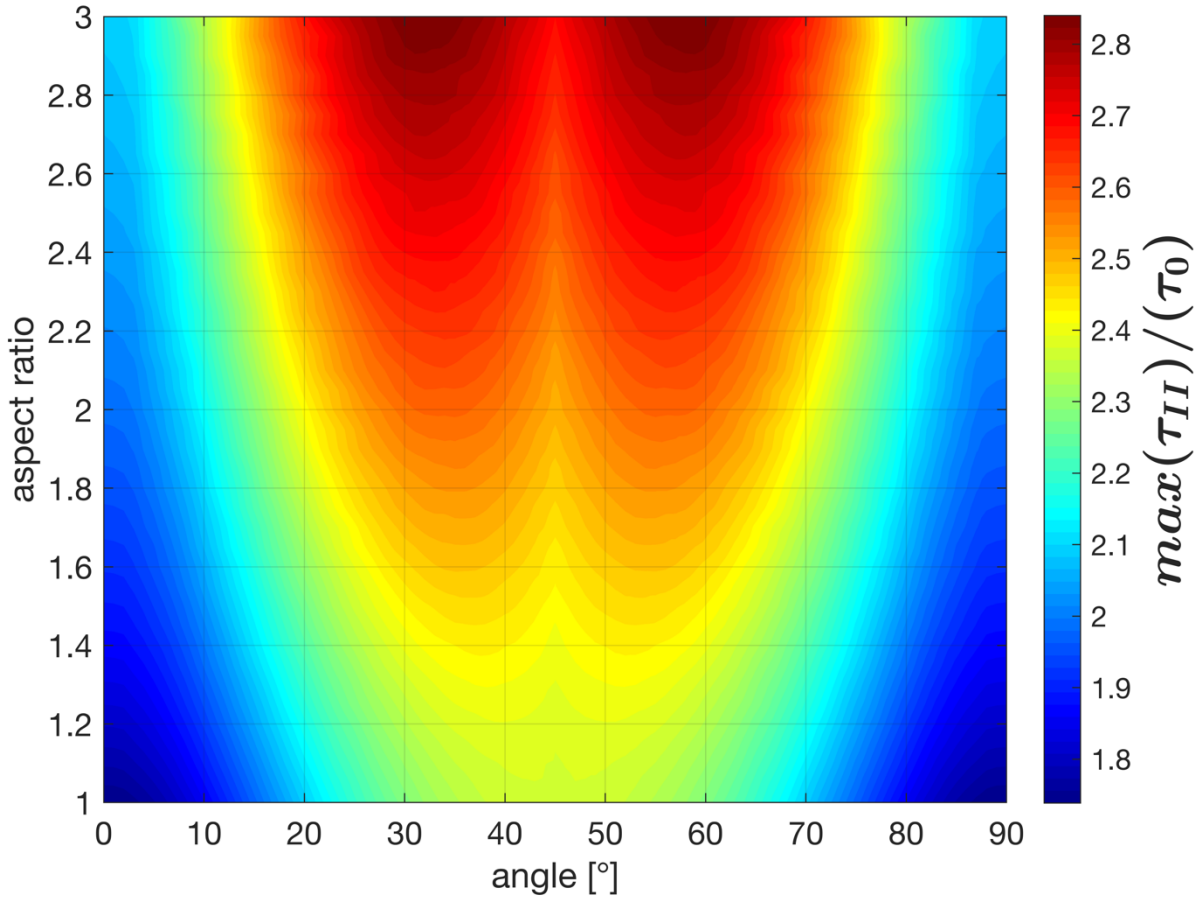

App. 3 Fig. 4 | Dependence of the stress amplification (magnitude of the deviatoric stress normalized to the far field stress, $max(\tau_{II})/\tau_0$) around a weak inclusion ($G_i = 0.3*G_m$, i,m for inclusion and matrix respectively) on (i) the aspect ratio of the inclusion, and (ii) on the orientation of the compression axis to the long axis of the elliptic inclusion (parallel to the long axis (0°) to perpendicular to the long axis (90°)).

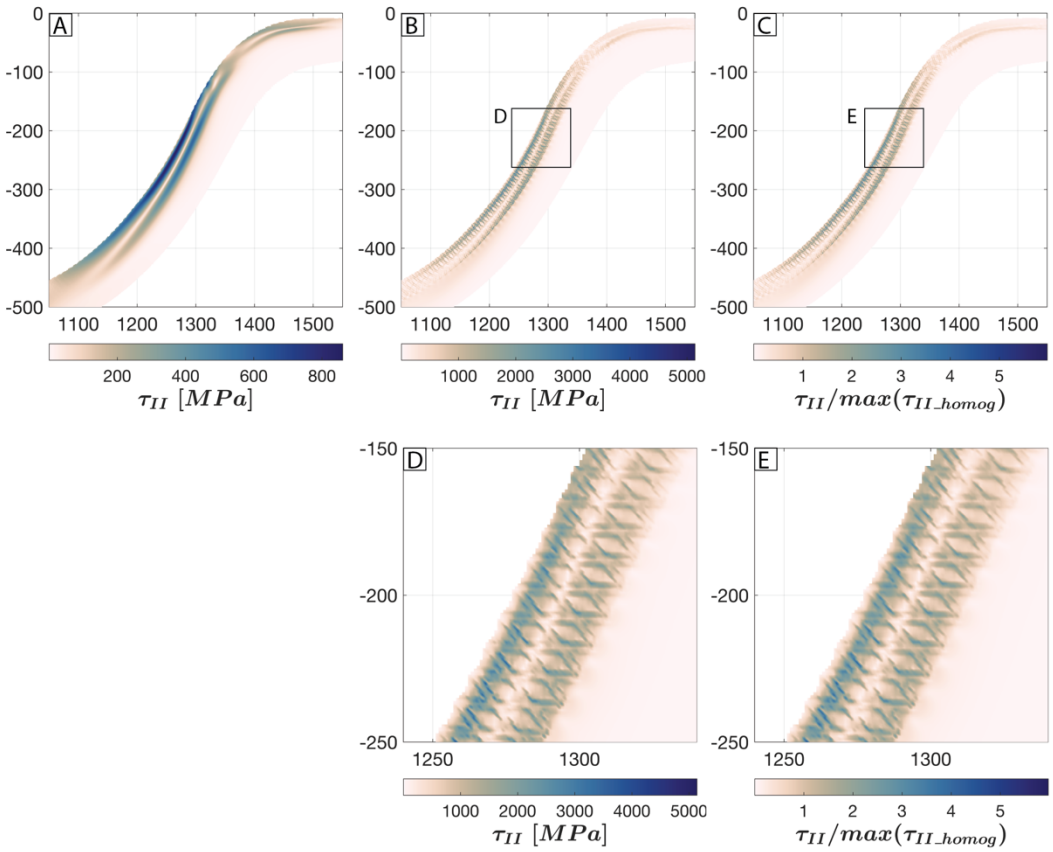

App. 3 Fig. 5 | Magnitude of the deviatoric stress (τ_{II}) in the subducting plate for models with LPT and cross-cutting weak faults. A) homogeneous case (*model 34*). B) Fault-like distribution of the weak material (G = 30 GPa) (*model 35*). C) same as B) with stress normalized to the maximum value of the homogeneous case ($\tau_{II}/max(\tau_{II\_homog})$). D,E) details of B,C) showing the region with highest deviatoric stress. Distances are in km.

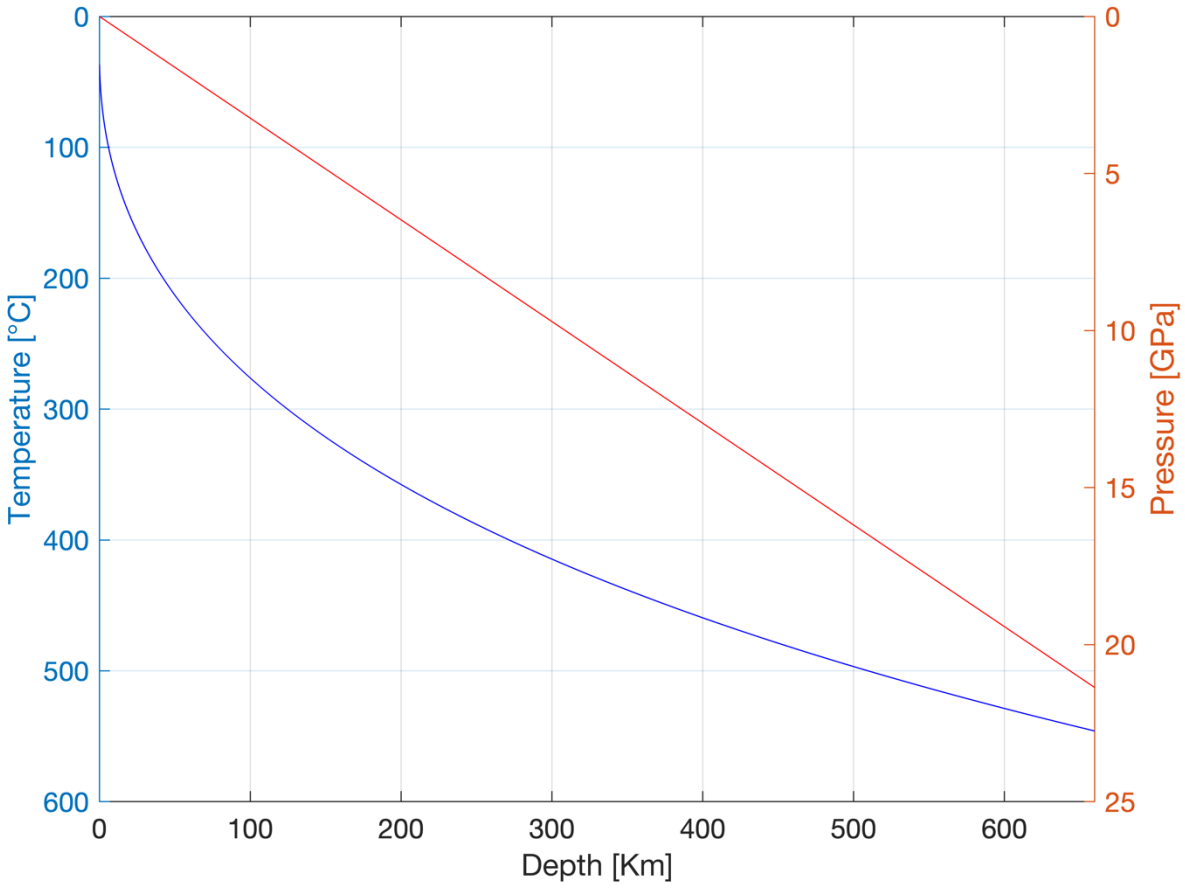

App. 3 Fig. 6 | Pressure and temperature profile of the subducting slab considered in *Fig. 6*. The temperature is referred to the inner colder portion of the slab.

Analytical solutions of the stress field around an inclusion

Analytical solutions for the case of an inhomogeneity within a homogeneous matrix under a prescribed stress field are used to assess the reliability of our simulations. The perturbation of the stress field is calculated with the equivalent inclusion method (Eshelby, 1957, 1959; Jin et al., 2011) following the formulation proposed by Jin et al., 2014 for elliptical inclusions in plane-stress. The outer stress field is calculated as:

$$\begin{bmatrix}\sigma_{xx}\\ \sigma_{yy}\\ 2\sigma_{xy}\end{bmatrix} = \begin{bmatrix}\sigma^0_{xx}\\ \sigma^0_{yy}\\ 2\sigma^0_{xy}\end{bmatrix} + \begin{bmatrix}D_{11} & D_{12} & D_{13}\\ D_{21} & D_{22} & D_{24}\\ D_{41} & D_{42} & D_{44}\end{bmatrix}\begin{bmatrix}\sigma^*_{xx}\\ \sigma^*_{yy}\\ 2\sigma^*_{xy}\end{bmatrix}$$

where σ^0_{ij} are the components of the far field stress, $[D] = [H][T]^{-1}$ is a matrix containing the geometrical parameters ($[H]$ the tensor relating stress to eigenstrain, $[T]$ the tensor relating eigenstress to eigenstrain) and σ^*_{ij} are the components of the eigenstress inside the inclusion which depends upon the elastic parameters. For an exhaustive treatment of the topic refer to the quoted literature.
The implementation of these equations in a matlab script (Appendix *A.2*) allows calculation of the exterior stress field for various aspect ratios, orientation of the principal stress axes and shear moduli contrasts. Comparison with results from the numerical simulations always consider aspect ratio of 1 (circular inclusion).

References

1. Eshelby, J. D. (1957). The determination of the elastic field of an ellipsoidal inclusion, and related problems. Proceedings of the royal society of London. Series A. Mathematical and physical sciences, 241(1226), 376-396.
2. Eshelby, J. D. (1959). The elastic field outside an ellipsoidal inclusion. Proceedings of the Royal Society of London. Series A. Mathematical and Physical Sciences, 252(1271), 561-569.
3. Jin, X., Keer, L. M., & Wang, Q. (2011). A closed-form solution for the Eshelby tensor and the elastic field outside an elliptic cylindrical inclusion. Journal of applied mechanics, 78(3).
4. Jin, X., Wang, Z., Zhou, Q., Keer, L. M., & Wang, Q. (2014). On the solution of an elliptical inhomogeneity in plane elasticity by the equivalent inclusion method. Journal of Elasticity, 114(1), 1-18.

Matlab script for the analytical solutions
To run the code it is required to download Crameri's color maps (Crameri, 2018).

```
% Matlab script for the calculation of the stress field around an
% elliptical inhomogeneity.

% All the equations are after:
% "On the solution of an Elliptical Inhomogeneity in Plane Elasticity by the
% Equivalent Inclusion Method"
% X. Jin et al., Journal of Elasticity, 2014
% DOI 10.1007/s10659-012-9423-0

clear all
close all
%----------------------
%-------- INPUT --------
%far-field stress (negative = compression)
sigmaX = -67;
```

```
sigmaY = 67;
tauXY = 0;    %engineering shear stress (twice the tensorial shear stress)
theta = 0; %angle (rotation of stress axes)
%matrix
mu1 = 10e10; % shear modulus [Pa]
pois1 = 0.5; % Poisson ratio
%inhomogeneity
mu2 = 3e+10;
pois2 = 0.5;
AR = 1; %aspect ratio
a = 2;  b = a/AR; %ellipse
%define the grid
 x = (-5:0.005:5);
 y = (-5:0.005:5);

[X,Y] = meshgrid(x,y);
%----------------------

%stress rotation
if theta ~= 0
    S1=zeros(2);
    stress = [sigmaX tauXY; tauXY sigmaY];
    rot = [cosd(theta) -sind(theta); sind(theta) cosd(theta)];
    for i=1:2;for j=1:2 for k=1:2; for l=1:2
                S1(i,j)=S1(i,j) + rot(i,k)*rot(j,l)*stress(k,l);
            end;end;end;end
    sigmaX = S1(1,1),   sigmaY = S1(2,2),   tauXY = 2*S1(1,2),
end

t = b/a;
%Kolosov constants
K1 = (3-pois1)/(1+pois1);   K2 = (3-pois2)/(1+pois2); %(plane stress)
%K1 = 3-4*pois1; K2 = 3 - 4*pois2; %(plane strain)
% Dundurs parameters
A = ((K1+1)/mu1-(K2+1)/mu2) / ((K1+1)/mu1+(K2+1)/mu2);
B = ((K1-1)/mu1-(K2-1)/mu2) / ((K1+1)/mu1+(K2+1)/mu2);

Delta = (A^2-1)*(1-t)^2+4*t*(B+1)*(2*B-A-1);
Cxx = -2*(A^2+A-3*t*A*B+t*B+4*t*B^2);
Cxy = 2*(1+A)*(A-2*B-t*B);
Cyx = 2*t*(1+A)*(t*A-B-2*t*B);
Cyy = -2*t*(t*A^2+t*A-3*A*B+B+4*B^2);
C = [Cxx Cxy; Cyx Cyy];

%EIGENSTRESS
s = zeros(2,1); s = (1/Delta) * C*[sigmaX;sigmaY];
EsigmaX = s(1);
EsigmaY = s(2);
EtauXY = (4*t*(A-B))/((1+t)^2+A*(1-t)^2+4*t*B) * tauXY;
Eigenstress = [EsigmaX; EsigmaY; EtauXY];
```

```
for i=1:max(size(x))
   for j=1:max(size(y))

      if ((x(i)/a)^2+(y(j)/b)^2) > 1

         L = 0.5*(x(i)^2+y(j)^2-a^2-b^2+sqrt((x(i)^2+y(j)^2-a^2+b^2)^2+4*(a^2-b^2)*y(j)^2));
         Ra = a/sqrt(a^2+L);
         Rb = b/sqrt(b^2+L);
         mx = x(i)/(a^2+L);
         my = y(j)/(b^2+L);
         nx = mx/sqrt(mx^2+my^2);
         ny = my/sqrt(mx^2+my^2);

         T6 = Ra^2+Rb^2-4*Ra^2*nx^2-4*Rb^2*ny^2-4;
         H11 = (Ra*b*(a*Rb+b*Ra+2*a*Ra^2*Rb+b*Ra^3))/(a*Rb+b*Ra)^2 + nx^2*(2-
6*Ra^2+(8*Ra^2+T6)*nx^2);
         H12 = (a^2*Ra^2*Rb^2+b^2*Ra^2+a*b*Ra*Rb)/(a*Rb+b*Ra)^2 - Rb^2*nx^2-
Ra^2*ny^2+(4*Ra^2+4*Rb^2+T6)*nx^2*ny^2;
         H22 = (Rb*a*(a*Rb+b*Ra+2*b*Ra*Rb^2+a*Rb^3))/(a*Rb+b*Ra)^2 + ny^2*(2-
6*Rb^2+(8*Rb^2+T6)*ny^2);
         H14 = nx*ny*(1-3*Ra^2+(6*Ra^2+2*Rb^2+T6)*nx^2);
         H24 = nx*ny*(1-3*Rb^2+(2*Ra^2+6*Rb^2+T6)*ny^2);

         D11 = H12/2 - (t+0.5)*H11;
         D12 = H11/2 - (1/t+0.5)*H12;
         D21 = H22/2 - (t+0.5)*H12;
         D22 = H12/2 - (1/t+0.5)*H22;
         D14 = -(1+t)^2/t*H14;
         D24 = -(1+t)^2/t*H24;
         D41 = H24/2 - (t+0.5)*H14;
         D42 = H14/2 - (1/t+0.5)*H24/t;
         D44 = -(1+t)^2/t*H12; %H44 = H12;

         D = [D11 D12 D14; D21 D22 D24; D41 D42 D44];

         s=zeros(3,1);
         s=Ra*Rb*D*Eigenstress; % s1=x s2=y s3=xy

         %stress in the matrix
         SX(i,j) = sigmaX + s(1);
         SY(i,j) = sigmaY + s(2);
         TXY(i,j) = tauXY + s(3); TXY(i,j) = TXY(i,j)/2;

      elseif ((x(i)/a)^2+(y(j)/b)^2) < 1 %interior field

         SX(i,j) = EsigmaX;
         SY(i,j) = EsigmaY;
         TXY(i,j) = EtauXY/2; TXY(i,j) = TXY(i,j)/2;

      end
   end
```

```
end
%second invariant of stress
sii=(0.5.*(SX.^2+SY.^2)+(TXY).^2).^0.5;
siiE=(0.5.*(EsigmaX.^2+EsigmaY.^2)+(EtauXY).^2).^0.5;
ratio=sii/sigmaY;
figure(14) %subplot(3,1,3)
pcolor(X,Y,ratio), axis equal tight, shading interp
load('~/Documents/MATLAB/CRAMERI_color/lapaz.mat')
%invert Crameri?s colormap
sC=size(lapaz); sC=sC(1);
for i=1:sC M(i)=sC+1-i; end
M=M?; inv_c=lapaz(M,:);
colormap(inv_c)
caxis([siiE/sigmaY max(max(ratio))])
yticks([-5  0  5])
xticks([-5  0  5])
h=colorbar;
set(get(h,'label'),'string','2^n^d inv. dev. stress [MPa] / f.f. stress','FontSize',20);

set(gca,'FontSize',18)
grid on
box on

%print(gcf,'Analytical.png','-dpng','-r600')
```

Matlab script to reproduce the Stress Vs. Depth diagram for an average oceanic slab

```
% Temperature profile for a subducting plate from Frohlich 2006 "Deep
% earthquakes" (pp 41-42)

% Dry olivine dislocation creep from Hirth and Kohlstedt, 2003

% Low temperature plasticity flow laws after:
% - Hansen et al., 2019
% - Evans and Goetze, 1979
% - Kawazoe et al., 2009
% - Long et al., 2011
% - Ratteron et al., 2004
% - Demouchy et al., 2013
%-------------------------------------------------------------------------
clear all
close all

R = 8.314; % [J/K/mol] gas constant
strainrate = 1e-14; % [1/s] background strain rate

%% Pressure profile
z=0:100:66e+4; % [m] - depth
pnum=size(z,2);
rho=3300; % [kg/m^3] - density
P=rho.*z*9.81; % [Pa] - pressure
```

```
%% Temperature profile
age= 100; % [My] age of the plate
V= 100; % [mm/year] subduction velocity
phi=age*V; phi = phi*1000; % [m]
Tmant=1275+273; % [K] potential temperature of the mantle
Toc = 298; % [K] temperature of the oceanic crust
for i=1:pnum
T(i) = (erf(sqrt(0.5*z(i)/phi.*log(1+phi/z(i))))...
   - erf(sqrt(0.5*(1+z(i)/phi).*log(1+phi/z(i))))) * (Tmant-Toc) + Tmant;
end

%% Brittle failure
C=0; % [Pa] cohesion
fr_ang=30; % [∞] friction angle
S_comp = C + 2*sind(fr_ang)/(1-sind(fr_ang))*P; %Compression
S_ext = C + 2*sind(fr_ang)/(1+sind(fr_ang))*P; %Extension
S_comp_DP = P*sind(fr_ang); %Drucker-Prager

%% Olivine dislocation creep
n=3.5;
A=2.7174e-17; % [1/s/Pa^n]
Ea=532e+3; % [J/mol]
Va=1e-6; % [J/mol/Pa]

S_disl=zeros(pnum,1);
for i=1:pnum
   S_disl(i)=(strainrate/A)^(1/n)*exp((Ea+P(i)*Va)/(n*R*T(i)));
end

%% Olivine low-T plasticity

% ------- Hansen et al., 2019 -------
A=10^20.7; % [1/s]
DF=550e3; % [J/mol]
SL=3.1e9; % [Pa]
K=3.2e6; % [Pa*m^0.5]
sigma=75;
SB=1.8e9; % [Pa] max back stress
diam=0.01; % [m] grainsize

S_Hansen = zeros(pnum,1);   S_Hansen_SH = zeros(pnum,1);
for i=1:pnum
   S_Hansen(i) = (R*T(i)*(SL+K*diam^-0.5)/DF) * asinh( strainrate/A * exp(DF/R/T(i)));
   S_Hansen_SH(i) = S_Hansen(i) + SB;
end

%------- Evans and Goetze, 1979 -------
E = 5.02e5; % [J/mol/K]
A = 1.26e12; % [1/s]
q = 2;
```

```
SP = 9.1e9; % [Pa]

S_Evans = zeros(pnum,1);
for i=1:pnum
   S_Evans(i) = SP - (SP^q * R*T(i)*log(strainrate/A)/(-E) )^(1/q);
end

%------ Kawazoe et al., 2009 ------
A = 10^(12.1); % [1/s]
E = 502e3; % [J/mol]
V = 30e-6; % [m^3/mol]
SP0 = 9.1e9; % [Pa]
G = 78e9; % [Pa]
dG = 1.7;

S_Kawazoe = zeros(pnum,1);
for i=1:pnum
   SP = SP0*(1+dG*P(i)/G);
   S_kawazoe(i) = SP - sqrt(SP^2 * R*T(i)*log(strainrate/A)/(-E-P(i)*V));
end

%------- Long et al., 2011 -------
S_long = zeros(pnum,1);
for i=1:pnum
   if T(i)<= 400+273
      A = 6.75e9;
      dF = 4.58e5;
      tau = 6.7; %GPa
      p = 3/4;
      q = 3/4;
      S_long(i) = (tau^p - (tau^(p*q)*R*T(i)*log(strainrate/A)/(-dF))^(1/q) )^(1/p);
   else
      A = 1e6;
      dF = 1.48e6;
      tau = 2.8;
      % p = q = 1
      S_long(i) = tau - tau*R*T(i)*log(strainrate/A)/(-dF);
   end
end
S_long = S_long * 1e9; %Pa

%------- Ratteron et al., 2004 -------
A = 2.6e10; % [1/s]
E = 564e3; % [J/mol]
SP = 15.4e9; % [Pa]
p = 2/3;
q = 2;

S_ratteron = zeros(pnum,1);
for i=1:pnum
   if (SP^(p*q)*R*T(i)*log(strainrate/A)/(-E))^(1/q) > SP^p
```

```
        S_ratteron(i) = NaN;
    else
S_ratteron(i) = (SP^p - (SP^(p*q)*R*T(i)*log(strainrate/A)/(-E))^(1/q) )^(1/p);
    end
end

%------- Demouchy et al., 2013 -------
A = 1e6; % [1/s]
E = 450e3; % [J/mol]
SP = 15e9; % [Pa]
p = 0.5;
q = 2;
S_demouchy = zeros(pnum,1);
for i=1:pnum
S_demouchy(i) = (SP^p - (SP^(p*q)*R*T(i)*log(strainrate/A)/(-E))^(1/q) )^(1/p);
end

%% plot
figure(3)
plot(S_comp,z/1000,'b','Linewidth',1.5)
hold on
plot(S_ext,z/1000,'b--','Linewidth',1.5)
plot(S_comp_DP,z/1000,'b:','Linewidth',1.5)
%plot(S_disl,z/1000,'g--')

plot(S_Hansen,z/1000,'r','Linewidth',1.5)
plot(S_Hansen_SH,z/1000,'r--','Linewidth',1.5)
plot(S_Evans,z/1000,'k','Linewidth',1.5)
plot(S_kawazoe,z/1000,'g','Linewidth',1.5)
plot(S_long,z/1000,'k-.')
plot(S_ratteron,z/1000,'k--')
plot(S_demouchy,z/1000,'k:')

x0=10;
y0=10;
width=550*1.5;
height=400*1.5;
set(gcf,'position',[x0,y0,width,height])

legend({'compressional','extensional','DP','Hansen et al., 2019',...
    'Hansen + Strain Hardening','Evans & Goetze, 1979','Kawazoe et al., 2009',...
    'Long et al., 2010','Ratteron et al., 2004','Demouchy et al., 2013'},...
    'Location','southeast','FontSize',14)
axis ij
axis([0 10e+9 0 6.6e+2])
set(gca,'fontsize',16)
xlabel('Differential Stress [Pa]','FontSize',18)
ylabel('Depth [Km]','FontSize',18)
grid on

%print(gcf,'lithosphere_strength.png','-dpng','-r600')
```

```
%% Plot Pressure and Temperature profiles
figure(2)
yyaxis left
plot(z/1000,T-273,'b')
axis ij
axis([0 6.6e+2 0 500])
set(gca,'fontsize',12)
ylabel('Temperature [∞C]','FontSize',14)
xlabel('Depth [Km]','FontSize',14)

yyaxis right
plot(z/1000,P/(1e+9),'r')
axis ij
axis([0 6.6e+2 0 25])
set(gca,'fontsize',12)
ylabel('Pressure [GPa]','FontSize',14)
grid on
% print(gcf,'lithosphere_strength_PT.png','-dpng','-r600')
```

References:

1. Long, H., Weidner, D. J., Li, L., Chen, J., & Wang, L. (2011). Deformation of olivine at subduction zone conditions determined from in situ measurements with synchrotron radiation. *Physics of the Earth and Planetary Interiors*, *186*(1-2), 23-35.
2. Raterron, P., Wu, Y., Weidner, D. J., & Chen, J. (2004). Low-temperature olivine rheology at high pressure. *Physics of the Earth and Planetary Interiors*, *145*(1-4), 149-159.
3. Demouchy, S., Tommasi, A., Ballaran, T. B., & Cordier, P. (2013). Low strength of Earth's uppermost mantle inferred from tri-axial deformation experiments on dry olivine crystals. *Physics of the Earth and Planetary Interiors*, *220*, 37-49.
4. Crameri, F. (2018). Scientific colour maps. Zenodo. http://doi.org/10.5281/zenodo.1243862

References

1. Abers, G. A., Nakajima, J., van Keken, P. E., Kita, S., & Hacker, B. R. (2013). Thermal–petrological controls on the location of earthquakes within subducting plates. *Earth and Planetary Science Letters*, *369*, 178-187.
2. Abramson, E. H., Brown, J. M., Slutsky, L. J., & Zaug, J. (1997). The elastic constants of San Carlos olivine to 17 GPa. *Journal of Geophysical Research: Solid Earth*, *102*(B6), 12253-12263.
3. Albaric, J., Déverchère, J., Petit, C., Perrot, J., & Le Gall, B. (2009). Crustal rheology and depth distribution of earthquakes: Insights from the central and southern East African Rift System. *Tectonophysics*, *468*(1-4), 28-41.
4. Andersen, T. B., & Austrheim, H. (2006). Fossil earthquakes recorded by pseudotachylytes in mantle peridotite from the Alpine subduction complex of Corsica. *Earth and Planetary Science Letters*, *242*(1-2), 58-72.
5. Anderson, P.M., Hirth, J.P., and Lothe, J., 2017, The- ory of Dislocations (third edition): New York, Cambridge University Press, 718 p.
6. Angiboust, S., Agard, P., Yamato, P., & Raimbourg, H. (2012). Eclogite breccias in a subducted ophiolite: A record of intermediate-depth earthquakes?. *Geology*, *40*(8), 707-710.
7. Austrheim, H., & Boundy, T. M. (1994). Pseudotachylytes generated during seismic faulting and eclogitization of the deep crust. *Science*, *265*(5168), 82-83.
8. Austrheim, H., Dunkel, K. G., Plümper, O., Ildefonse, B., Liu, Y., & Jamtveit, B. (2017). Fragmentation of wall rock garnets during deep crustal earthquakes. *Science Advances*, *3*(2), e1602067.
9. Babuška, V., Fiala, J., Kumazawa, M., Ohno, I., & Sumino, Y. (1978). Elastic properties of garnet solid-solution series. *Physics of the Earth and Planetary Interiors*, *16*(2), 157-176.
10. Bailey, G. N., Reynolds, S. C., & King, G. C. (2011). Landscapes of human evolution: models and methods of tectonic geomorphology and the reconstruction of hominin landscapes. *Journal of human evolution*, *60*(3), 257-280.
11. Beall, A., Fagereng, Å., & Ellis, S. (2019). Strength of strained two-phase mixtures: Application to rapid creep and stress amplification in subduction zone Mélange. *Geophysical Research Letters*, *46*(1), 169-178.
12. Bell, T. H. (1978), Progressive deformation and reorientation of fold axes in a ductile mylonite zone: The Woodroffe Thrust, Tectonophysics, 44(1–4), 285–320, doi:10.1016/0040-1951(78)90074-4.
13. Bestmann, M., Pennacchioni, G., Nielsen, S., Göken, M., & De Wall, H. (2012). Deformation and ultrafine dynamic recrystallization of quartz in pseudotachylyte-bearing brittle faults: A matter of a few seconds. *Journal of Structural Geology*, *38*, 21-38.
14. Bezacier, L., Reynard, B., Bass, J. D., Sanchez-Valle, C., & Van de Moortèle, B. (2010). Elasticity of antigorite, seismic detection of serpentinites, and anisotropy in subduction zones. *Earth and Planetary Science Letters*, *289*(1-2), 198-208.
15. Bodin, P., & Horton, S. (2004). Source parameters and tectonic implications of aftershocks of the M w 7.6 Bhuj earthquake of 26 January 2001. *Bulletin of the Seismological Society of America*, *94*(3), 818-827.
16. Boneh, Y., Schottenfels, E., Kwong, K., Van Zelst, I., Tong, X., Eimer, M., ... & Billen, M. (2019). Intermediate-depth earthquakes controlled by incoming plate hydration along bending-related faults. *Geophysical Research Letters*, *46*(7), 3688-3697.
17. Bonnet, E., Bour, O., Odling, N. E., Davy, P., Main, I., Cowie, P., & Berkowitz, B. (2001). Scaling of fracture systems in geological media. *Reviews of geophysics*, *39*(3), 347-383.
18. Britton, T. B., & Wilkinson, A. J. (2011). Measurement of residual elastic strain and lattice rotations with high resolution electron backscatter diffraction. *Ultramicroscopy*, *111*(8), 1395-1404.
19. Britton, T. B., & Wilkinson, A. J. (2012). High resolution electron backscatter diffraction measurements of elastic strain variations in the presence of larger lattice rotations. *Ultramicroscopy*, *114*, 82-95.
20. Brückner, L. M., & Trepmann, C. A. (2021). Stresses during pseudotachylyte formation-Evidence from deformed amphibole and quartz in fault rocks from the Silvretta basal thrust (Austria). *Tectonophysics*, *817*, 229046.
21. Brudzinski, M. R., Thurber, C. H., Hacker, B. R., & Engdahl, E. R. (2007). Global prevalence of double Benioff zones. *Science*, *316*(5830), 1472-1474.
22. Burov, E. B. (2011). Rheology and strength of the lithosphere. *Marine and petroleum Geology*, *28*(8), 1402-1443.
23. Burov, E. B., & Diament, M. (1995). The effective elastic thickness (T e) of continental lithosphere: What does it really mean?. *Journal of Geophysical Research: Solid Earth*, *100*(B3), 3905-3927.
24. Burov, E. B., & Watts, A. B. (2006). The long-term strength of continental lithosphere:" jelly sandwich" or" crème brûlée"?. *GSA today*, *16*(1), 4.

25. Camacho, A., & Fanning, C. M. (1995). Some isotopic constraints on the evolution of the granulite and upper amphibolite facies terranes in the eastern Musgrave Block, central Australia. *Precambrian Research*, *71*(1-4), 155-181.
26. Camacho, A., & McDougall, I. (2000). Intracratonic, strike-slip partitioned transpression and the formation and exhumation of eclogite facies rocks: An example from the Musgrave Block, central Australia. *Tectonics*, *19*(5), 978-996.
27. Camacho, A., McDougall, I., Armstrong, R., & Braun, J. (2001). Evidence for shear heating, Musgrave Block, central Australia. *Journal of Structural Geology*, *23*(6-7), 1007-1013.
28. Camacho, A., Vernon, R. H., & Gerald, J. F. (1995). Large volumes of anhydrous pseudotachylyte in the Woodroffe Thrust, eastern Musgrave Ranges, Australia. *Journal of Structural Geology*, *17*(3), 371-383.
29. Camacho, A., W. Compston, M. McCulloch, and I. McDougall (1997), Timing and exhumation of eclogite facies shear zones, Musgrave Block, central Australia, J. Metamorph. Geol., 15(6), 735–751
30. Campbell, L. R., & Menegon, L. (2022). High Stress Deformation and Short-Term Thermal Pulse Preserved in Pyroxene Microstructures From Exhumed Lower Crustal Seismogenic Faults (Lofoten, Norway). *Journal of Geophysical Research: Solid Earth*, *127*(7), e2021JB023616.
31. Campbell, L. R., Menegon, L., Fagereng, Å., & Pennacchioni, G. (2020). Earthquake nucleation in the lower crust by local stress amplification. *Nature communications*, *11*(1), 1322.
32. Cesare, B., Marchesi, C., Hermann, J., & Gómez-Pugnaire, M. T. (2003). Primary melt inclusions in andalusite from anatectic graphitic metapelites: implications for the position of the Al2SiO5 triple point. *Geology*, *31*(7), 573-576.
33. Chernak, L. J., & Hirth, G. (2011). Syndeformational antigorite dehydration produces stable fault slip. *Geology*, *39*(9), 847-850.
34. Chester, J. S., Chester, F. M., & Kronenberg, A. K. (2005). Fracture surface energy of the Punchbowl fault, San Andreas system. *Nature*, *437*(7055), 133-136.
35. Clarke, G. L., I. S. Buick, A. Y. Glikson, and A. J. Stewart (1995), Structural and pressure-temperature evolution of host rocks of the Giles Complex, western Musgrave Block, central Australia: Evidence for multiple high-pressure events, AGSO J. Aust. Geol. Geophys., 16(1/2), 127–146.
36. Cocco, M., Aretusini, S., Cornelio, C., Nielsen, S. B., Spagnuolo, E., Tinti, E., & Di Toro, G. (2023). Fracture Energy and Breakdown Work During Earthquakes. *Annual Review of Earth and Planetary Sciences*, *51*.
37. Dal Zilio, L., & Ampuero, J. P. (2023). Earthquake doublet in Turkey and Syria. *Communications Earth & Environment*, *4*(1), 71.
38. de Gromard, R. Q., Kirkland, C. L., Howard, H. M., Wingate, M. T., Jourdan, F., McInnes, B. I., ... & Smithies, R. H. (2019). When will it end? Long-lived intracontinental reactivation in central Australia. *Geoscience Frontiers*, *10*(1), 149-164.
39. Deichmann, N., & Rybach, L. (1989). Earthquakes and temperatures in the lower crust below the northern Alpine foreland of Switzerland. *Properties and processes of earth's lower crust*, *51*, 197-213.
40. Di Toro, G., & Pennacchioni, G. (2004). Superheated friction-induced melts in zoned pseudotachylytes within the Adamello tonalites (Italian Southern Alps). *Journal of Structural Geology*, *26*(10), 1783-1801.
41. Di Toro, G., Hirose, T., Nielsen, S., Pennacchioni, G., & Shimamoto, T. (2006). Natural and experimental evidence of melt lubrication of faults during earthquakes. *science*, *311*(5761), 647-649.
42. Di Toro, G., Nielsen, S., & Pennacchioni, G. (2005). Earthquake rupture dynamics frozen in exhumed ancient faults. *Nature*, *436*(7053), 1009-1012.
43. Di Toro, G., Pennacchioni, G., & Teza, G. (2005). Can pseudotachylytes be used to infer earthquake source parameters? An example of limitations in the study of exhumed faults. *Tectonophysics*, *402*(1-4), 3-20.
44. Doan, M. L., & Gary, G. (2009). Rock pulverization at high strain rate near the San Andreas fault. *Nature Geoscience*, *2*(10), 709-712.
45. Druiventak, A., Matysiak, A., Renner, J., & Trepmann, C. A. (2012). Kick-and-cook experiments on peridotite: simulating coseismic deformation and post-seismic creep. *Terra Nova*, *24*(1), 62-69.
46. Edgoose, C. J., Camacho, A., Wakelin-King, G. A., & Simons, B. A. (1993). Kulgera, Northern Territory. 1: 250000 Geological sheet and explanatory notes. Northern Territory Geological Survey, Darwin, Australia.
47. Edgoose, C. J., I. R. Scrimgeour, and D. F. Close (2004), Report 15: Geology of the Musgrave Block, Northern Territory, North. Territ. Geol. Surv., Darwin.
48. Ellis, D. J., and M. A. H. Maboko (1992), Precambrian tectonics and the physicochemical evolution of the continental crust. I. The gabbro-eclogite transition revisited, Precambrian Res., 55(1–4), 491–506, doi:10.1016/0301-9268(92)90041-L.

49. Ellis, S., & Stöckhert, B. (2004). Elevated stresses and creep rates beneath the brittle-ductile transition caused by seismic faulting in the upper crust. *Journal of Geophysical Research: Solid Earth*, *109*(B5).
50. Engdahl, E. R., & Scholz, C. H. (1977). A double Benioff zone beneath the central Aleutians: An unbending of the lithosphere. *Geophysical Research Letters*, *4*(10), 473-476.
51. England, P., & Jackson, J. (2011). Uncharted seismic risk. *Nature Geoscience*, *4*(6), 348-349.
52. Eshelby, J. D. (1957). The determination of the elastic field of an ellipsoidal inclusion, and related problems. Proceedings of the royal society of London. Series A. Mathematical and physical sciences, 241(1226), 376-396.
53. Evans, B., & Goetze, C. (1979). The temperature variation of hardness of olivine and its implication for polycrystalline yield stress. *Journal of Geophysical Research: Solid Earth*, *84*(B10), 5505-5524.
54. Fabbri, O., Magott, R., Fournier, M., & Etienne, L. (2018). Pseudotachylyte in the Monte Maggiore ophiolitic unit (Alpine Corsica): a possible lateral extension of the Cima di Gratera intermediate-depth Wadati-Benioff paleo-seismic zone. *BSGF-Earth Sciences Bulletin*, *189*(4-6), 18.
55. Faccenda, M. (2014). Water in the slab: A trilogy. *Tectonophysics*, *614*, 1-30.
56. Faccenda, M., Gerya, T. V., & Burlini, L. (2009). Deep slab hydration induced by bending-related variations in tectonic pressure. *Nature Geoscience*, *2*(11), 790-793.
57. Faccenda, M., Gerya, T. V., Mancktelow, N. S., & Moresi, L. (2012). Fluid flow during slab unbending and dehydration: Implications for intermediate-depth seismicity, slab weakening and deep water recycling. *Geochemistry, Geophysics, Geosystems*, *13*(1).
58. Ferrand, T. P. (2019). Seismicity and mineral destabilizations in the subducting mantle up to 6 GPa, 200 km depth. *Lithos*, *334*, 205-230.
59. Ferrand, T. P. & Manea, E. F. (2021). Dehydration-induced earthquakes identified in a subducted oceanic slab beneath Vrancea, Romania. *Scientific Reports,* 11(1), 1-9.
60. Ferrand, T. P., Hilairet, N., Incel, S., Deldicque, D., Labrousse, L., Gasc, J., ... & Schubnel, A. (2017). Dehydration-driven stress transfer triggers intermediate-depth earthquakes. *Nature communications*, *8*(1), 1-11.
61. Ferrand, T. P., Nielsen, S., Labrousse, L., & Schubnel, A. (2021). Scaling seismic fault thickness from the laboratory to the field. *Journal of Geophysical Research: Solid Earth*, *126*(3), e2020JB020694.
62. Florez, M. A., & Prieto, G. A. (2019). Controlling factors of seismicity and geometry in double seismic zones. *Geophysical Research Letters*, *46*(8), 4174-4181.
63. Fondriest, M., Mecklenburgh, J., Passelegue, F. X., Artioli, G., Nestola, F., Spagnuolo, E., ... & Di Toro, G. (2020). Pseudotachylyte alteration and the rapid fade of earthquake scars from the geological record. *Geophysical Research Letters*, *47*(22), e2020GL090020.
64. Freund, L. B. (1998). *Dynamic fracture mechanics*. Cambridge university press.
65. Frohlich C. 2006. *Deep Earthquakes*. Cambridge, UK: Cambridge Univ. Press
66. Gerya, T., 2019. Introduction to numerical geodynamic modelling. Second edition. Cambridge University Press, Cambridge
67. Gilio, M., Scambelluri, M., Agostini, S., Godard, M., Peters, D., & Pettke, T. (2019). Petrology and geochemistry of serpentinites associated with the ultra-high pressure Lago di Cignana Unit (Italian Western Alps). *Journal of petrology*, *60*(6), 1229-1262.
68. Gray, C. M. (1978), Geochronology of granulite-facies gneisses in the western Musgrave Block, central Australia, J. Geol. Soc. Aust., 25(7), 403–414, doi:10.1080/00167617808729050.
69. Groma, I. & Bakó, B. Probability distribution of internal stresses in parallel straight dislocation systems. Phys. Rev. B 58, 2969–2974 (1998).
70. Hacker, B. R., Peacock, S. M., Abers, G. A., & Holloway, S. D. (2003) Subduction factory 2. Are intermediate-depth earthquakes in subducting slabs linked to metamorphic dehydration reactions?. Journal of Geophysical Research: Solid Earth, 108(B1)
71. Hansen, L. N., Kumamoto, K. M., Thom, C. A., Wallis, D., Durham, W. B., Goldsby, D. L., ... & Kohlstedt, D. L. (2019). Low-temperature plasticity in olivine: Grain size, strain hardening, and the strength of the lithosphere. *Journal of Geophysical Research: Solid Earth*, *124*(6), 5427-5449.
72. Hasegawa, A., & Nakajima, J. (2017). Seismic imaging of slab metamorphism and genesis of intermediate-depth intraslab earthquakes. *Progress in Earth and Planetary Science*, *4*(1), 12.
73. Hawemann, F., Mancktelow, N. S., Pennacchioni, G., Wex, S., & Camacho, A. (2019). Weak and slow, strong and fast: How shear zones evolve in a dry continental crust (Musgrave Ranges, Central Australia). *Journal of Geophysical Research: Solid Earth*, *124*(1), 219-240.
74. Hawemann, F., Mancktelow, N. S., Wex, S., Camacho, A., & Pennacchioni, G. (2018). Pseudotachylyte as field evidence for lower-crustal earthquakes during the intracontinental Petermann Orogeny (Musgrave Block, Central Australia). *Solid Earth*, *9*(3), 629-648.

75. Hawemann, F., Mancktelow, N., Wex, S., Pennacchioni, G., & Camacho, A. (2019). Fracturing and crystal plastic behaviour of garnet under seismic stress in the dry lower continental crust (Musgrave Ranges, Central Australia). *Solid Earth*, *10*(5), 1635-1649.
76. Heuberger, H., Masch, L., Preuss, E., & Schröcker, A. (1984). Quaternary landslides and rock fusion in Central Nepal and in the Tyrolean Alps. *Mountain Research and Development*, 345-362.
77. Hielscher, R., & Schaeben, H. (2008). A novel pole figure inversion method: specification of the MTEX algorithm. *Journal of Applied Crystallography*, *41*(6), 1024-1037.
78. Hilairet, N., Reynard, B., Wang, Y., Daniel, I., Merkel, S., Nishiyama, N., & Petitgirard, S. (2007). High-pressure creep of serpentine, interseismic deformation, and initiation of subduction. *Science*, *318*(5858), 1910-1913.
79. Hirth, G., & Kohlstedt, D. (2003). Rheology of the upper mantle and the mantle wedge: A view from the experimentalists. Geophys. Monogr. Inside Subduct: Fact., 138, pp. 83-105
80. Holdaway, M. J., & Lee, S. M. (1977). Fe-Mg cordierite stability in high-grade pelitic rocks based on experimental, theoretical, and natural observations. *Contributions to Mineralogy and Petrology*, *63*(2), 175-198.
81. Holland, T. J. B., & Powell, R. T. J. B. (1998). An internally consistent thermodynamic data set for phases of petrological interest. *Journal of metamorphic Geology*, *16*(3), 309-343.
82. Houston H. 2015. Deep earthquakes. In *Treatise on Geophysics*, ed. G Schubert, pp. 329–54. Amsterdam: Elsevier
83. Incel, S., Labrousse, L., Hilairet, N., John, T., Gasc, J., Shi, F., ... & Schubnel, A. (2019). Reaction-induced embrittlement of the lower continental crust. *Geology*, *47*(3), 235-238.
84. Incel, S., Schubnel, A., Renner, J., John, T., Labrousse, L., Hilairet, N., ... & Jamtveit, B. (2019). Experimental evidence for wall-rock pulverization during dynamic rupture at ultra-high pressure conditions. *Earth and Planetary Science Letters*, *528*, 115832.
85. Jackson, J. (2002). Faulting, flow, and the strength of the continental lithosphere. *International Geology Review*, *44*(1), 39-61.
86. Jackson, J. A., Austrheim, H., McKenzie, D., & Priestley, K. (2004). Metastability, mechanical strength, and the support of mountain belts. *Geology*, *32*(7), 625-628.
87. Jackson, J., McKenzie, D., & Priestley, K. (2021). Relations between earthquake distributions, geological history, tectonics and rheology on the continents. *Philosophical Transactions of the Royal Society A*, *379*(2193), 20190412.
88. Jacobsen, S. D. (2006). Effect of water on the equation of state of nominally anhydrous minerals. *Reviews in mineralogy and geochemistry*, *62*(1), 321-342.
89. Jain, C., Korenaga, J., & Karato, S. I. (2017). On the yield strength of oceanic lithosphere. *Geophysical Research Letters*, *44*(19), 9716-9722.
90. Jamtveit, B., Ben-Zion, Y., Renard, F., & Austrheim, H. (2018). Earthquake-induced transformation of the lower crust. *Nature*, *556*(7702), 487-491.
91. Jamtveit, B., Petley-Ragan, A., Incel, S., Dunkel, K. G., Aupart, C., Austrheim, H., ... & Renard, F. (2019). The effects of earthquakes and fluids on the metamorphism of the lower continental crust. *Journal of Geophysical Research: Solid Earth*, *124*(8), 7725-7755.
92. John, T., & Schenk, V. (2006). Interrelations between intermediate-depth earthquakes and fluid flow within subducting oceanic plates: Constraints from eclogite facies pseudotachylytes. *Geology*, *34*(7), 557-560.
93. John, T., Medvedev, S., Rüpke, L. H., Andersen, T. B., Podladchikov, Y. Y., & Austrheim, H. (2009). Generation of intermediate-depth earthquakes by self-localizing thermal runaway. *Nature Geoscience*, *2*(2), 137-140.
94. Johnson, S. E., Song, W. J., Vel, S. S., Song, B. R., & Gerbi, C. C. (2021). Energy partitioning, dynamic fragmentation, and off-fault damage in the earthquake source volume. *Journal of Geophysical Research: Solid Earth*, *126*(11), e2021JB022616.
95. Kameyama, M., Yuen, D. A., & Karato, S. I. (1999). Thermal-mechanical effects of low-temperature plasticity (the Peierls mechanism) on the deformation of a viscoelastic shear zone. *Earth and Planetary Science Letters*, *168*(1-2), 159-172.
96. Kaus, B. J., Mühlhaus, H., & May, D. A., 2010. A stabilization algorithm for geodynamic numerical simulations with a free surface. Physics of the Earth and Planetary Interiors 181(1-2), 12-20.
97. Kaus, B., Popov, A. A., Baumann, T., Pusok, A., Bauville, A., Fernandez, N., & Collignon, M., 2016. Forward and inverse modelling of lithospheric deformation on geological timescales. *Proceedings of NIC Symposium*.
98. Kawazoe, T., Karato, S. I., Otsuka, K., Jing, Z., & Mookherjee, M. (2009). Shear deformation of dry polycrystalline olivine under deep upper mantle conditions using a rotational Drickamer apparatus (RDA). *Physics of the Earth and Planetary Interiors*, *174*(1-4), 128-137.

99. Kelemen, P. B., & Hirth, G. (2007). A periodic shear-heating mechanism for intermediate-depth earthquakes in the mantle. *Nature*, *446*(7137), 787-790.
100. Kirby, E., & Whipple, K. X. (2012). Expression of active tectonics in erosional landscapes. *Journal of structural geology*, *44*, 54-75.
101. Kirkpatrick, J. D., & Rowe, C. D. (2013). Disappearing ink: How pseudotachylytes are lost from the rock record. *Journal of Structural Geology*, *52*, 183-198.
102. Kita, S., & Ferrand, T. P. (2018). Physical mechanisms of oceanic mantle earthquakes: Comparison of natural and experimental events. *Scientific reports*, *8*(1), 1-11.
103. Kocks, U. F., & Mecking, H. (2003). Physics and phenomenology of strain hardening: the FCC case. *Progress in materials science*, *48*(3), 171-273.
104. Lallemand, S., Heuret, A., Faccenna, C., & Funiciello, F. (2008). Subduction dynamics as revealed by trench migration. *Tectonics*, *27*(3).
105. Lin, A. (1994). Microlite morphology and chemistry in pseudotachylite, from the Fuyun fault zone, China. *The Journal of Geology*, *102*(3), 317-329.
106. Lin, A. (2008). Seismic slip in the lower crust inferred from granulite-related pseudotachylyte in the Woodroffe thrust, Central Australia. *Pure and Applied Geophysics*, *165*, 215-233.
107. Lin, A., Maruyama, T., Aaron, S., Michibayashi, K., Camacho, A., & Kano, K. I. (2005). Propagation of seismic slip from brittle to ductile crust: Evidence from pseudotachylyte of the Woodroffe thrust, central Australia. *Tectonophysics*, *402*(1-4), 21-35.
108. Lockner, D. A., & Okubo, P. G. (1983). Measurements of frictional heating in granite. *Journal of Geophysical Research: Solid Earth*, *88*(B5), 4313-4320.
109. Lofgren, G. (1974). An experimental study of plagioclase crystal morphology; isothermal crystallization. *American journal of Science*, *274*(3), 243-273.
110. Ma, K. F., Tanaka, H., Song, S. R., Wang, C. Y., Hung, J. H., Tsai, Y. B., ... & Wu, H. Y. (2006). Slip zone and energetics of a large earthquake from the Taiwan Chelungpu-fault Drilling Project. *Nature*, *444*(7118), 473-476.
111. Maboko, M. A. H., I. McDougall, and P. K. Zeitler (1989), Metamorphic P-T path of granulites in the Musgrave Ranges, central Australia, in Evolution of Metamorphic Belts, edited by J. S. Daly, R. A. Cliff, and B. W. D. Yardley, Geol. Soc. London Spec. Publ., 43, pp. 303–307.
112. Maboko, M. A. H., I. McDougall, P. K. Zeitler, and I. S. Williams (1992), Geochronological evidence for ~ 530–550 Ma juxtaposition of two Proterozoic metamorphic terranes in the Musgrave Ranges, central Australia, Aust. J. Earth Sci., 39(4), 457–471, doi:10.1080/08120099208728038.
113. Maboko, M. A. H., I. S. Williams, and W. Compston (1991), Zircon U-Pb chronometry of the pressure and temperature history of granulites in the Musgrave Ranges, Central Australia, J. Geol., 99(5), 675–697.
114. Maggi, A., Jackson, J. A., Mckenzie, D., & Priestley, K. (2000). Earthquake focal depths, effective elastic thickness, and the strength of the continental lithosphere. *Geology*, *28*(6), 495-498.
115. Magloughlin, J. F. (2005). Immiscible sulfide droplets in pseudotachylyte: Evidence for high temperature (> 1200 C) melts. *Tectonophysics*, *402*(1-4), 81-91.
116. Major, R. B. (1970), Woodroffe Thrust zone in the Musgrave Ranges, Q. Geol. Notes issued by Geol. Surv. South Aust., 35, 9–11.
117. Major, R. B., & Conor, C. H. H. (1993). Musgrave block. *The Geology of South Australia*, *1*, 156-167.
118. Mancktelow, N. S., Camacho, A., & Pennacchioni, G. (2022). Time-Lapse Record of an Earthquake in the Dry Felsic Lower Continental Crust Preserved in a Pseudotachylyte-Bearing Fault. *Journal of Geophysical Research: Solid Earth*, *127*(4), e2021JB022878.
119. McKenzie, D., & Brune, J. N. (1972). Melting on fault planes during large earthquakes. *Geophysical Journal International*, *29*(1), 65-78.
120. Meagher, E. P. (1980). Silicate garnets. *Reviews in Mineralogy and Geochemistry*, *5*(1), 25-66.
121. Menant, A., Angiboust, S., Monié, P., Oncken, O., & Guigner, J. M. (2018). Brittle deformation during Alpine basal accretion and the origin of seismicity nests above the subduction interface. *Earth and Planetary Science Letters*, *487*, 84-93.
122. Menegon, L., Campbell, L., Mancktelow, N., Camacho, A., Wex, S., Papa, S., ... & Pennacchioni, G. (2021). The earthquake cycle in the dry lower continental crust: insights from two deeply exhumed terranes (Musgrave Ranges, Australia and Lofoten, Norway). *Philosophical transactions of the Royal Society A*, *379*(2193), 20190416.
123. Menegon, L., Pennacchioni, G., Malaspina, N., Harris, K., & Wood, E. (2017). Earthquakes as precursors of ductile shear zones in the dry and strong lower crust. *Geochemistry, Geophysics, Geosystems*, *18*(12), 4356-4374.

124. Mikami, Y., Oda, K., Kamaya, M., & Mochizuki, M. (2015). Effect of reference point selection on microscopic stress measurement using EBSD. *Materials Science and Engineering: A*, *647*, 256-264.
125. Mitchell, T. M., Ben-Zion, Y., & Shimamoto, T. (2011). Pulverized fault rocks and damage asymmetry along the Arima-Takatsuki Tectonic Line, Japan. *Earth and Planetary Science Letters*, *308*(3-4), 284-297.
126. Moecher, D. P., & Steltenpohl, M. G. (2009). Direct calculation of rupture depth for an exhumed paleoseismogenic fault from mylonitic pseudotachylyte. *Geology*, *37*(11), 999-1002.
127. Myers, J. S., R. D. Shaw, and I. M. Tyler (1996), Tectonic evolution of Proterozoic Australia, Tectonics, 15(6), 1431–1446, doi:10.1029/96TC02356.
128. Newton, R. C., & Wood, B. J. (1979). Thermodynamics of water in cordierite and some petrologic consequences of cordierite as a hydrous phase. *Contributions to Mineralogy and Petrology*, *68*(4), 391-405.
129. Okubo, K., Bhat, H. S., Rougier, E., Marty, S., Schubnel, A., Lei, Z., ... & Klinger, Y. (2019). Dynamics, radiation, and overall energy budget of earthquake rupture with coseismic off-fault damage. *Journal of Geophysical Research: Solid Earth*, *124*(11), 11771-11801.
130. Orlandini, O. F., Mahan, K. H., Williams, M. J., Regan, S. P., & Mueller, K. J. (2019). Evidence for deep crustal seismic rupture in a granulite-facies, intraplate, strike-slip shear zone, northern Saskatchewan, Canada. *Bulletin*, *131*(3-4), 403-425.
131. Papa, S., Pennacchioni, G., Angel, R. J., & Faccenda, M. (2018). The fate of garnet during (deep-seated) coseismic frictional heating: The role of thermal shock. *Geology*, *46*(5), 471-474.
132. Papa, S., Pennacchioni, G., Menegon, L., & Thielmann, M. (2020). High-stress creep preceding coseismic rupturing in amphibolite-facies ultramylonites. *Earth and Planetary Science Letters*, *541*, 116260.
133. Passchier, C. W. (1982). Pseudotachylyte and the development of ultramylonite bands in the Saint-Barthelemy Massif, French Pyrenees. *Journal of Structural Geology*, *4*(1), 69-79.
134. Pattison, D. R. (1992). Stability of andalusite and sillimanite and the Al2SiO5 triple point: constraints from the Ballachulish aureole, Scotland. *The Journal of Geology*, *100*(4), 423-446.
135. Pennacchioni, G., Scambelluri, M., Bestmann, M., Notini, L., Nimis, P., Plümper, O., ... & Nestola, F. (2020). Record of intermediate-depth subduction seismicity in a dry slab from an exhumed ophiolite. *Earth and Planetary Science Letters*, *548*, 116490.
136. Petley-Ragan, A., Ben-Zion, Y., Austrheim, H., Ildefonse, B., Renard, F., & Jamtveit, B. (2019). Dynamic earthquake rupture in the lower crust. *Science Advances*, *5*(7), eaaw0913.
137. Petley-Ragan, A., Dunkel, K. G., Austrheim, H., Ildefonse, B., & Jamtveit, B. (2018). Microstructural records of earthquakes in the lower crust and associated fluid-driven metamorphism in plagioclase-rich granulites. *Journal of Geophysical Research: Solid Earth*, *123*(5), 3729-3746.
138. Phillips, N. J., & Ji, S. (2021). Constraining the ductile deformation mechanisms of garnet across pressure-temperature space. *Journal of Structural Geology*, *148*, 104356.
139. Philpotts, A. R. (1964). Origin of pseudotachylites. *American Journal of Science*, *262*(8), 1008-1035.
140. Pittarello, L., Di Toro, G., Bizzarri, A., Pennacchioni, G., Hadizadeh, J., & Cocco, M. (2008). Energy partitioning during seismic slip in pseudotachylyte-bearing faults (Gole Larghe Fault, Adamello, Italy). *Earth and Planetary Science Letters*, *269*(1-2), 131-139.
141. Pittarello, L., Habler, G., Abart, R., & Rhede, D. (2015). Garnet growth in frictional melts of the Ivrea Zone (Italy). *Italian Journal of Geosciences*, *134*(1), 149-161.
142. Pittarello, L., Pennacchioni, G., & Di Toro, G. (2012). Amphibolite-facies pseudotachylytes in Premosello metagabbro and felsic mylonites (Ivrea Zone, Italy). *Tectonophysics*, *580*, 43-57.
143. Plümper, O., John, T., Podladchikov, Y. Y., Vrijmoed, J. C., & Scambelluri, M. (2017). Fluid escape from subduction zones controlled by channel-forming reactive porosity. *Nature Geoscience*, *10*(2), 150-156.
144. Popov, A.A., Sobolev, S.V., Zoback, M.D., 2012. Modeling evolution of the San Andreas Fault system in northern and central California. Geochemistry, Geophysics, Geosystems 13.
145. Prieto, G. A., Florez, M., Barrett, S. A., Beroza, G. C., Pedraza, P., Blanco, J. F., & Poveda, E. (2013). Seismic evidence for thermal runaway during intermediate-depth earthquake rupture. *Geophysical Research Letters*, *40*(23), 6064-6068.
146. Prieto, G. A., Froment, B., Yu, C., Poli, P., & Abercrombie, R. (2017). Earthquake rupture below the brittle-ductile transition in continental lithospheric mantle. *Science Advances*, *3*(3), e1602642.
147. Raimondo, T., Collins, A. S., Hand, M., Walker-Hallam, A., Smithies, R. H., Evins, P. M., & Howard, H. M. (2010). The anatomy of a deep intracontinental orogen. *Tectonics*, *29*(4).
148. Raleigh, C. B., & Paterson, M. S. (1965). Experimental deformation of serpentinite and its tectonic implications. *Journal of Geophysical Research*, *70*(16), 3965-3985.

149. Raleigh, C. B., & Paterson, M. S. (1965). Experimental deformation of serpentinite and its tectonic implications. *Journal of Geophysical Research*, *70*(16), 3965-3985.
150. Ranalli, G. (1995). *Rheology of the Earth*. Springer Science & Business Media.
151. Reches, Z. E., & Dewers, T. A. (2005). Gouge formation by dynamic pulverization during earthquake rupture. *Earth and Planetary Science Letters*, *235*(1-2), 361-374.
152. Reynard, B., Nakajima, J. & Kawakatsu, H. (2010). Earthquakes and plastic deformation of anhydrous slab mantle in double Wadati-Benioff zones. *Geophysical Research Letters,* **37**(24).
153. Scambelluri, M., Pennacchioni, G., Gilio, M., Bestmann, M., Plümper, O., & Nestola, F. (2017). Fossil intermediate-depth earthquakes in subducting slabs linked to differential stress release. *Nature Geoscience*, *10*(12), 960-966.
154. Scholz, C. H. (2019). *The mechanics of earthquakes and faulting*. Cambridge university press.
155. Scrimgeour, I. R., D. F. Close, and C. J. Edgoose (1999), 1:250,000 Geological Map Series and Explanatory Notes. Petermann Ranges SG52-7, 2nd ed., North. Territ. Geol. Surv., Darwin.
156. Scrimgeour, I., and D. Close (1999), Regional high-pressure metamorphism during intracratonic deformation: The Petermann Orogeny, central Australia, J. Metamorph. Geol., 17(5), 557–572, doi:10.1046/j.1525-1314.1999.00217.x.
157. Shand, S. J. (1916). The pseudotachylyte of Parijs (Orange free State), and its relation to 'Trap-Shotten Gneiss' and 'Flinty Crush-rock'. *Quarterly Journal of the Geological Society*, *72*(1-4), 198-221.
158. Shi, F., Wang, Y., Yu, T., Zhu, L., Zhang, J., Wen, J., ... & Jin, Z. (2018). Lower-crustal earthquakes in southern Tibet are linked to eclogitization of dry metastable granulite. *Nature Communications*, *9*(1), 3483.
159. Shillington, D. J., Bécel, A., Nedimović, M. R., Kuehn, H., Webb, S. C., Abers, G. A., ... & Mattei-Salicrup, G. A. (2015). Link between plate fabric, hydration and subduction zone seismicity in Alaska. *Nature Geoscience*, *8*(12), 961-964.
160. Sibson, R. H. (1975). Generation of pseudotachylyte by ancient seismic faulting. *Geophysical Journal International*, *43*(3), 775-794.
161. Sibson, R. H. (1977). Fault rocks and fault mechanisms. *Journal of the Geological Society*, *133*(3), 191-213.
162. Singer, J., Diehl, T., Husen, S., Kissling, E., & Duretz, T. (2014). Alpine lithosphere slab rollback causing lower crustal seismicity in northern foreland. *Earth and Planetary Science Letters*, *397*, 42-56.
163. Smithies, R. H., H. M. Howard, P. M. Evins, C. L. Kirkland, D. E. Kelsey, M. Hand, M. T. D. Wingate, A. S. Collins, and E. Belousova (2011), High-temperature granite magmatism, crust-mantle interaction and the Mesoproterozoic intracontinental evolution of the Musgrave Province, Central Australia, J. Petrol., 52(5), 931–958, doi:10.1093/petrology/egr010.
164. Spray, J. G. (2010). Frictional melting processes in planetary materials: From hypervelocity impact to earthquakes. *Annual Review of Earth and Planetary Sciences*, *38*, 221-254.
165. Stewart, C. A., & Miranda, E. A. (2017). The rheological evolution of brittle-ductile transition rocks during the earthquake cycle: Evidence for a ductile precursor to pseudotachylyte in an extensional fault system, South Mountains, Arizona. *Journal of Geophysical Research: Solid Earth*, *122*(12), 10-643.
166. Swanson, M. T. (1992). Fault structure, wear mechanisms and rupture processes in pseudotachylyte generation. *Tectonophysics*, *204*(3-4), 223-242.
167. Thielmann, M., Rozel, A., Kaus, B. J. P., & Ricard, Y. (2015). Intermediate-depth earthquake generation and shear zone formation caused by grain size reduction and shear heating. *Geology*, *43*(9), 791-794.
168. Thompson, A. B., & Connolly, J. A. (1995). Melting of the continental crust: some thermal and petrological constraints on anatexis in continental collision zones and other tectonic settings. *Journal of Geophysical Research: Solid Earth*, *100*(B8), 15565-15579.
169. Toffol, G., Pennacchioni, G., Camacho, A., & Mancktelow, N. (2022). *Geometric complexity of the Woodroffe Thrust (Musgrave Ranges, central Australia) recorded in hanging wall Al-silicate-bearing peraluminous gneisses and hosted pseudotachylytes* (No. EGU22-8678). Copernicus Meetings.
170. Toffol, G., Yang, J., Pennacchioni, G., Faccenda, M., & Scambelluri, M. (2022). How to quake a subducting dry slab at intermediate depths: Inferences from numerical modelling. *Earth and Planetary Science Letters*, *578*, 117289.
171. Trepmann, C. A., & Stöckhert, B. (2013). Short-wavelength undulatory extinction in quartz recording coseismic deformation in the middle crust–an experimental study. *Solid Earth*, *4*(2), 263-276.
172. Trepmann, C. A., Hsu, C., Hentschel, F., Döhler, K., Schneider, C., & Wichmann, V. (2017). Recrystallization of quartz after low-temperature plasticity–The record of stress relaxation below the seismogenic zone. *Journal of Structural Geology*, *95*, 77-92.

173. Trepmann, C., & Stöckhert, B. (2001). Mechanical twinning of jadeite–an indication of synseismic loading beneath the brittle–plastic transition. *International Journal of Earth Sciences*, *90*(1), 4-13.
174. Tromans, D., & Meech, J. A. (2002). Fracture toughness and surface energies of minerals: theoretical estimates for oxides, sulphides, silicates and halides. *Minerals Engineering*, *15*(12), 1027-1041.
175. Tse, S. T., & Rice, J. R. (1986). Crustal earthquake instability in relation to the depth variation of frictional slip properties. *Journal of Geophysical Research: Solid Earth*, *91*(B9), 9452-9472.
176. Ueda, T., Obata, M., Ozawa, K., & Shimizu, I. (2020). The Ductile-to-Brittle Transition Recorded in the Balmuccia Peridotite Body, Italy: Ambient Temperature for the Onset of Seismic Rupture in Mantle Rocks. *Journal of Geophysical Research: Solid Earth*, *125*(2), e2019JB017385.
177. Voegelé, V., Cordier, P., Sautter, V., Sharp, T. G., Lardeaux, J. M., & Marques, F. O. (1998). Plastic deformation of silicate garnets: II. Deformation microstructures in natural samples. *Physics of the Earth and Planetary Interiors*, *108*(4), 319-338.
178. Wadati, K. (1928). Shallow and deep earthquakes. *Geophys. Mag.*, *1*, 162-202.
179. Wade, B. P., Kelsey, D. E., Hand, M., & Barovich, K. M. (2008). The Musgrave Province: stitching north, west and south Australia. *Precambrian Research*, *166*(1-4), 370-386.
180. Wagner, L. S., Caddick, M. J., Kumar, A., Beck, S. L., & Long, M. D. (2020). Effects of Oceanic Crustal Thickness on Intermediate Depth Seismicity. *Frontiers in Earth Science*, *8*, 244
181. Wallis, D., Hansen, L. N., Britton, T. B., & Wilkinson, A. J. (2019). High-angular resolution electron backscatter diffraction as a new tool for mapping lattice distortion in geological minerals. *Journal of Geophysical Research: Solid Earth*, *124*(7), 6337-6358.
182. Wallis, D., Hansen, L. N., Kumamoto, K. M., Thom, C. A., Plümper, O., Ohl, M., ... & Wilkinson, A. J. (2020). Dislocation interactions during low-temperature plasticity of olivine and their impact on the evolution of lithospheric strength. *Earth and Planetary Science Letters*, *543*, 116349.
183. Wallis, D., Hansen, L. N., Wilkinson, A. J., & Lebensohn, R. A. (2021). Dislocation interactions in olivine control postseismic creep of the upper mantle. *Nature communications*, *12*(1), 1-12.
184. Walsh, A. K., Raimondo, T., Kelsey, D. E., Hand, M., Pfitzner, H. L., & Clark, C. (2013). Duration of high-pressure metamorphism and cooling during the intraplate Petermann Orogeny. *Gondwana Research*, *24*(3-4), 969-983.
185. Wei, S. S., Wiens, D. A., van Keken, P. E., & Cai, C. (2017). Slab temperature controls on the Tonga double seismic zone and slab mantle dehydration. *Science advances*, *3*(1), e1601755.
186. Wex, S., Mancktelow, N. S., Camacho, A., & Pennacchioni, G. (2019). Interplay between seismic fracture and aseismic creep in the Woodroffe Thrust, central Australia–Inferences for the rheology of relatively dry continental mid-crustal levels. *Tectonophysics*, *758*, 55-72.
187. Wex, S., Mancktelow, N. S., Hawemann, F., Camacho, A., & Pennacchioni, G. (2017). Geometry of a large-scale, low-angle, midcrustal thrust (Woodroffe Thrust, central Australia). *Tectonics*, *36*(11), 2447-2476.
188. Wex, S., Mancktelow, N. S., Hawemann, F., Camacho, A., & Pennacchioni, G. (2018). Inverted distribution of ductile deformation in the relatively "dry" middle crust across the Woodroffe Thrust, central Australia. *Solid Earth*, *9*(4), 859-878.
189. White, R. W., and G. L. Clarke (1997), The role of deformation in aiding recrystallization: An example from a high-pressure shear zone, Central Australia, J. Petrol., 38(10), 1307–1329, doi:10.1093/petrology/38.10.1307
190. Wilkinson, A. J., Meaden, G., & Dingley, D. J. (2006). High-resolution elastic strain measurement from electron backscatter diffraction patterns: New levels of sensitivity. *Ultramicroscopy*, *106*(4-5), 307-313.
191. Yamasaki, T., & Seno, T. (2003). Double seismic zone and dehydration embrittlement of the subducting slab. *Journal of Geophysical Research: Solid Earth*, *108*(B4).
192. Zhan, Z. (2020). Mechanisms and implications of deep earthquakes. *Annual Review of Earth and Planetary Sciences*, *48*, 147-174.
193. Zhong, X., Petley-Ragan, A. J., Incel, S. H., Dabrowski, M., Andersen, N. H., & Jamtveit, B. (2021). Lower crustal earthquake associated with highly pressurized frictional melts. *Nature Geoscience*, *14*(7), 519-525.

ACKNOWLEDGEMENTS
The financial supports from Università degli Studi di Padova, Fondazione Ing. Aldo Gini (grant for a 6 month stay in Oslo), Excite Network (TNA access for HR-EBSD data acquisition) and PRIN_2020WPMFE9 (Project: THALES) are greatly acknowledged.
Giorgio, Luca and Alfredo are acknowledged for supervision. Manuele, Jianfeng, David, Marco and the other co-authors of the chapters are acknowledged for their contributions and help.
The people of the structural geology group in Padova (Giorgio Pennaccchioni, Giulio Di Toro, Rodrigo Gomila, Telemaco Tesei, Simone Papa, Simone Masoch, Miriana Chinello, Michele Fondriest, Manuele Faccenda) are acknowledged for great scientific discussions and equally great beers.
The people at the Njord Centre in Oslo are acknowledged for scientific discussions. In particular Sascha Zertani, Stephen Michalchuk, Hugo Lantman and Luca Menegon are thanked for the great time in Oslo.
The technical staff in Padova is acknowledged for sample preparation and help with data acquisition.

Personal acknowledgements
Too many are the people to acknowledge, that have been directly or indirectly involved in these three and a half years of PhD and contributed to my growth as a scientist. Even more are the people who influenced my life in these years of research, determining my growth as a human being. Countless the people whose meeting, either for a day, a year or the entire life, drove me to this precise moment and shaped me the way I am. All these people left something in me that is now forever recorded, crystallized in my interior, but also forever evolving and growing.
I can't mention all of them, and I apologize with who I may have forgotten.
To Giorgio and Luca, for being my mentors, for the scientific guidance, for the inspiration and for the great fun.
To Tommaso, Daniele and Marco, for all the years together, that led me to the choice of pursuing a PhD.
To Stefano, Alessandro and Alex for the grand days in the mountains.
To Simone for sharing glories and pains of these PhD years.
To EB, TP, DC, MT, AS, SC, AT, AC, SM, PR, SP, AB, MC, SZ, SM, HL, EL, AF, AC, AP, SP, HP, LN, MB, MA, PS, OC, TC, GP, LM and all the others. Forever grateful for having you in my life.